NTNU – Trondheim
Norwegian University of
Science and Technology

Oxidation of Manganese-Containing Aluminium Alloys

Oxidation of Molten Mn-Containing Al Alloys
in Various Atmospheres

Shawn Wilson

A ship in harbour is safe,
but that is not what ships are built for.

Acknowlegements

I would like to acknowledge the following people and organizations for their contributions to this work:

> My supervisor, Anne Kvithyld (SINTEF), for inviting me to do this work as part of the CastAl project and for helping me with the literature search so I didn't have to start from square one.
>
> Thorvald A. Engh, for your patience with questions I should already know the answers to, your valuable feedback, the numerous revisions and guidance you have provided throughout this Thesis.
>
> My NTNU co-supervisor, Gabriella Tranell for allowing me to choose this project even though it wasn't necessarily on the Approved List, the discussions we have had during the course of the Project, and your guidance on "what to do next".
>
> The Metallurgy department at SINTEF Materials and Chemistry for allowing me the opportunity to further my education and position in the world, as well as the time and facilities needed to complete the work herein.
>
> My SINTEF colleagues: John Walmsley, for the Auger analysis; Wilhelm Dall, for your help with the EDS work, usually on short notice; and Kai Tang, for your FactSage expertise.

And finally, I would like to thank Tanja Pettersen for your unwavering support, for feeding me occasionally, and for the final proofreading to catch all the little errors I just couldn't see.

Shawn Wilson, Trondheim,

Abstract

An oxidation study was performed on 99.99% Al, Al1%Mn and Al5%Mn materials, both in a thermogravimetric furnace, and in a muffle furnace. The mass gain behaviour for these materials was studied and compared for different temperatures and surface preparations, and was compared to previous work on Al1Mn.

Curve fitting was used with the thermogravimetric data in an attempt to develop a mathematical model to describe oxidation in the Al1%Mn materials, but a satisfactory model could not be found.

The oxidized materials were then analyzed in the Scanning Electron Microscope using EDS and Auger microprobe analysis, both for chemical composition and to analyze the structure of the oxide that was formed.

The main findings from the thermogravimetric work were are as follows:

1. Error analysis showed that the mass measurement errors were at least two orders of magnitude smaller than the mass measurements, so any differences between samples was due to different oxidation behaviour in the sample.
2. There was inconsistent oxidation behaviour for the Al1Mn surface-cleaned TGA samples; for six identical samples and experiments, five samples showed comparable results, while one sample showed much larger mass gain.
3. Sample preparation has a large influence on oxidation behaviour in the muffle furnace.
4. Mn content has an influence on oxidation behavior; there was a trend of increasing oxidation with increasing Mn content in the muffle furnace samples.

The main findings from the SEM analysis of the oxidized 99.99% Al, Al1%Mn and Al5%Mn materials are as follows:

1. The oxides formed on the Al1Mn and Al5Mn materials were thicker and different than those found on 99.99% Al
2. The oxides formed on the Al1Mn and Al5Mn materials did not contain Mn oxides
3. The oxides formed on the Al1Mn and Al5Mn materials had small particles of Mn metal completely surrounded by Al_2O_3
4. Mn-rich particles were found in the interior of the Al1Mn and Al5Mn samples
5. Small clusters of Mn metal were found among the Al_2O_3 particles on the surface of the Al1Mn and Al5Mn samples

Glow Discharge Optical Emission Spectroscopy showed that there was no measurable Mn on the surface of an as-extruded Al1Mn strip, and the Mn was deficient to a depth of some 100nm from the surface. A similar Al1Mn extruded strip that had $50\mu m$ of the surface mechanically removed also did not contain Mn on the surface, and had a similar Mn profile to the as-extruded strip.

A qualitative physical model of oxidation was suggested, based on thermogravimetric data.

Contents

List of Figures

List of Tables

Nomenclature

Abbreviations

TGA	Thermogravimetric Analysis
GD-OES	Glow Discharge Optical Emission Spectroscopy
MS	Mass Spectrometer
SEM	Scanning Electron Microscope
SE	Secondary Electron
BS	Backscatter
EDS	Energy-Dispersive X-ray Spectroscopy
Al1Mn	Aluminum + 1 weight % manganese
Al5Mn	Aluminum + 5 weight % manganese
STP	Standard Temperature and Pressure
Ø	Diameter
%RH	% Relative Humidity

Variables

P	Pressure	[atmospheres]
T	Temperature	$[K]$
t	time	$[s]$
τ	time constant	$[s]$
a	activity	*dimensionless*
γ	activity coefficient	*dimensionless*
k	equilibrium constant	dimensionless
y	mass fraction of oxygen in the oxide	*dimensionless*
$\mathscr{D}$	Diffusion coefficient	$[m^2 \ s^{-1}]$
G	Gibbs free energy	$[kJ \ mole^{-1}]$
H	enthalpy	$[kJ \ mole^{-1}]$
S	entropy	$[kJ \ mole^{-1}K^{-1}]$
h	thickness or height	$[m]$
D	diameter	$[m]$
ℓ	thickness or length	$[m]$
A	geometric surface area	$[m^2]$
m	mass	$[kg]$
n	molar quantity	$[kmol]$
$\dot{n}$	molar flux	[kmol/s]
$\dot{N}$	the molar flux per unit area	$[kmol/(m^2 s)]$
c	is the concentration of the diffusing component	$[kmol/m^3]$
ρ	density	$[kg \ m^{-3}]$
M	molecular mass	$[kg \ kmol^{-1}]$

Prefixes, superscripts and subscripts

Δ	change	
δ	error	
eq	equilibrium	
n	normal	
vap	vaporization	
ox	oxide	
met	metal	
0	original	

Constants

R	Universal gas constant	$[8.314 \ J \ mol^{-1} \ K^{-1}]$

1. Introduction

1.1 Motivation

During remelting of aluminum alloys, industrial experience has shown a tendency toward increased oxidation losses when remelting alloys containing industrially-significant levels of manganese, when compared to alloys containing magnesium.

This is surprising, given that Mn is far less reactive toward oxygen than either Al or Mg. Considerable work has been done on Al-Mg alloys, as evidenced by the volumes of information available in the literature. Far less work has been done, however, with Mn-containing alloys, and published literature concerning oxidation of these alloys is scarce.

A goal of this work is to increase what is currently known about oxidation of Mn-containing aluminum alloys and relate this knowledge to reducing oxidation losses during remelting.

1.2 Background

This Thesis builds on the author's Master's Project [17] conducted Fall 2012, concerning high temperature oxidation behavior of manganese-containing aluminum alloys. In that work, thermogravimetric measurements were conducted in gaseous atmospheres that are components of industrial remelting furnace atmospheres.

Some brief results from [17]:

1. Glow Discharge Emission Spectroscopy showed that the extruded Al-1%Mn ribbon used to make the TGA samples had an aluminum oxide layer approximately 17nm thick, with traces of Si, Zn and Na that were suspected to be contamination from previous extrusions in the extrusion press. Mn was depleted in the surface layer to a depth of 1.5μm.

2. At 800℃, there was no real difference in mass gain between dry gases, and gases containing 7 mol% H_2O.

3. At 1000℃, the humid gases caused significantly more oxidation than the dry gases, but there were multiple parallel TGA runs for the dry gases, and only one TGA run for each humid gas.

4. As expected, there was greater mass gain for all dry gases at 1000℃ than at 800℃, but there was significantly more scatter in the 1000℃ results, especially for O_2.

5. CO_2 and N_2 showed similar mass gains up to 7 hours at 1000℃, after which CO_2 showed slightly more mass gain, and O_2 showed more mass gain than both N_2 and CO_2.

6. For the 1000℃ isothermal TGA measurements, the majority of the mass gain occured in the first 60 to 90 minutes, after which the mass gain slowed significantly and became nearly linear with time. By comparison, the 800℃ isothermal TGA mass gain curves showed a much more linear mass gain with time.

7. Black aluminum oxide growths formed on the surface of Al-1%Mn samples at 1000℃ in dry CO_2 for 14 hours. These growths did not form on the dry CO_2 sample held at 1000℃ for 7 hours, nor for any of the other atmospheres.

8. At 800℃, the addition of 7 mol% H_2O had no significant effect on Al-1%Mn oxidation with O_2 and N_2 when compared to the dry gases. The addition of 7 mol% H_2O to CO_2 seemed to have a slight inhibiting effect on oxidation at 800℃, compared to dry CO_2.

9. Adding 7 mol% H_2O to O_2, N_2 and CO_2 at 1000℃ significantly increased oxidation compared to the dry gases, with humid N_2 showing approximately 2.8x more oxidation than dry N_2. Humid O_2 and CO_2 showed approximately 2.2x more oxidation than the respective dry gases.

In [17], the thermogravimetric measurements were thoroughly treated, but no analysis of the oxide layer was conducted.

1.3 Project Aim - from Project

With the basis listed above, the goal of this work is to further investigate the role of Mn in oxidation of Al-Mn alloys, with emphasis on analysis of the oxide layer using techniques such as electron microscopy.

2. Theory

Recycling aluminum consumes as little as 5% of the energy required to produce the same amount of virgin metal from alumina [7]. Dross formation during remelting increases the energy consumption in two ways: the aluminum lost to dross must be replaced by addition of primary metal, and the dross acts as an insulating barrier which reduces heat transfer into the melt.

Themodynamically, Mn should not take part in oxidation until the Al has been consumed. Rossel [1990] showed that there was slightly less metal loss for a given scrap thickness when remelting AA3103 (AlMn) than for Al 99/5 (commercially pure aluminum) at 700-900℃ in a gas-fired hearth-type furnace[13]. However, industrial remelting experience has shown the opposite; when remelting alloys containing Mn, dross formation can exceed one ton dross per 14 tons produced metal[1]. This is a significant loss when compared to the one ton dross formed per 100 tons produced metal that is normally experienced when remelting Al alloys containing Mg and Si. It is unclear what role Mn plays in the increased dross formation; the questions become:

- Do AlMn alloys oxidize more rapidly than pure Al or AlMg alloys in the remelting furnace atmosphere and conditions?
- Do AlMn alloys produce mechanically stronger oxides that trap or encapsulate more molten metal than other Al alloys? In other words, is the increased dross due to mechanical factors instead of chemical?
- Is there some other factor that leads to increased dross formation?
- Is it some combination of factors that increase dross formation?

2.1 Thermodynamics

2.1.1 Oxidation

Oxidation rates of AlMn alloys might be expected to be equal to or lower than for pure Al under the same conditions, given that Mn is much nobler than Al, based on their relative positions in the Ellingham oxidation diagram shown in Figure 2.1. Thus, Mn should not take part in oxidation until the Al is consumed. However, as mentioned in the Introduction, industrial remelting experience has shown the opposite; when remelting alloys containing Mn, dross formation can exceed one ton dross per 14 tons produced

---

[1]Information from industrial aluminum producers
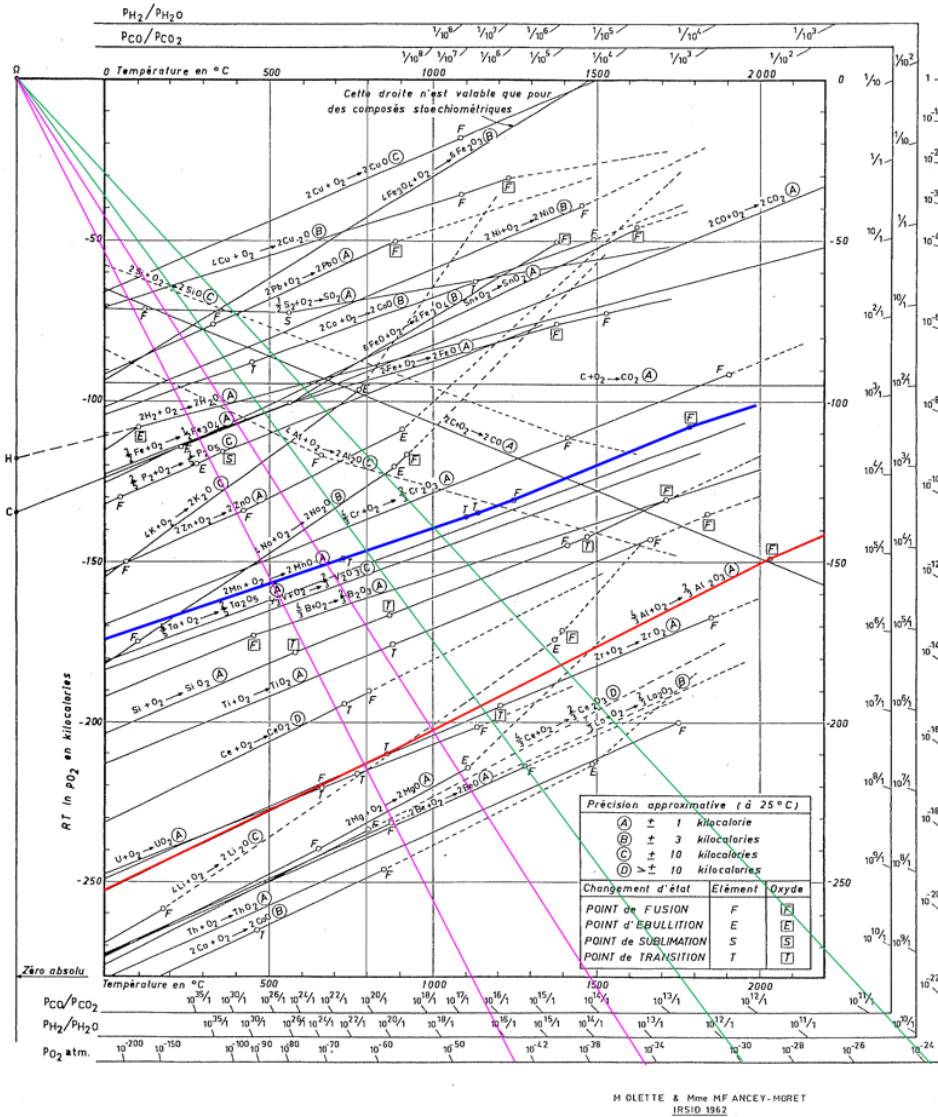
Figure 2.1: *Ellingham diagram for metal oxides, showing relative positions of Mn (blue) and Al (red). Oxygen pressures necessary for oxidation at 800 and 1000℃ are shown in green for Mn and magenta for Al.*

metal. The oxidation reactions for aluminum and manganese are as follows:

$$\tfrac{4}{3}\,\text{Al} + \text{O}_2 \longrightarrow \tfrac{2}{3}\,\text{Al}_2\text{O}_3 \quad \Delta\text{G}^{\circ}_{800\text{℃}} = -865\text{kJ/mol} \tag{2.1}$$

$$2\,\text{Mn} + \text{O}_2 \longrightarrow 2\,\text{MnO} \quad \Delta\text{G}^{\circ}_{800\text{℃}} = -610\text{kJ/mol} \tag{2.2}$$
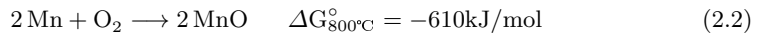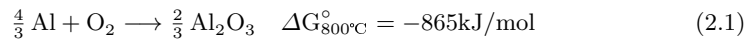
The Gibbs free energy change at 800℃, $\Delta\text{G}^{\circ}_{800\text{℃}}$, is composed of an enthalpy term and an

entropy term, where the temperature is given in Kelvin:

$$\Delta G^{\circ}_{800^{\circ}C} = \Delta H + T\Delta S \tag{2.3}$$

The Gibbs free energy change is related to the equilibrium constant k through the equation

$$\Delta G^{\circ}_{800^{\circ}C} = -RT\ln(k) \tag{2.4}$$

Table 2.1: *Gibbs free energy change and equilibrium constants for oxidation reactions (2.1) and (2.2), calculated using FactSage.*

	$\Delta G^{\circ}_{800^{\circ}C}, \frac{J}{mol}$	$k^{eq}_{800^{\circ}C}$	$\Delta G^{\circ}_{1000^{\circ}C}, \frac{J}{mol}$	$k^{eq}_{1000^{\circ}C}$
Al oxidation, (2.1)	-951956	1.43E+62	-907508	2.52E+47
Mn oxidation, (2.2)	-666563	3.32E+43	-633219	1.19E+33

where k is given by the ratio of the activities of the reactants and products. For the aluminum oxidation reaction (2.1), $k^{eq}_{Al\,ox}$ is given by

$$k^{eq}_{Al\,ox} = \frac{activity^{2/3}_{Al_2O_3}}{activity^{4/3}_{Al} \cdot activity_{O_2}} \tag{2.5}$$

similarly, for the manganese oxidation reaction (2.2), $k^{eq}_{Mn\,ox}$ is given by:

$$k^{eq}_{Mn\,ox} = \frac{activity^2_{MnO}}{activity^2_{Mn}\,activity_{O_2}} \tag{2.6}$$

The activities of pure substances such as Al, Mn and their oxides are assumed to be equal to 1, and the activity of a gas is equal to its partial pressure in atmospheres, so equations (2.5) and (2.6) reduce to

$$k^{eq}_{Al\,ox} = k^{eq}_{Mn\,ox} = \frac{1}{P_{O_2}} \tag{2.7}$$

and the equilibrium constants for these reactions is only a function of temperature and the oxygen partial pressure.

Table 2.2: *Activities and activity coefficients of Al and Mn in Al1%Mn alloy at 800℃ and 1000℃, calculated in FactSage*

	mass%	mole frac	$a_{800℃}$	$\gamma_{800℃}$	$a_{1000℃}$	$\gamma_{1000℃}$
Al	99	9.95E-01	9.95E-01	1.00E+00	9.95E-01	1.00E+00
Mn	1	4.94E-03	8.48E-06	1.72E-03	2.81E-05	5.68E-03

2.1.2 Vapour Pressure

For the pure metals, manganese has a higher vapour pressure than aluminum at remelting temperatures, but the vapour pressures are still very small relative to atmospheric pressure. These differences in vapour pressure may cause a depletion of Mn in the surface layer, to a depth of some few µm, and the depth of the depletion will be determined mainly by mass transport (diffusion) of Mn to the surface. Once at the surface, vapourization of Mn may occur at elevated temperatures. The vapour pressure for pure Al and Mn can be calculated using equation (2.8) and the constants in Table 2.3 [15]:

$$log(P/atm) = A + \frac{B}{T/K} + C \, log(T/K) \tag{2.8}$$

Table 2.3: *Vapour pressure calculation constants for pure aluminum and pure manganese [15], for use in Equation (2.8).*

Constant	A	B	C	Range, ℃	
Al. solid	9.459	-17342	-0.7927	25	660
Al. liquid	5.911	-16211		660	1527
Mn. solid	12.805	-15097	-1.7896	25	1246
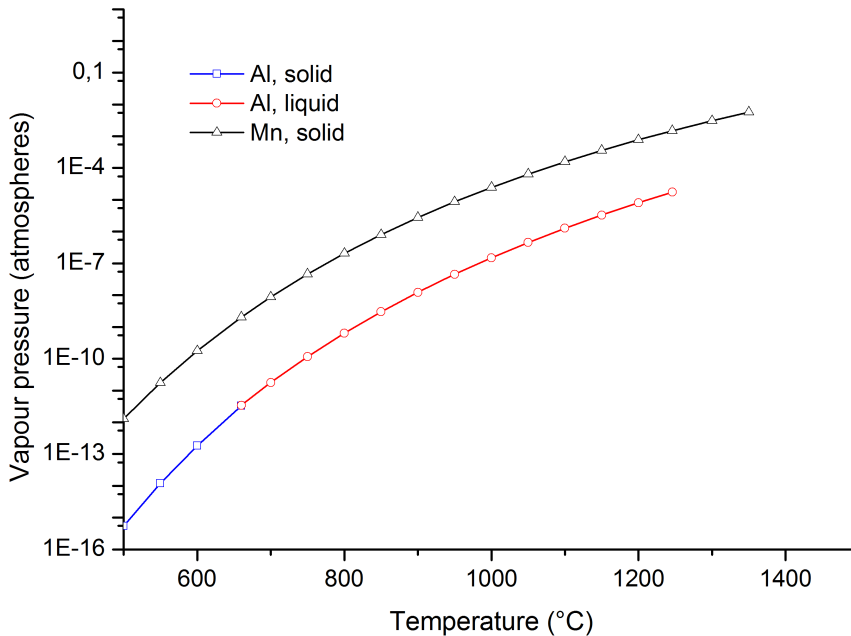
Figure 2.2: *Calculated vapour pressure curve for pure aluminum and pure manganese.*

At 800℃, the vapour pressure of Mn is approximately 300x that of Al, and at 1000℃, the vapour pressure of Mn is approximately 150x that of Al.

Table 2.4: *Calculated vapour pressures in atmospheres for aluminum and manganese*

Temperature, ℃	660	800	1000	1200	1245
$p_{Al(l)}^{vap}$, atm	3.4E-12	6.4E-10	1.5E-07	8.0E-06	1.7E-05
$p_{Mn(s)}^{vap}$, atm	2.0E-09	2.0E-07	2.5E-05	7.7E-04	2.5E-03

Using Raoult's law for low solute concentrations, the vapour pressure of a solvent in a solution is the product of the solvent molar fraction and the vapour pressure of the pure solvent. In the case of the Al alloy with 1 mass % Mn, using the mole fraction from Table 2.2 and the calculated vapour pressure from Table 2.4, the vapour pressure of Al at 800℃ is given by:

$$p_{Al} = 0.995064 \times 6.4 \times 10^{-10} = 6.32 \times 10^{-10} \, atm \tag{2.9}$$

2.1.3 Combustion

The remelting furnace is fired by hydrocarbon (natural gas, propane or oil) combustion in either air or pure oxygen. Assuming air consists of 21vol% O_2 and 79vol% N_2, the general equations for oxy-fuel and air-fuel combustion are [5]:

$$C_xH_y + (\tfrac{4x+y}{4})O_{2(g)} \longrightarrow x\,CO_2 + (\tfrac{y}{2})H_2O_{(g)} + heat \tag{2.10}$$

$$C_xH_y + (\tfrac{4x+y}{4})\{O_{2(g)} + 3.76\,N_2\} \longrightarrow$$
$$\longrightarrow x\,CO_2 + (\tfrac{y}{2})H_2O_{(g)} + 3.76(\tfrac{4x+y}{4})N_2 + heat \tag{2.11}$$
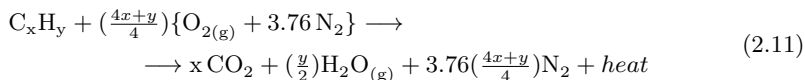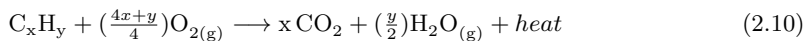
Nitrogen is carried through reaction (2.11) as an inert species, but small amounts may oxidize to form ppm levels of undesireable NO_x, depending largely on the flame temperature [11]. Furnaces are typically operated with 2-4% more oxygen than is required by stoichiometry to ensure complete combustion. However, carbon monoxide may be formed at ppm levels due to incomplete combustion if there is insufficient air (oxygen) available, or if there is incomplete combustion for some other reason, such as malfunctioning burners.

The benefits of oxy-fuel over air-fuel heating are twofold: higher flame temperatures are possible, and less nitrogen is present in the furnace. Further, it is simpler and less costly to implement CO_2 capture programs on the exhaust streams from oxy-fuel furnaces because the gas volumes are smaller and have a higher concentration of CO_2 compared to air-fuel furnaces.

A drawback of the higher flame temperatures of oxy-fuel heating is the increased tendency for any nitrogen present in the furnace atmosphere to react to form NO_x above 1300℃ [11], so good furnace sealing and operation of the furnace at a slight overpressure are important to exclude N_2-containing air from the process.

Water vapour is a product of both combustion processes, and is found in the furnace atmosphere at levels approaching 10% by volume for air-fuel furnaces, and up to 50% by volume for oxy-fuel furnaces[2]. Previous work on AlMg alloys has shown that water

---

[2]Measurements taken by SINTEF as part of the CastAl project

vapour contributes to rapid Al oxidation [9] via the reaction

$$H_2O_{(g)} + \tfrac{2}{3} Al_{(l)} \longrightarrow \tfrac{1}{3} Al_2O_3 + H_{2(g)} \quad \Delta G^{\circ}_{800^{\circ}C} = 296kJ/mol \tag{2.12}$$
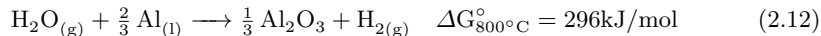
The hydrogen that is liberated, when measured with a mass spectrometer, is a strong indicator of rapid or so-called "breakaway" oxidation and coincides with periods of rapid mass gain measurements.

2.2 Oxide Thickness Calculation

The average thickness of the oxide that forms on a sample during an oxidation experiment can be calculated if the mass gain and surface area are known; this Section is adapted from Wagner [16].

The mass fraction of oxygen in the oxide is given by

$$y = \frac{M_O}{M_{ox}} \tag{2.13}$$

The thickness of the oxide film multiplied by the density of the oxide equals the mass of the oxide film per unit area

$$\Delta \ell_{ox} \rho_{ox} = \frac{m_{ox}}{A} \tag{2.14}$$

It is assumed that all of the mass change is due to the reaction of oxygen with the metal to form oxide; no metal is lost. Then the total mass gain per unit area is equal to the product of the oxide thickness, the oxide density and the mass fraction of oxygen in the oxide

$$\frac{\Delta m}{A} = y \rho_{ox} \Delta \ell_{ox} \tag{2.15}$$

where $y\rho_{ox}$ is the mass of oxygen per volume of oxide. Rearranging Equation (2.15) gives an expression for the theoretical oxide thickness in terms of the mass gain

$$\Delta \ell_{ox} = \frac{1}{y} \frac{1}{\rho_{ox}} \frac{\Delta m}{A} \tag{2.16}$$

The loss of metal per unit area equals

$$\frac{\Delta m_{met}}{A} = (1 - y) \frac{m_{ox}}{A} = \frac{1 - y}{y} \frac{\Delta m}{A} = (1 - y) \rho_{ox} \Delta \ell_{ox} \tag{2.17}$$

Moreover, the loss of metal per unit area can be written as the product of the metal density and the displacement of the boundary of the oxide-metal interface

$$\rho_{met} \Delta \ell_{met} = \frac{\Delta m_{met}}{A} \tag{2.18}$$

The oxide has a different density than the metal, and the oxide thickness given in Equation (2.16) does not reflect this density change. Substituting Equation (2.17) into Equation (2.18) gives the actual oxide-metal boundary displacement in terms of either the total mass change or the oxide thickness

$$\Delta\ell_{met} = \frac{1}{\rho_{met}}\frac{(1-y)}{y}\frac{\Delta m}{A} = (1-y)\frac{\rho_{ox}}{\rho_{met}}\Delta\ell_{ox} \tag{2.19}$$

2.3 The Parabolic Rate Law

Wagner [16] contains a thorough description of the parabolic rate law, from which this Section was adapted.

When a coherent oxide film is formed, diffusion of the reactants, metal or oxygen across the oxide layer is a necessary step. According to Fick's first law, the number of moles diffusing per unit area per unit time equals

$$\frac{\dot{n}}{A} = \dot{N} = \mathscr{D}_c\left|\frac{\partial c}{\partial x}\right| \tag{2.20}$$

where

In general, $\mathscr{D}_c$ depends on concentration. Upon integration of Equation (2.20) between the metal-oxide interface and the outer surface involving the concentrations c' and c", respectively,

$$\frac{\dot{n}}{A}\int_0^{\Delta x}\mathrm{d}x = \dot{N}\int_0^{\Delta x}\mathrm{d}x = \left|\int_{c'}^{c''}\mathscr{D}_c\,\mathrm{d}c\right| \tag{2.21}$$

which gives

$$\frac{\dot{n}}{A} = \dot{N} = \frac{1}{x}\left|\int_{c'}^{c''}\mathscr{D}_c\,\mathrm{d}c\right| \tag{2.22}$$

Consequently, if the concentrations or activities of the reactants in the adjacent phases are kept constant and thermodynamic equilibrium at the boundaries of the oxide film is practically established, the reaction rate is inversely proportional to the instantaneous thickness of the oxide film. According to Tammann (1920), we may take the increase of the film thickness per unit time as a measure of the reaction rate. Thus

$$\frac{\mathrm{d}(\Delta\ell_{ox})}{\mathrm{d}t} = \frac{k'}{\Delta x} \tag{2.23}$$

where k' is a constant with the dimension $\left[\frac{length^2}{time}\right]$. Upon integration,

$$(\Delta\ell_{ox})^2 = 2\,k't \tag{2.24}$$

or

$$\Delta\ell_{ox} = \sqrt{2\,k't} \tag{2.25}$$

Thus a plot of $\Delta\ell_{ox}$ versus time t, gives a parabola (parabolic or quadratic rate law). Using the mass increase per unit area $\frac{\Delta m}{A}$ as a measure for the advancement of the reaction and recalling that $\frac{\Delta m}{A}$ is proportional to $\Delta\ell_{ox}$ according to Equation (2.15), another form of the parabolic rate law[3] is obtained:

$$\left(\frac{\Delta m}{A}\right)^2 = k'' t \tag{2.26}$$

where the rate constant k'' has the units $\left[\dfrac{mass^2}{length^4\, time}\right]$ \hfill (2.27)

2.4 Mixed control kinetics

Young [18] describes a kinetics regime that is a combination of diffusion and phase boundary processes. In the early stages, the oxidation rate may be controlled by a phase boundary reaction, but as the oxide thickens, diffusion through the oxide gradually becomes the controlling factor. Linear-parabolic kinetics is described by the rate equation

$$x^2 + C_1 x = kt + C_2 \tag{2.28}$$

where x is mass gain (or increase in oxide thickness). To get mass gain as a function of time,

$$x^2 + C_1 x - (kt + C_2) = 0 \tag{2.29}$$

$$x^2 + C_1 x + \frac{C_1^2}{4} - \left(\frac{C_1^2}{4} + kt + C_2\right) = 0 \tag{2.30}$$

$$\left(x + \frac{C_1}{2}\right)^2 - \left(\sqrt{\frac{C_1^2}{4} + kt + C_2}\right)^2 = 0 \tag{2.31}$$

the equation above is of the form

$$(x + a)^2 - b^2 = 0 \tag{2.32}$$

where

$$[(x + a) + b][(x + a) - b] = 0 \tag{2.33}$$

$$\left\{\left(x + \frac{C_1}{2}\right) + \sqrt{\frac{C_1^2}{4} + kt + C_2}\right\}\left\{\left(x + \frac{C_1}{2}\right) - \sqrt{\frac{C_1^2}{4} + kt + C_2}\right\} = 0 \tag{2.34}$$

and the solution to the quadratic equation is

$$x = -\frac{C_1}{2} \pm \sqrt{\frac{C_1^2}{4} + kt + C_2} \tag{2.35}$$

For $t \geq 0$, $x \geq 0$, so take the positive root:

$$x = -\frac{C_1}{2} + \sqrt{\frac{C_1^2}{4} + kt + C_2} \tag{2.36}$$

_____

[3] Pilling and Bedworth, Journ. Inst. Metals *29*, 529 (1923)

2.5 Diffusion model

Diffusion of oxygen through the alumina layer can be described by the model where the surface of the material has an existing oxide layer, ℓ_0, which increases by thickness $\Delta\ell_{ox}$ upon heating in an oxidizing atmosphere, as shown in Figure 2.3.
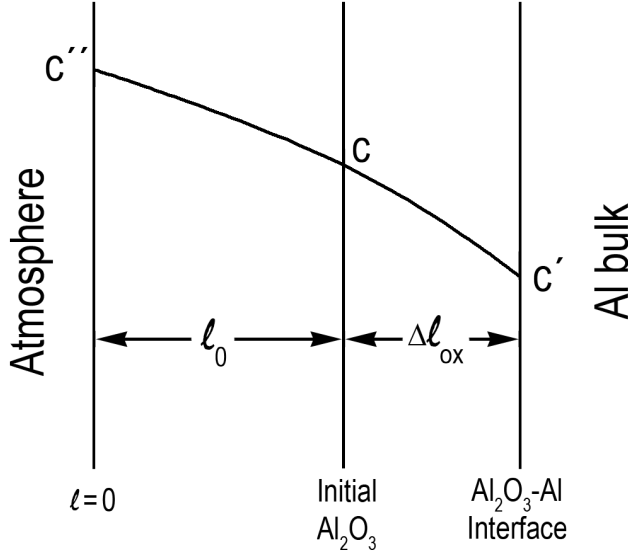
Figure 2.3: *Diffusion model*

Assuming that the diffusivity of oxygen is the same in the original oxide as in the newly-formed oxide, the oxidation can be described by an equation of the form $\frac{\ell}{2\sqrt{\mathscr{D}(t+\tau)}}$.

$$\frac{c'' - c}{c'' - c'} = \frac{2}{\sqrt{\pi}} B \int_0^{\frac{\ell}{2\sqrt{\mathscr{D}(t+\tau)}}} e^{-v^2} \, \mathrm{d}v \qquad (2.37)$$

the diffusivity of oxygen through the oxide $\mathscr{D}$ and the thickness of the inital oxide ℓ_0 are known, and the constants B and τ are to be determined. At $t = 0$, $\ell = \ell_0$ and $c = c'$. Then Equation (2.37) becomes

$$1 = \frac{2}{\sqrt{\pi}} B \int_0^{\frac{\ell_0}{2\sqrt{\mathscr{D}\tau}}} e^{-v^2} \, \mathrm{d}v \qquad (2.38)$$

As the oxidation proceeds, $\ell = \ell_0 + \Delta\ell_{ox}$ and $c = c'$

$$1 = \frac{2}{\sqrt{\pi}} B \int_0^{\frac{\ell_0+\Delta\ell_{ox}}{2\sqrt{\mathscr{D}(t+\tau)}}} e^{-v^2} \, \mathrm{d}v \qquad (2.39)$$

11

As a simplification, $\frac{\ell_0 + \Delta\ell_{ox}}{2\sqrt{\mathscr{D}(t+\tau)}} = \alpha$, then Equation (2.38) becomes

$$1 = \frac{2}{\sqrt{\pi}}B\int_0^\alpha e^{-v^2}\mathrm{d}v \tag{2.40}$$

where α is a constant. At the Al–Al_2O_3 interface,

$$\ell = \ell_0 + \Delta\ell_{ox} = 2\alpha\sqrt{\mathscr{D}(t+\tau)} \tag{2.41}$$

and at $t = 0$, $\Delta\ell_{ox} = 0$, so

$$\ell_0 = 2\alpha\sqrt{\mathscr{D}\tau} \tag{2.42}$$

therefore, α is given by ℓ_0, $\mathscr{D}$ and τ. τ (is unknown and) is found from the mass balance: From the mass balance for the oxide, there are three oxygen atoms per molecule of Al_2O_3, and τ can be determined:

$$3\frac{\mathrm{d}(\Delta\ell_{ox})}{\mathrm{d}t}\frac{\rho_{ox}}{M_{ox}} = -\mathscr{D}\frac{\mathrm{d}c}{\mathrm{d}\ell} \tag{2.43}$$

from Equation (2.37)

$$\frac{\mathrm{d}c}{\mathrm{d}\ell} = -(c''-c')\frac{2}{\sqrt{\pi}}\frac{B}{2\sqrt{\mathscr{D}(t+\tau)}}e^{-\alpha^2} \tag{2.44}$$

$$3\frac{\mathrm{d}(\Delta\ell_{ox})}{\mathrm{d}t}\frac{\rho_{ox}}{M_{ox}} = (c''-c')\frac{2}{\sqrt{\pi}}\frac{B\mathscr{D}}{2\sqrt{\mathscr{D}(t+\tau)}}e^{-\alpha^2} \tag{2.45}$$

$$3\frac{\mathrm{d}\ell}{\mathrm{d}t}\frac{\rho_{ox}}{M_{ox}} = (c''-c')\frac{2}{\sqrt{\pi}}\frac{B\mathscr{D}}{2\sqrt{\mathscr{D}(t+\tau)}}e^{-\alpha^2} \tag{2.46}$$

Multiply Equation (2.46) by ℓ and substitute Equation (2.41) on the RHS:

$$\frac{3}{2}\frac{\mathrm{d}\ell^2}{\mathrm{d}t}\frac{\rho_{ox}}{M_{ox}} = (c''-c')\frac{2}{\sqrt{\pi}}B\mathscr{D}\alpha e^{-\alpha^2} \tag{2.47}$$

From Equation (2.41), $\ell^2 = 4\alpha^2\mathscr{D}(t+\tau)$:

$$\frac{3}{2}4\mathscr{D}\frac{\mathrm{d}[\alpha^2(t+\tau)]}{\mathrm{d}t}\frac{\rho_{ox}}{M_{ox}} = (c''-c')\frac{2}{\sqrt{\pi}}B\mathscr{D}\alpha e^{-\alpha^2} \tag{2.48}$$

$$6\left[\frac{\mathrm{d}\alpha^2}{\mathrm{d}t}(t+\tau) + \alpha^2\right]\frac{\rho_{ox}}{M_{ox}} = (c''-c')\frac{2}{\sqrt{\pi}}B\alpha e^{-\alpha^2} \tag{2.49}$$

A solution to Equation (2.49) is that α does not depend on t. (Solve graphically using TGA data) Then:

$$6\frac{\rho_{ox}}{M_{ox}}\alpha = (c''-c')\frac{2}{\sqrt{\pi}}B\alpha e^{-\alpha^2} \tag{2.50}$$

Solving Equation (2.50) to give α as a function of B gives

$$e^{-\alpha^2} = \frac{3\sqrt{\pi}}{B(c'' - c')} \frac{\rho_{ox}}{M_{ox}}$$

(2.51)

B is obtained from Equation (2.40):

$$\frac{1}{B} = \frac{2}{\sqrt{\pi}} \int_0^\alpha e^{-v^2} \mathrm{d}v = \mathrm{erf}(\alpha)$$

(2.52)

The Gauss error function $\mathrm{erf}(\alpha)$ for $-1 \leq \alpha \leq 1$ can be approximated by the Taylor series

$$\frac{2}{\sqrt{\pi}} \sum_{n=0}^{\infty} \frac{(-1^n)\alpha^{2n+1}}{n!(2n+1)} = \frac{2}{\sqrt{\pi}} \left(\alpha - \frac{\alpha^3}{3} + \frac{\alpha^5}{10} - \frac{\alpha^7}{42} + \frac{\alpha^9}{216} - \dots \right)$$

(2.53)

then

$$B = \left[\frac{2}{\sqrt{\pi}} \left(\alpha - \frac{\alpha^3}{3} + \frac{\alpha^5}{10} - \frac{\alpha^7}{42} + \frac{\alpha^9}{216} - \dots \right) \right]^{-1}$$

(2.54)

Equation (2.42) is used to solve for τ.

If the thermogravimetric oxidation data is converted into $\Delta\ell_{ox}$ as a function of time t, we can determine the diffusivity $\mathscr{D}$ from Equation (2.41).

2.6 Error Analysis

There are two types of error encountered in experimental measurements: *systematic error*, which always occurs with the same value when we use the instrument, and *random error*, which may vary from observation to observation and is equally likely to be positive or negative [14].

An example of a systematic error is the repeatable, reliable change in a thermogravimetric signal due to change of furnace gas properties (volume, viscosity, enthalpy, . . .) with temperature, independent of any changes in the sample. Random error often occurs when instruments are pushed to their limits, i.e. digital balances can have random error in the least significant digit. The measurement uncertainties for the equipment used in this work are given in Table 2.5.

Experimental work does not generally produce the desired measurement directly, i.e. the result is calculated from measured primary quantities. The error in the desired measurement is calculated from the uncertainty in these primary quantities according to the formulae shown in Table 2.6.

Table 2.5: *Limits of accuracy for measuring instruments used in this work*

Instrument	Range	Repeatability
Setsys TGA Type S thermocouple	0-1700°C	$\pm 0.0025(T, \text{°C})^{\dagger}$
Setsys TGA microbalance, large range	$\pm 200 mg$	$\pm 0.4 \mu g^{\ddagger}$
Setsys TGA microbalance, small range	$\pm 20 mg$	$\pm 0.04 \mu g^{\ddagger}$
Sartorius M36S microbalance	$31 g$	$\leq \pm 2 \mu g^{\ddagger}$
Sartorius BP301S microbalance	$303 g$	$\leq \pm 0.2 mg^{\ddagger}$

† N.I.S.T. Monograph 175, Revised to ITS-90

‡ Manufacturer documentation

Table 2.6: *Error calculation formulae for different mathematical operations, from Squires [14]*

Relation between Z, A and B	Relation between standard errors	
$Z = A + B$ $Z = A - B$	$\delta Z^2 = \delta A^2 + \delta B^2$	(2.55)
$Z = AB$ $Z = A/B$	$\left(\dfrac{\delta Z}{Z}\right)^2 = \left(\dfrac{\delta A}{A}\right)^2 + \left(\dfrac{\delta B}{B}\right)^2$	(2.56)
$Z = A^n$	$\dfrac{\delta Z}{Z} = n\dfrac{\delta A}{A}$	(2.57)
$Z = \ln A$	$\delta Z = \dfrac{\delta A}{A}$	(2.58)
$Z = \exp(A)$	$\dfrac{\delta Z}{Z} = \delta A$	(2.59)

2.7 Sample preparation considerations

Previous Al-Mn thermogravimetric oxidation work by the author [17] was conducted using discs punched from an extruded strip of Al1Mn, with no further processing of the sample surface. Glow discharge optical emission spectroscopy (GD-OES) analysis showed that the surface of the as-extruded strip had an oxide layer nearly $20 \mu m$ thick. Impey [7] reported work by Thiele, Ginsberg and Datta, and Sharova that indicated small amounts of Na contamination (0.0013-0.24%) caused increased oxidation in pure Al.

GD-OES analysis of the extruded Al1Mn strip in Wilson [17] showed that the oxide layer contained traces of Si, Zn and Na that were not present in the original alloy, and the surface of the strip was depleted in Mn to a depth of $1.5 \mu m$. In light of the Mn depletion, it is possible that the surface of the extruded samples approximated that of pure Al when heated in the TGA, so in order to get accurate oxidation results for Al1Mn, the surface layer of the extruded strip must be removed to expose the Mn-containing bulk. This can be done by, for example, sputtering, machining, mechanical polishing or electropolishing, but all of these processes can affect the oxidation results.

Impey [7] reviewed work prior to 1989 which found that sample preparation played an important role in the oxidation of solid aluminum. Unpolished Al surfaces were reported to gain less mass than mechanically polished surfaces, and samples which were manually polished using abrasives gained more mass during oxidation than those with chemically polished surfaces because of greater surface roughness and therefore surface area generated when using abrasives. Further, machined samples were reported to have a surface area of 8-10 times the geometric area, while unspecified "special polishing procedures" could result in a surface area as high as 25 times the geometric area.

Therefore, sample preparation deserves careful consideration, and will likely play a very important role in the results of the current work

3. Experimental

3.1 Materials

99.99% pure Al was used as a reference material, since the oxidation properties of very pure Al have been well-studied. Al1Mn represents the upper range of Mn content in commercial Al alloys, and Al5Mn was chosen as an "extreme" content to investigate if (or how) Mn affects Al oxidation or dross formation; there are no industrially-relevant alloys with 5% Mn.

The Al1Mn alloy and Al5Mn alloys used in this work were prepared by the casting laboratory at SINTEF. The Al1Mn alloy was prepared from 99.8% Al and a commercial master alloy containing Al and 20 weight% Mn, while the Al5Mn alloy was prepared from 99.99% Al and the same 20wt% Mn master alloy. In both cases the alloys were cast into ingots that were allowed to cool in air.

A portion of the Al1Mn ingot was machined into a Ø95x200mm cylinder that was subsequently extruded into a 1.6x78.5mm strip in SINTEF's extrusion press. This extrusion was used for the thermogravimetric (TGA) oxidation work shown in Sections 4.2 and 4.3, and was also used in the TGA work in [17].

Material from the remaining Al1Mn and Al5Mn ingots, as well as from some 99.99% pure Al were used for the muffle furnace oxidation experiments. The muffle furnace sample preparation is discussed in Section 3.2.4, and the muffle furnace results are presented in Section 4.5

Figures 3.1 and 3.2 show the binary phase diagram for the Al-Mn system calculated using FactSage, in the area of interest to this work, and indicate the various phases expected at different temperatures.
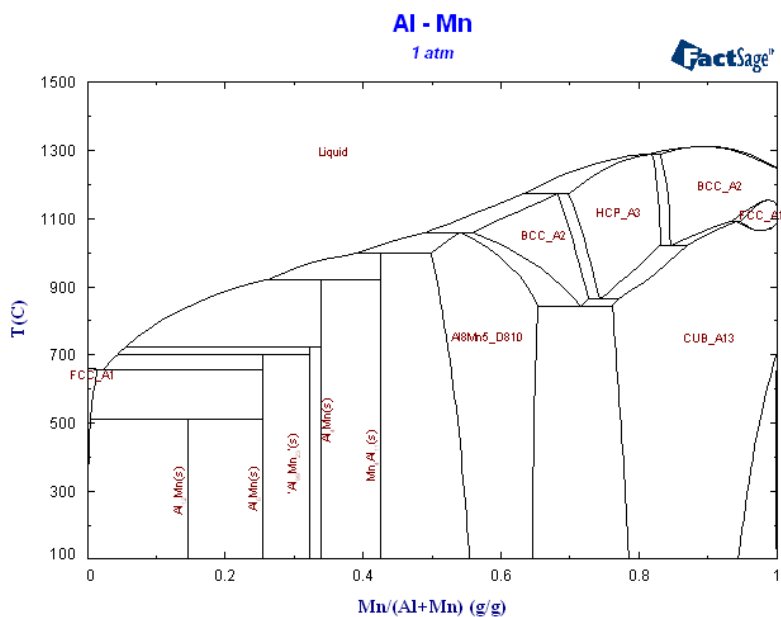
Figure 3.1: *Aluminum-manganese phase diagram calculated using FactSage [8]*
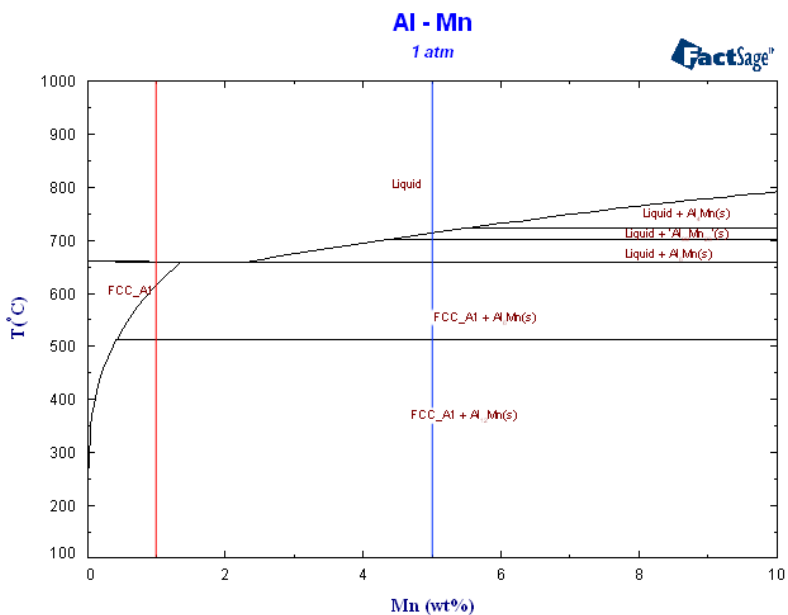
Figure 3.2: *Aluminum-manganese phase diagram showing the composition region from 0-10wt% Mn, calculated using FactSage [8]. Alloys with 1% Mn (red line) and 5% Mn (blue line) were used in this work.*

3.2 Thermogravimetric Oxidation

3.2.1 Setaram SetSys 2400 Thermogravimetric Analyzer

Thermogravimetric Analysis (TGA) is measurement of mass change under controlled heating in a controlled atmosphere. The outlet gases can be analyzed using mass spectroscopy to give more information about any reactions that take place.

TGA measurements were carried out using a Setaram SetSys 2400 TG-DTA, an equipment schematic is shown in Figure 3.3.
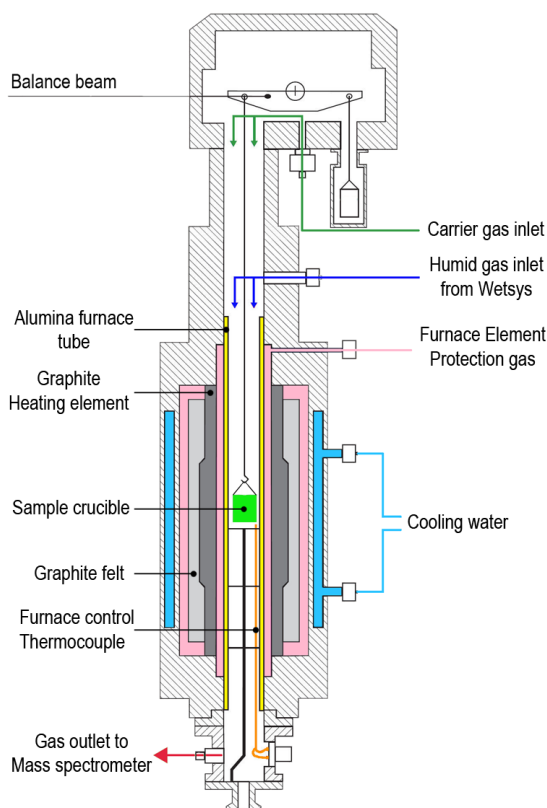
Figure 3.3: *Schematic of Setaram Setsys 2400 TGA*

The Setsys is equipped with two mass flow controllers for furnace atmosphere control, and gas flows can be changed and/or mixed at different ratios during an experiment. Typical gas flow during experiments is 20 normal mL/min; that is to say all programmed gas flows are corrected to Standard Temperature and Pressure (STP) conditions: 1 atmosphere pressure, 0℃ and 22.414L/mol. Gas flow rates above $50ml_n$/min cause noise in the TG measurements which increases with temperature, due to turbulent flow past the sample

crucible. The Setsys balance has $\pm 0.4\mu g$ resolution, and $\varnothing 0.5mm$ platinum wires connect the $\varnothing 10x10mm$ sintered alumina sample crucible to the balance beam.

Typical heating rates are up to 30℃/min, and complex heating and cooling profiles can be programmed.

3.2.2 Setaram Wetsys Gas Humidifier

A Setaram Wetsys humidified the gas for experiments requiring water vapour, and was connected to the Setsys via a heated gas transfer tube and 3-way bypass valve. The gas flow rate through the Wetsys is adjustable up to $50ml_n/min$, and the outlet gas temperature is adjustable from room temperature up to 80℃. While the humidity can be programmed to follow a given profile during the experiment, the gas flow rate is fixed for the duration of the experiment at a user-determined value up to $50ml_n/min$.

It is important to ensure that the humid gas is kept above its dew point to prevent condensation in the gas transfer tube or Setsys furnace. The Wetsys control interface uses % relative humidity (%RH) to set how much water vapour to add to the dry gas, so it is simple to use a psychrometric chart to ensure that the process is operated above the dew point for the chosen amount of humidity. However, most chemical reaction and kinetics calculations are in terms of molar quantities; it is not straight forward to convert from relative humidity to molar or mass fractions. See Appendix C for detailed humid gas calculations.

Water vapour can damage the Setsys balance head, so for experiments using humid gas, a minimum of $5ml_n/min$ dry experimental gas is used to purge the balance head, while the humid gas enters the furnace below the balance head; see Figure 3.3. This dilutes the humid gas that reaches the sample, so the humid gas water content and flow rate must be adjusted accordingly.

3.2.3 Pfeiffer Quadrupole Mass Spectrometer

A Pfeiffer QMA422 Quadrupole Mass Spectrometer (MS) was connected to the Setsys by a (1m long) heated capillary, and measured the composition of the SetSys furnace gases directly below the sample crucible. When water vapour is present, hydrogen peaks provide evidence of accelerated (breakaway) oxidation according to Equation (2.12). In experiments with H_2O vapour, the MS data also shows when the "operating" humidity level is reached.

The MS can be operated in two modes: scanning a spectrum of molecular masses, or scanning only defined masses. Scanning a spectrum of masses will show all of the species present in the sample gas, but this generates a large amount of data that is difficult to interpret. Scanning only defined masses generates time-series data that is easy to interpret, but if other species are present in the sample gas, they will be ignored. The number of possible components in this system was limited and known, so it was more efficient to scan only defined masses.

The MS data does not give absolute concentrations directly. Rather, it shows relative ion concentrations in terms of $\frac{mass}{charge}$: $\frac{M}{Q}$ or $\frac{M}{Z}$, and has SI units of $\frac{kg}{Coulomb}$. In order to give

quantitative concentrations the MS must be calibrated for each species being measured, but in this work the MS has not been calibrated.

3.2.4 Aluminum sample preparation

The TGA samples were prepared from the 1.6x78.5mm Al1Mn extruded strip described in Section 3.1. The surface of the as-extruded strip was cleaned mechanically by removing at least $50\mu m$ using a carpenter's hand plane, as detailed in Sections 4.2 and 4.3. Ø8.5mm discs were then punched from the strip using a hand punch with a flat face, and these discs were used in the TGA experiments.

3.2.5 TGA procedure

In this work the samples were heated according to the profile shown in Figure 3.4, with a 7 hour isothermal period at 1000℃.
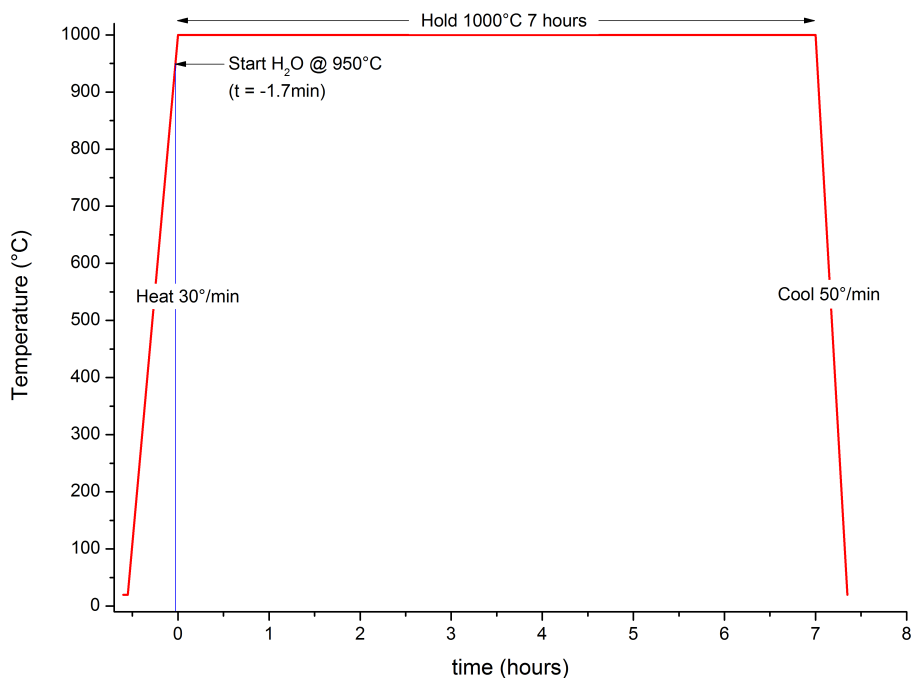
Figure 3.4: *Heating profile with 7 hour isotherm used for TGA sample analysis.*

The Setsys program included a vacuum-purge cycle before heating the sample, to ensure that only the pure, dry experimental gas was in the furnace during the heating phase. The sample lay flat in the bottom of the crucible so that the sample shape was maintained when it melted. The upper side of the sample was openly exposed to the furnace atmosphere, while the lower surface was not. The operating procedure for dry gas was:

1. Weigh sample and crucible on external balance
2. Load sample and crucible in Setsys
3. Start Setsys and MS programs simultaneously
4. When experiment is finished, weigh sample and crucible on external balance

In experiments using H_2O vapour, the humid gas was started at 950℃ in order to restrict the effects of water vapour to the isothermal period. During the start-up and heating phase, the Wetsys was running but the humid gas bypassed the furnace through a 3-way valve for three reasons:

1. The aim of the experiments was to expose the sample to humid atmosphere only during the isothermal period, to simplify analysis of the results.
2. If the Wetsys is not isolated from the Setsys during the vacuum-purge cycle before heating, humid gas is pulled through the Wetsys and the Setsys cannot achieve full vacuum.
3. It takes some minutes for the Wetsys humidity output to stabilize after a large program setpoint change. If the Wetsys is operating at the correct humidity setpoint in the bypass mode, there is only a very small disturbance in the Wetsys output that stabilizes within 15-20 seconds when the 3-way valve is switched from bypass to the Setsys.

The Setsys program was adjusted so that the total gas flow rate was the same before and after the 3-way valve was switched.

Operating procedure for humid gas:

1. Weigh sample and crucible on external balance
2. Load sample and crucible in Setsys
3. Set humid gas 3-way valve to bypass
4. Start Setsys, Wetsys and MS programs simultaneously
5. At time = 3 minutes before the start of the isotherm (950℃, 52 minutes after program start), switch humid gas 3-way valve from bypass to Setsys
6. When experiment is finished, weigh sample and crucible on external balance

3.3   Muffle Furnace Oxidation

The TGA results from the Master Project [17] preliminary to this work indicated that the majority of the sample mass change occurs in the first 60-90 minutes of isothermal heating. However, the thin disc-shaped TGA samples have a high surface area:volume ratio, and do not accurately reflect the conditions of the molten bath in the remelting furnace. For a rapid comparison of oxidation characteristics between pure Al and the Al1Mn and Al5Mn alloys, and to better simulate the conditions of a molten bath under a normal air atmosphere, three groups of oxidation trials were conducted in a muffle furnace in the sequence shown in Table 3.1:

Table 3.1: *Muffle furnace oxidation experimental matrix.*
Material A = 99.99% Al, B = Al1Mn, C = Al5Mn.

Group	Material	Preparation	Temp, ℃	Sample mass, g
1	A+B	Abrasive belt	1000	40.41 ± 0.06
2	A+B+C	Machined	1200	35.55 ± 0.05
3	A	Machined	1000	38.67 ± 0.04

The results of the muffle furnace experiments are presented in Section 4.5.

3.3.1 Alumina crucible preparation

Ø30x40mm (size A2) crucibles made of 99.7% Al_2O_3 were used to contain the aluminum samples. The empty crucibles were "pre-baked" for 2h in the muffle furnace at 1000℃ (1200℃ for the 1200℃ experiments) to prevent a change in crucible mass during Al heating from affecting the results.

3.3.2 Aluminum sample preparation

Samples were cut from ingots of the respective alloys using a bandsaw. For the samples in Group 1 (Table 3.1), pieces were cut from blocks of the respective alloys using a bandsaw, and an abrasive belt sander with a 60-grit belt was used to shape the samples to fit the crucible and to bring the sample masses close to each other; no further surface treatment was done.

For the samples in Groups 2 and 3 (Table 3.1), blocks were cut from the respective ingots in a bandsaw, then machined into cylinders and cut to length in a lathe. The bandsawing was done using a water-based synthetic coolant/lubricant, but the machining work was done without coolant or lubricant so as not to contaminate the samples. The fine adjustment of sample masses was done by drilling holes to remove material in a drill press, also without coolant or lubricant.

The finished samples were loaded into the "pre-baked" Ø30x40mm crucibles, which were then loaded into a muffle furnace that was preheated to 1000℃ (1200℃).

3.3.3 Muffle furnace procedure

The purpose of the muffle furnace tests was to measure the mass gain while the sample was molten. To determine the time needed to melt the sample, the furnace was preheated to 1000℃, then a single crucible and 40g sample was placed in the centre of the furnace. The sample appeared completely molten after 8 minutes, and this was taken as the t_0 for the subsequent samples.

The radiant and convective heat emitted from an open furnace at 1000℃ makes it challenging to place all of the crucibles for each group inside the furnace quickly and accurately if done one at a time. Further, there is considerable heat lost from the furnace that takes

time to recover. Therefore, for each experiment group, all of the crucibles were arranged on a 15mm thick plate of refractory material, then the plate was loaded into the furnace.

At the times designated in Figures 3.5 through 3.7 (corresponding to Groups 1 through 3 in Table 3.1), one crucible of each alloy was removed from the furnace and allowed to cool naturally in air. When the samples had cooled to room temperature, the mass changes were recorded.
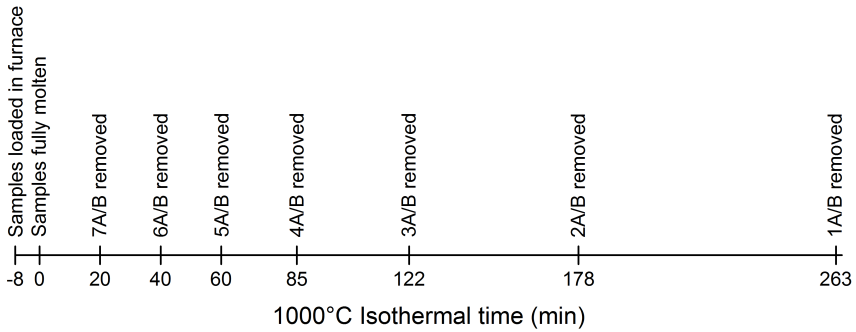
Figure 3.5: *Muffle furnace oxidation timeline for Group 1 samples (Table 3.1); pairs of samples were removed from the furnace at the times indicated. "A" = 99.99% Al, "B" = Al1Mn.*
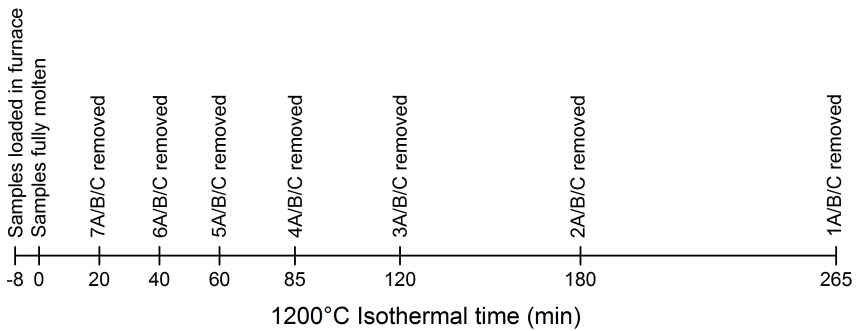
Figure 3.6: *Muffle furnace oxidation timeline for Group 2 samples (Table 3.1); sample triples were removed from the furnace at the times indicated. "A" = 99.99% Al, "B" = Al1Mn, "C" = Al5Mn.*
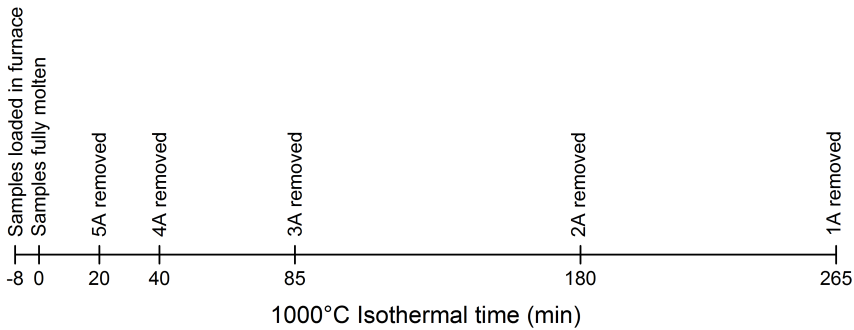
Figure 3.7: *Timeline for Group 3 (Table 3.1) 99.99% Al muffle furnace oxidation experiments; samples were removed from the furnace at the times indicated. MuffleTime1002*

3.4   Sample Analysis

3.4.1   Scanning Electron Microscope

Sections from the samples produced by the muffle furnace oxidation in Section 3.3 were examined using a Hitachi SU6600 Field Emission Scanning Electron Microscope (SEM) equipped with a Bruker Quantax Energy Dispersive x-Ray Spectrometer (EDS).

The surface composition of two TGA samples from Wilson [17] were analyzed using a JEOL 9500F Auger Microprobe.

3.4.2   SEM Sample preparation

To get meaningful results in the SEM, the samples must be polished to a fine finish, and the surface must be electrically conductive. If the sample - or at least the surface of the sample - is not conductive there will be a buildup of electrons known as "charging", which shows up as featureless bright spots in the images.

The oxide-metal interface to be inspected was less than $10\mu m$ thick; to prevent rounding of the edges during polishing and damage to the relatively fragile oxide layer, the samples were mounted in epoxy. However, both the epoxy and the oxide are electrically insulating, so coating the samples with a thin layer of carbon using a physical vapour deposition process provided the required conductivity without affecting the sample.

The procedure used for sample preparation:

1. Remove solidified samples from alumina crucibles - some of the samples were stuck in the crucibles and the crucibles had to be broken
2. Cut a section from the top portion of each sample using an abrasive cutoff disc, with one plane parallel to the axis of the material; see Figure 3.8
3. Mount the removed section in epoxy and polish to a $1\mu m$ finish using standard metallographic techniques

4. Carbon coat the finished samples
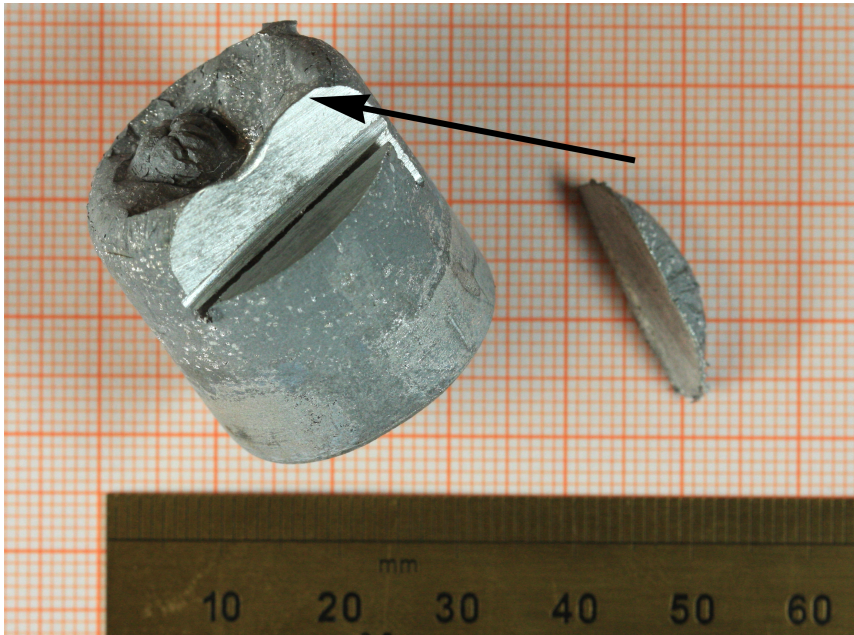
Figure 3.8: *Section cut from muffle furnace sample after heating, section to be mounted and polished is shown on the right. The arrow indicates the oxide-metal interface that was examined in the SEM*

3.4.3 GD-OES

Glow Discharge Optical Emission Spectroscopy (GD-OES) was used to analyze the composition of the Al1Mn extruded strip, using a Horiba Jobin Yvon *GD Profiler*. These measurements were performed by Hydro Aluminium's Surface Laboratory at Karmøy, Norway.

4. Results

4.1 Surface analysis of unheated Al1Mn extrusion

In Wilson [17], Glow Discharge Optical Emission Spectroscopy (GD-OES) analysis showed that there was no Mn on the surface of the as-extruded Al1Mn strip, and the Mn concentration did not reach the bulk concentration until a depth of some $150 - 200 nm$.

To investigate this further, two areas of the same extruded strip used in [17] were "cleaned" mechanically. At least $50 \mu m$ of material was removed from the surface of the as-extruded strip using a carpenter's hand plane, and it was expected that the surface of the cleaned samples would have the same composition as the bulk. These two cleaned areas and two adjacent untreated areas were analyzed using GD-OES. Figures 4.1, 4.3 and 4.5 show the GD-OES results for one as-extruded and surface cleaned pair (Pair A in the figures), and Figures 4.2, 4.4 and 4.6 show the other pair (Pair B in the figures).

Oxygen constitutes 47 mass% in Al_2O_3, and Figures 4.1 and 4.2 show that the oxide layer (vertical black line at the intersection of the Al and Mn spectra at 47 mass%) is thinner in the samples where the extruded surface was removed.

Figures 4.3 and 4.4 show that the Mn profiles of the cleaned and as-extruded samples are very nearly identical, and there is practically no measurable Mn on the surface. Si content in the top $100 nm$ of the cleaned samples is lower than that of the as-extruded samples.

Figures 4.5 and 4.6 show that the surface $0 - 40 nm$ in the cleaned samples is lower in Si, Mg and Zn contents than in the as-extruded samples, but the Mn profiles appear similar.
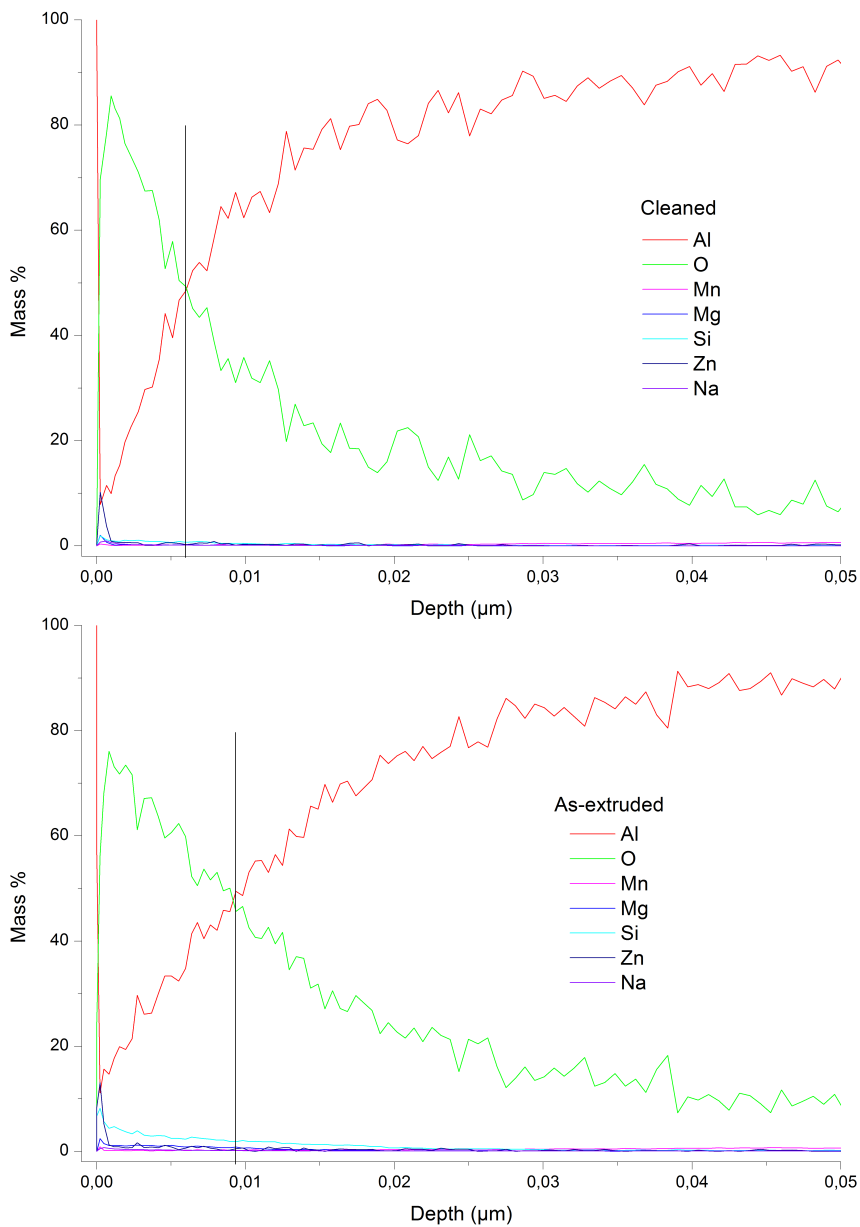
Figure 4.1: *GD-OES analysis of the oxide thickness for Al1Mn sample pair A, with surface removed by planing (top) and as-extruded (bottom). The vertical line indicates the thickness of the Al$_2$O$_3$ layer.*
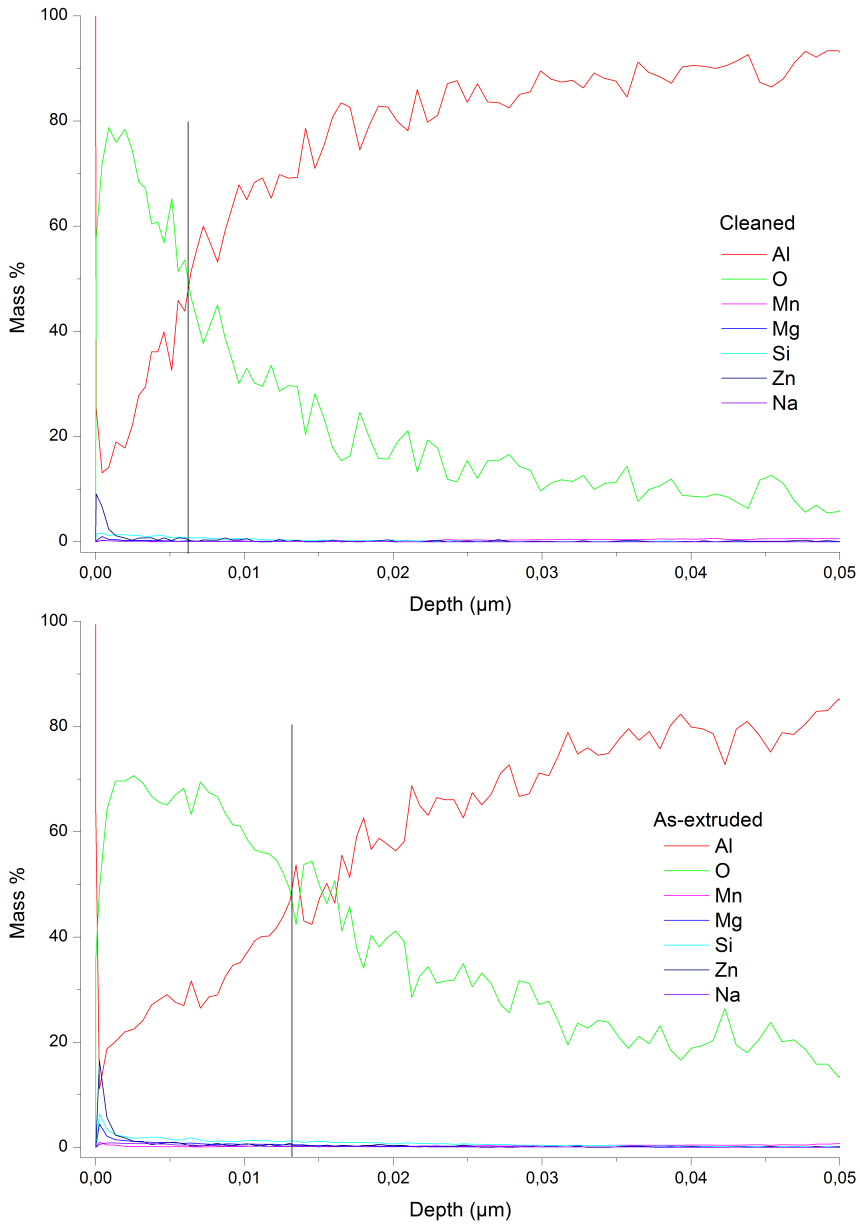
Figure 4.2: *GD-OES analysis of the oxide thickness for Al1Mn sample pair B, with surface removed by planing (top) and as-extruded (bottom). The vertical line indicates the thickness of the Al_2O_3 layer.*
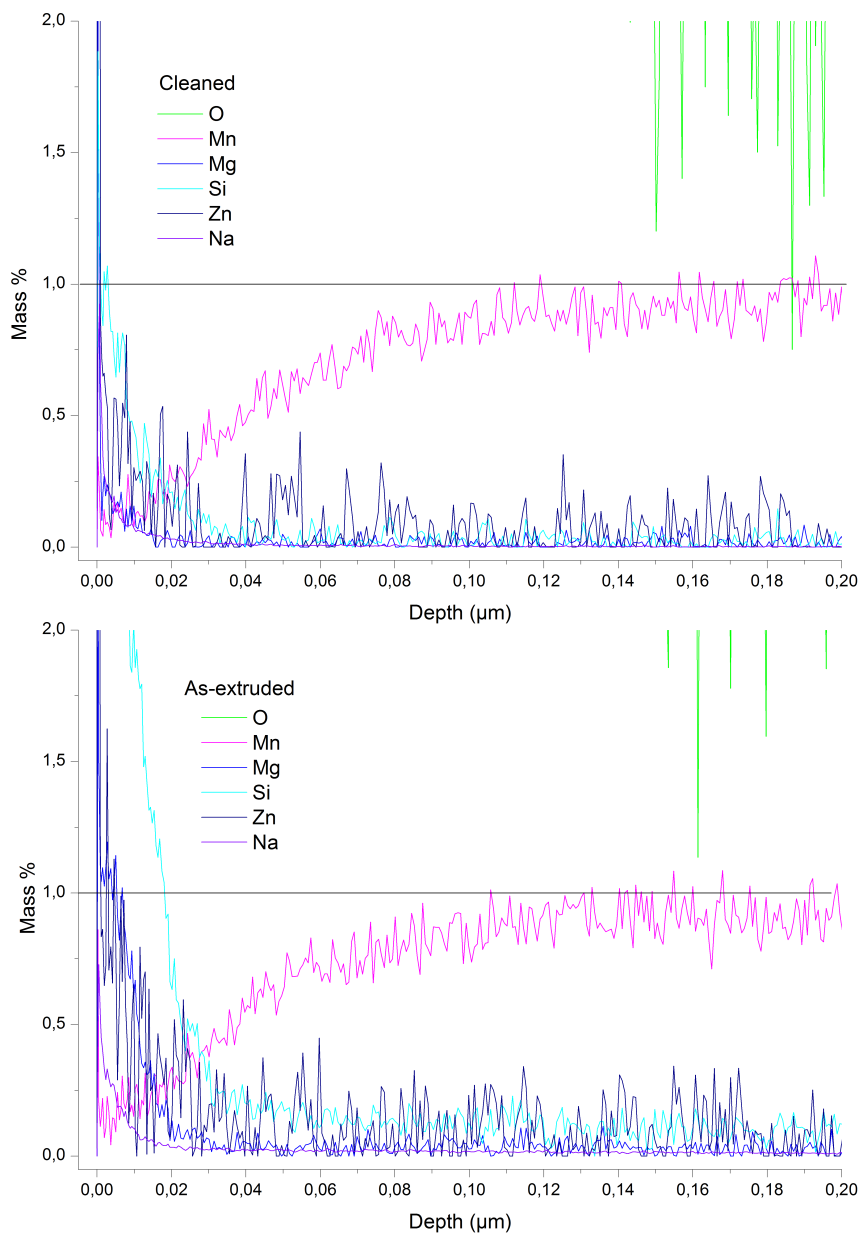
Figure 4.3: *GD-OES analysis for extruded Al1Mn sample pair A, showing the Mn and Si profiles for sample with planed surface (top) and as-extruded (bottom). The horizontal line represents the 1% Mn bulk concentration. Axes rescaled from Figure 4.1.*
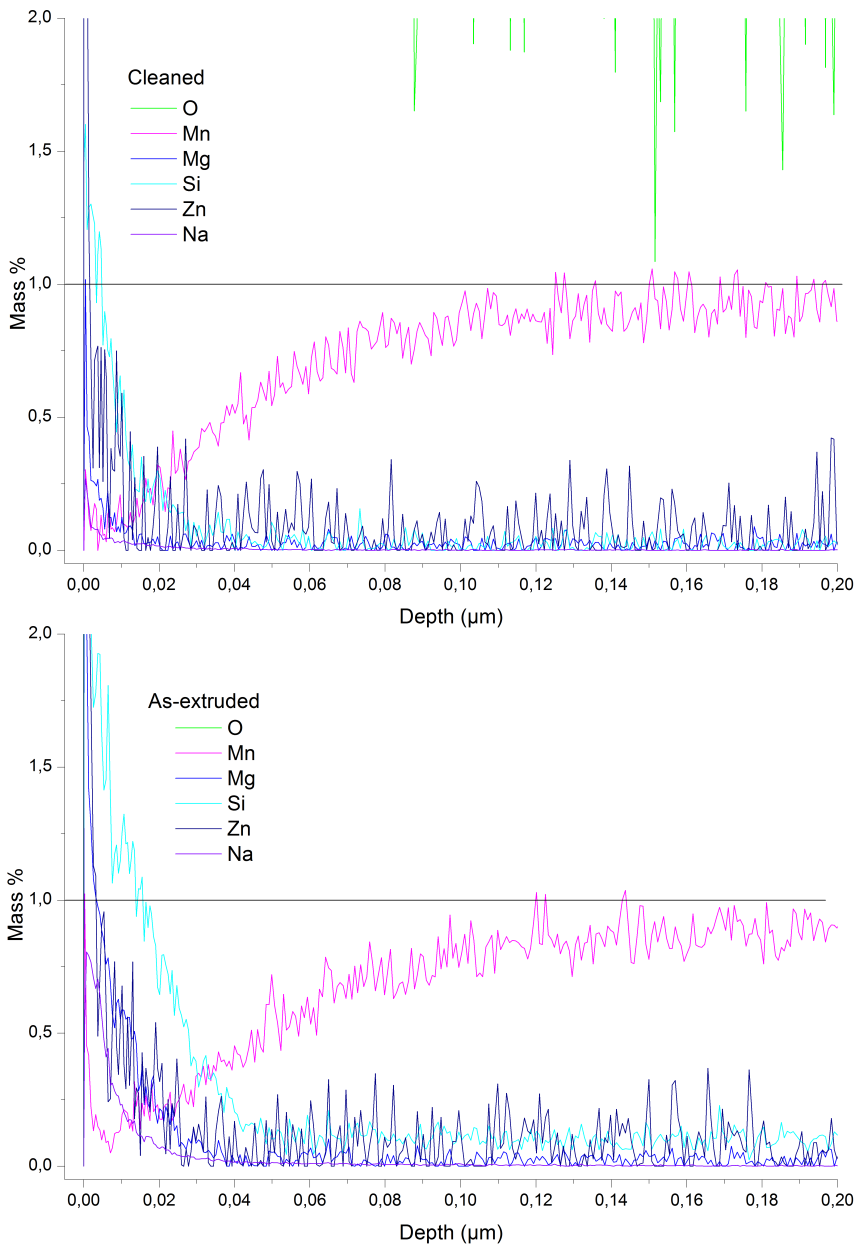
Figure 4.4: *GD-OES analysis for extruded Al1Mn sample pair B, showing the Mn and Si profiles for sample with planed surface (top) and as-extruded (bottom). The horizontal line represents the 1% Mn bulk concentration. Axes rescaled from Figure 4.2.*
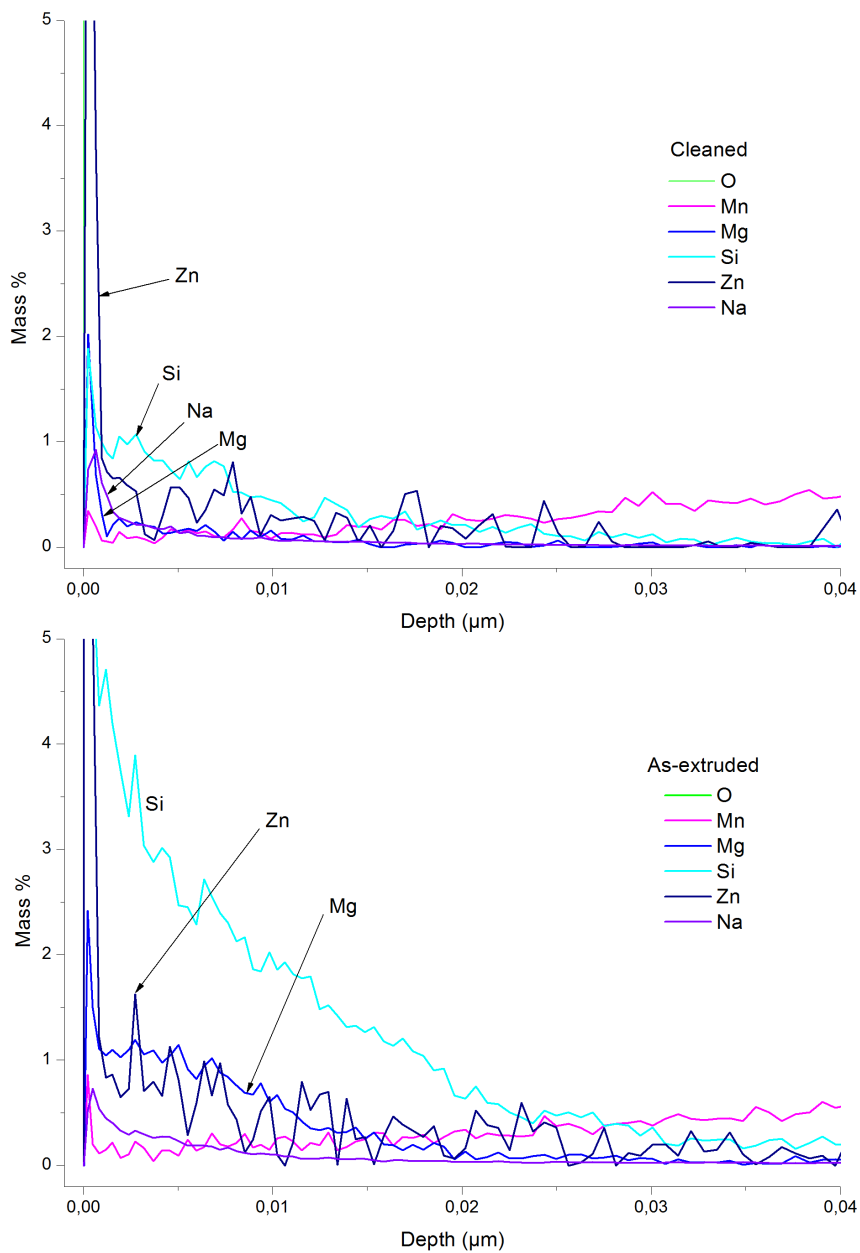
Figure 4.5: *GD-OES analysis for extruded Al1Mn sample pair A showing the Si, Mg and Zn profiles for sample with planed surface (top) and as-extruded (bottom). Axes rescaled from Figure 4.1.*
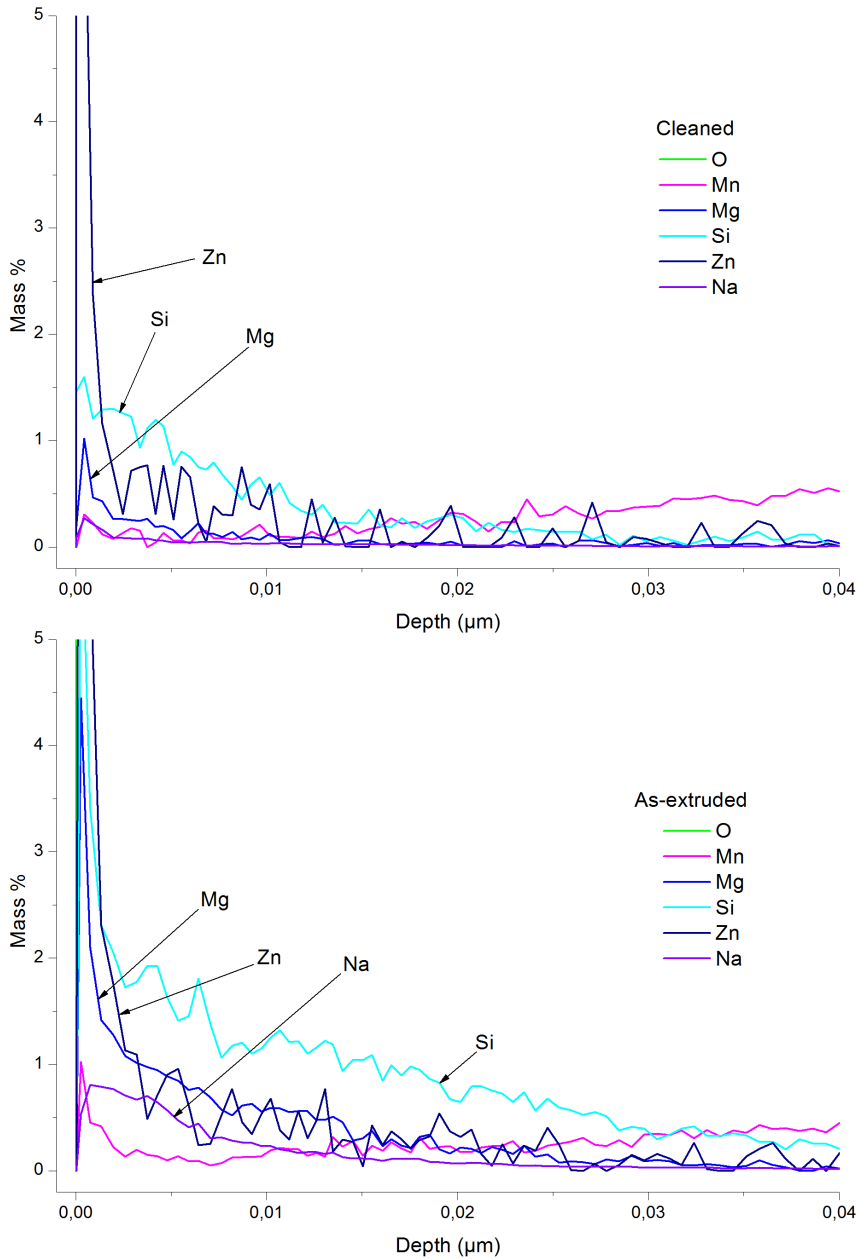
Figure 4.6: *GD-OES analysis for extruded Al1Mn sample pair B showing the Si, Mg and Zn profiles for sample with planed surface (top) and as-extruded (bottom). Axes rescaled from Figure 4.2.*

4.2   Preliminary TGA Oxidation Trials

In Wilson [17], GD-OES analysis revealed that the surface of the extruded strip was depleted in Mn to a depth of approximately $150nm$.

Different methods of surface removal such as chemical etching, machining and abrasive grinding were considered, to obtain a surface composition that was the same as that of the bulk. As mentioned in Section 4.1, a carpenter's plane was used to remove at least $50\mu m$ of material from the surface of the extruded Al1Mn strip to expose the bulk. Samples were then punched from the extruded strip and run in the TGA, using the same heating program and conditions as for Sample O2-800 in [17]. The TGA mass gain results of the cleaned samples (130224 and 130225) are compared to those for the as-extruded sample from Wilson [17] in Figure 4.7.
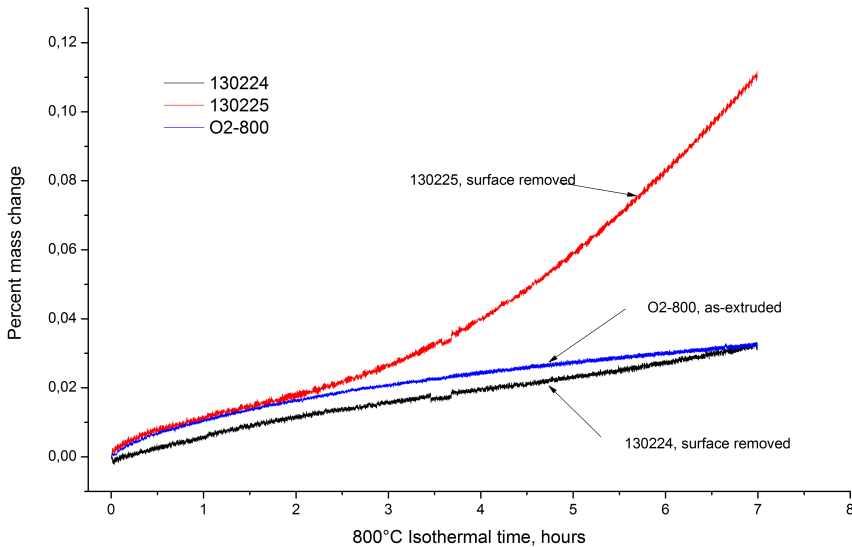
Figure 4.7: *800℃ 7h isothermal TGA results for cleaned Al1Mn strip in O_2. The mass gain curve from sample "O2-800" is from [17], Samples 130224 and 130225 were run using the same TGA program as Sample O2-800.*

Figure 4.7 shows that the oxidation behaviour of the cleaned samples is not consistent. Sample 130224 has nearly the same behaviour as Sample O2-800, while Sample 130225 has significantly more mass gain than Sample O2-800, and the rate of mass gain for Sample 120225 is increasing with time.

4.3 TGA with cleaned Al1Mn in $N_2 + 7\,\%H_2O$ at 1000℃

A series of six samples from the mechanically cleaned Al1Mn extruded strip were heated in the thermogravimetric furnace in $N_2 + 7\,\%H_2O$ for 7 hours at 1000℃. Figures 4.8 through 4.15 show the mass change and mass spectrometer results for these samples.

Figures 4.8 and 4.10 through 4.13 show similar mass change results; there is a rapid mass gain in approximately the first 15 minutes, but then the mass gain is essentially finished in the first 30 minutes. From 30 minutes to the end of the experiment there is a slow, nearly linear mass gain.

Sample 130327 in Figure 4.14 gained much more mass than the other samples, even though the samples were treated identically, and there is a significant peak in the H_2 signal in the first few minutes of the experiment that indicates breakaway oxidation, as discussed in Section 2.1.3.

The mass changes for all six experiments are compared in Figures 4.14 and 4.15; the mass of Sample 130327 increased at approximately the same rate as the other samples, but the mass gain did not flatten off at 15 minutes as with the other samples.

The H_2O and H_2 mass spectrometer signals from Figures 4.8 through 4.13 are compared in Figures 4.16 and 4.17, respectively. The H_2O signals do not show any significant differences, which indicates that the furnace atmosphere was identical between all of the samples. The H_2 signals, on the other hand, show more variation. The significant peak for Sample 130327 has already been discussed; the H_2 signals for the other samples also have peaks that correlate with relatively rapid rates of oxidation, but these peaks are much smaller than for Sample 130327.
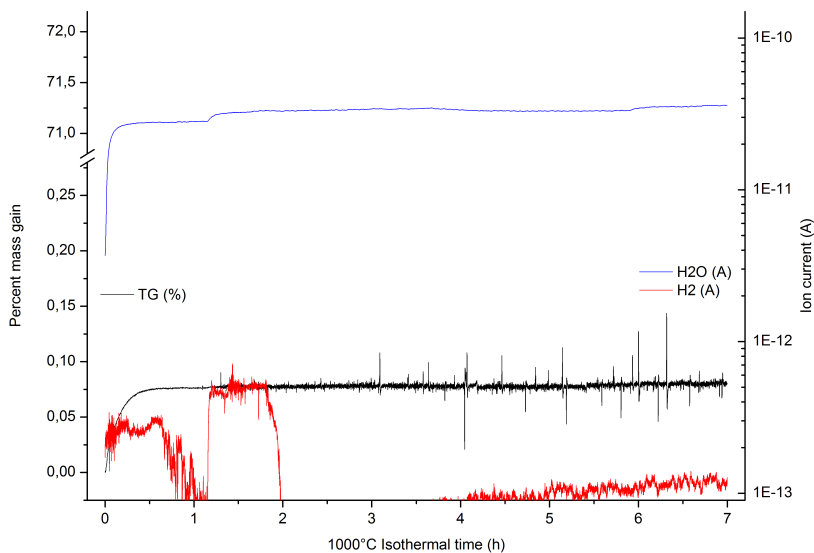
Figure 4.8: *TGA results for 1000℃ isothermal heating of Al1Mn sample 130326 in $N_2 + 7\%H_2O$.*
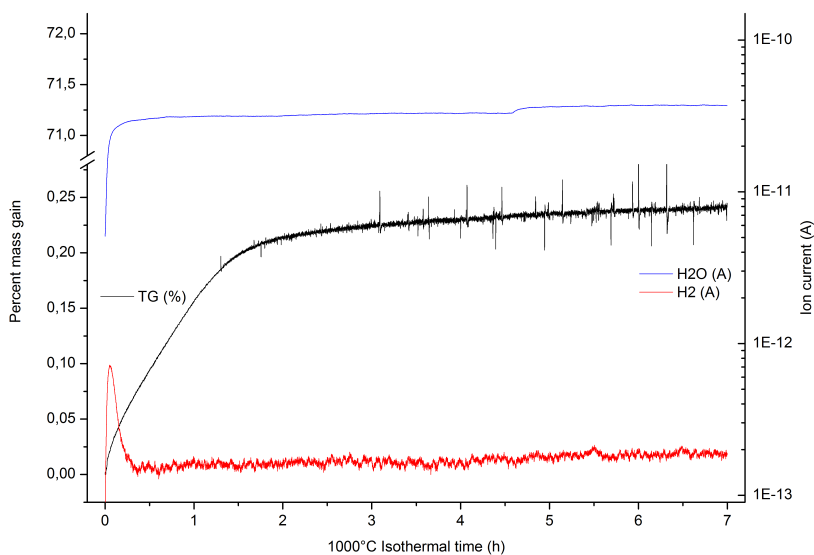
Figure 4.9: *TGA results for 1000℃ isothermal heating of Al1Mn sample 130327 in $N_2 + 7\%H_2O$*

36
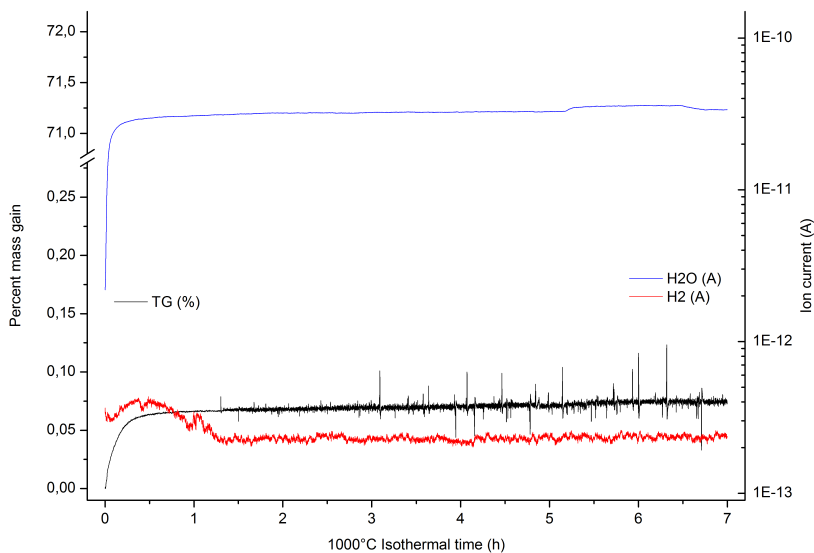
Figure 4.10: *TGA results for 1000℃ isothermal heating of Al1Mn sample 130328 in* $N_2 + 7\%H_2O$
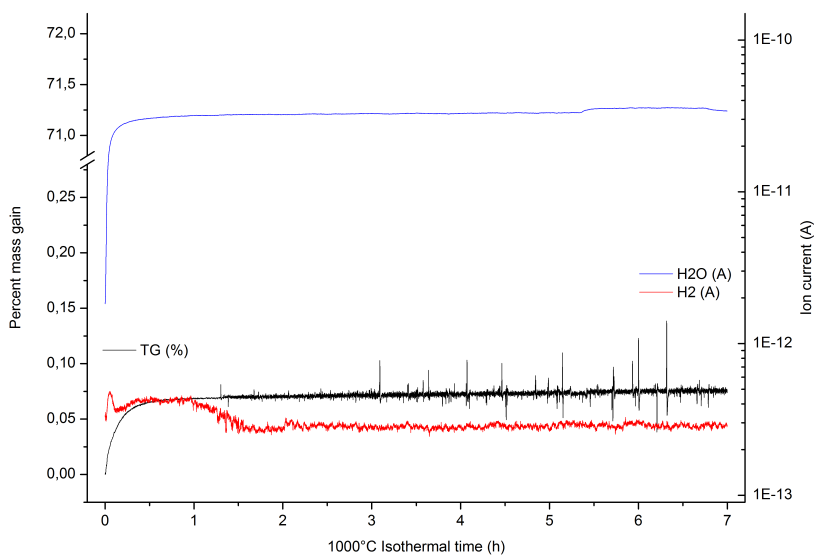
Figure 4.11: *TGA results for 1000℃ isothermal heating of Al1Mn sample 130329 in* $N_2 + 7\%H_2O$
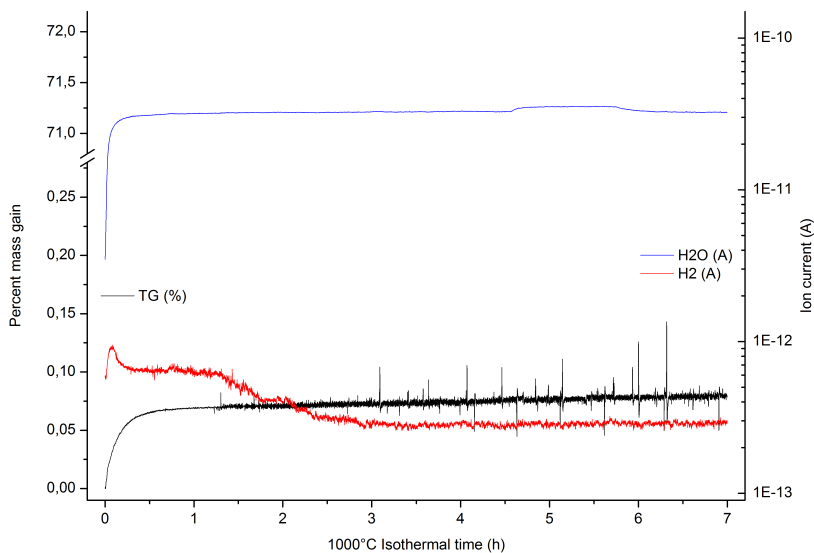
Figure 4.12: *TGA results for 1000℃ isothermal heating of Al1Mn sample 130330 in $N_2 + 7\%H_2O$*
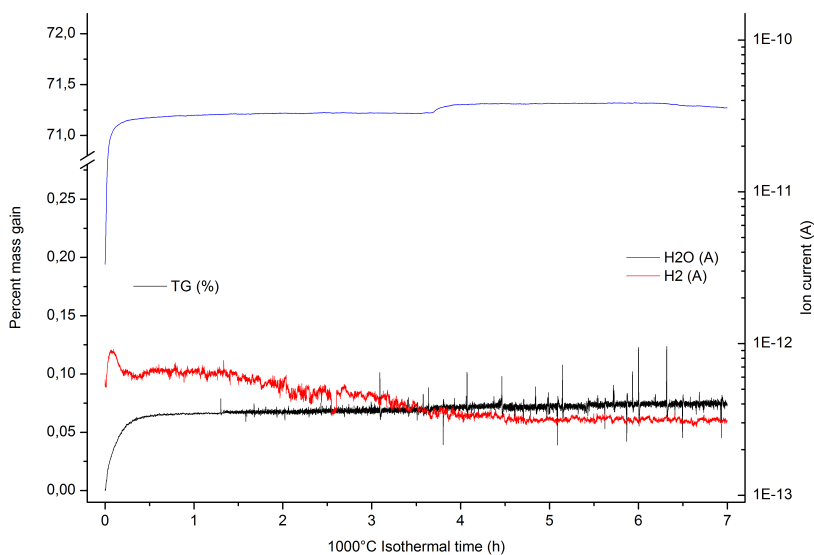
Figure 4.13: *TGA results for 1000℃ isothermal heating of Al1Mn sample 130331 in $N_2 + 7\%H_2O$*
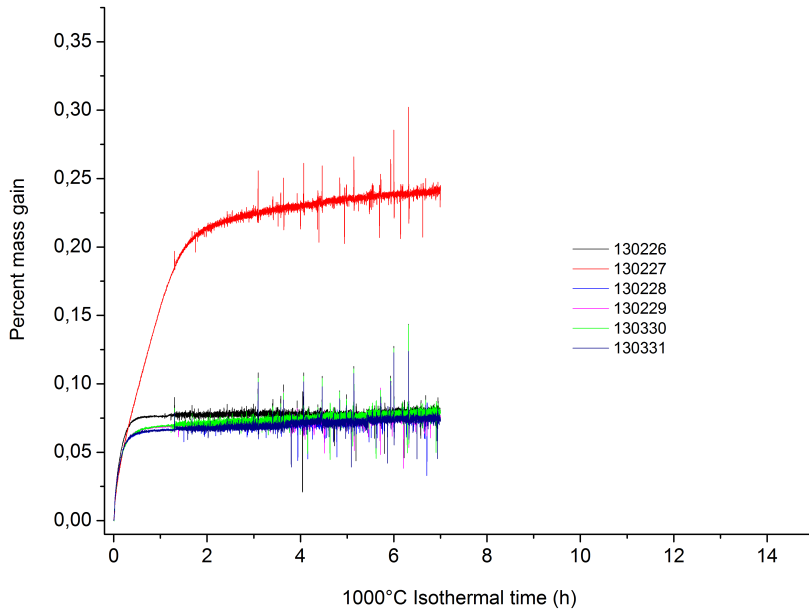
Figure 4.14: *Comparison of TGA mass change results for Al1Mn samples 130326 through 130331, from Figures 4.8 through 4.8 TG1H2O*
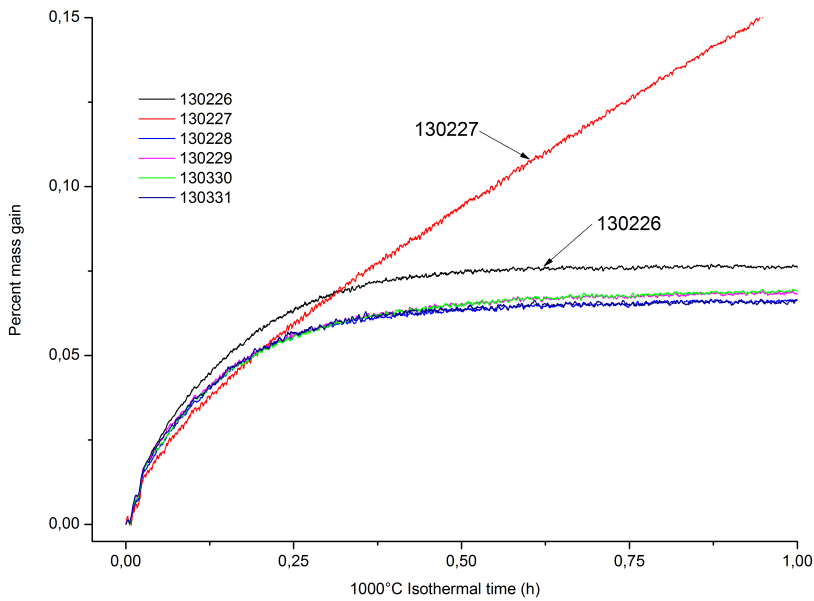
Figure 4.15: *Comparison of TGA mass change results for Al1Mn samples 130326 through 130331, rescaled axes from Figure 4.14*

39
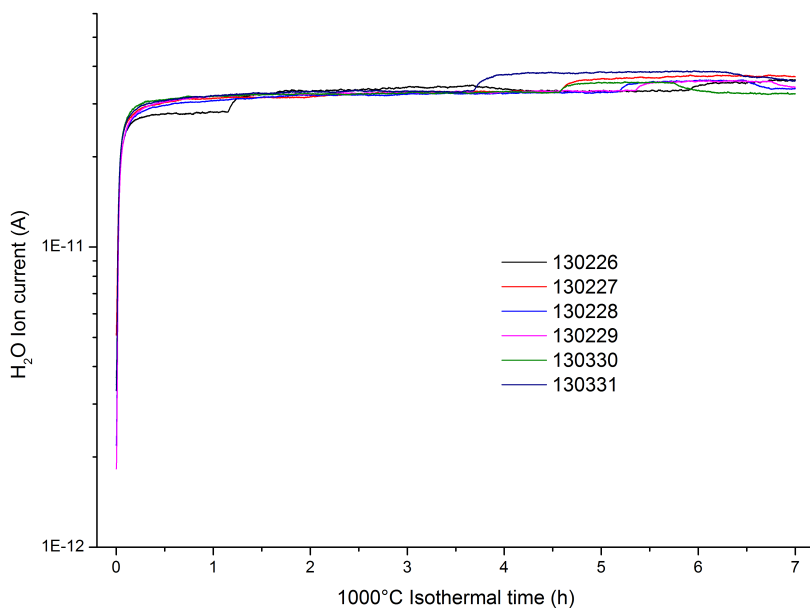
Figure 4.16: *Comparison of H_2O mass spec results for Al1Mn TGA samples 130326 through 130331, from Figures 4.8 through 4.13 H2OMS*
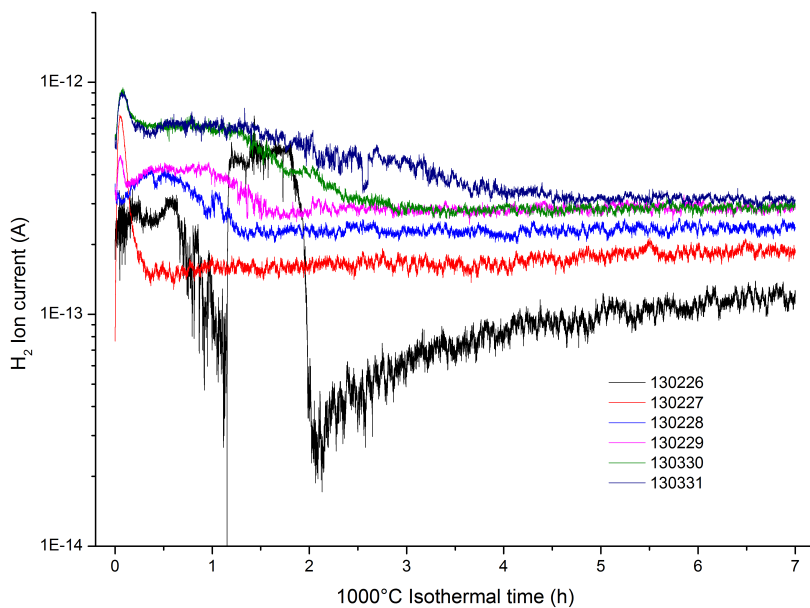
Figure 4.17: *Comparison of H_2 mass spec results for Al1Mn TGA samples 130326 through 130331, from Figures 4.8 through 4.13 H2MS*

4.4 Auger analysis of oxidised Al1Mn TGA samples

Auger analysis[1] was used to investigate the composition of the oxide layer that was formed on two of the Al1Mn TGA samples from [17]. One of the samples had been held at 800℃ in O_2 for 14h (120923 Run#2), and the other sample was held at 1000℃ in CO_2 for 14h (121024 Run#27). The CO_2 sample was one of the two that exhibited the black oxide growths that were discussed in [17], shown in Figure 4.18.
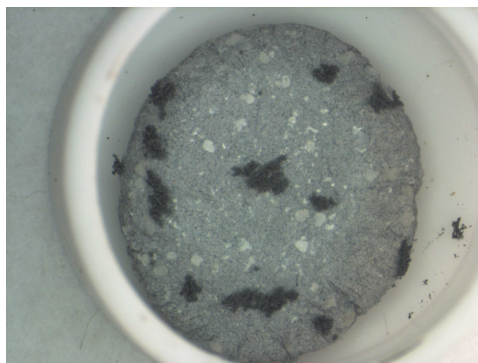
Figure 4.18: *Al1Mn TGA sample heated at 1000℃ for 14h in CO_2, showing black growths. From Wilson [17].*

Figure 4.19 shows the Auger results for Sample 120923 (Al1Mn/O_2/800℃/14h) and Figure 4.20 shows the Auger results for Sample 121024 (Al1Mn/CO_2/1000℃/14h).

Auger analysis showed that:

- Oxide thickness for Sample 120923 in Figure 4.19 ca 800nm
- Oxide thickness for Sample 121024 in Figure 4.20 ca 1900nm
- Mn was not found until a depth of $500nm$ from the surface of the sample
- there was essentially no Mn in the surface $500nm$ of either sample
- the Mn profiles on both samples were similar to the GD-OES results shown in Section 4.1 for the unheated sample material
- Mg oxide nodules were found on the surface of Sample 120923 (Al1Mn/O_2/800℃/14h), but Mg is a very minor component of the original sample alloy

---

[1]Auger analysis was performed by John Walmsley, SINTEF
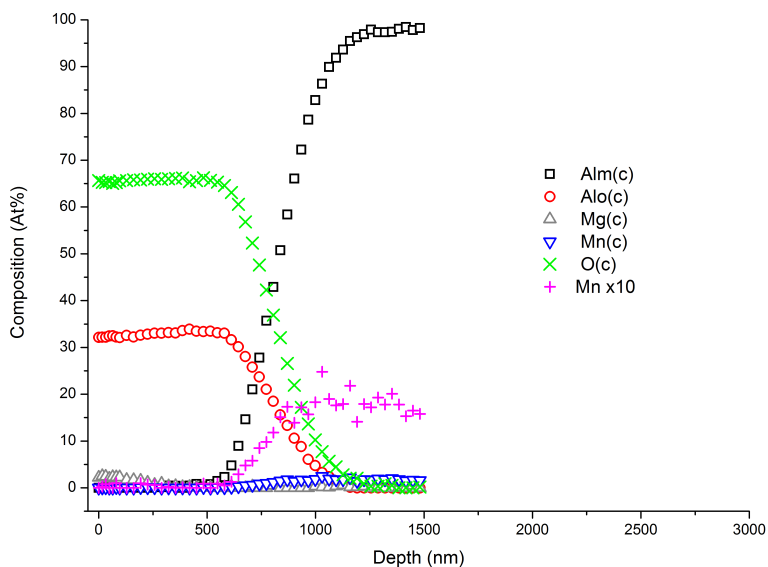
Figure 4.19: *Auger analysis of Al1Mn Sample 120923 heated at 800℃ in O_2 for 14h; sample from [17]*
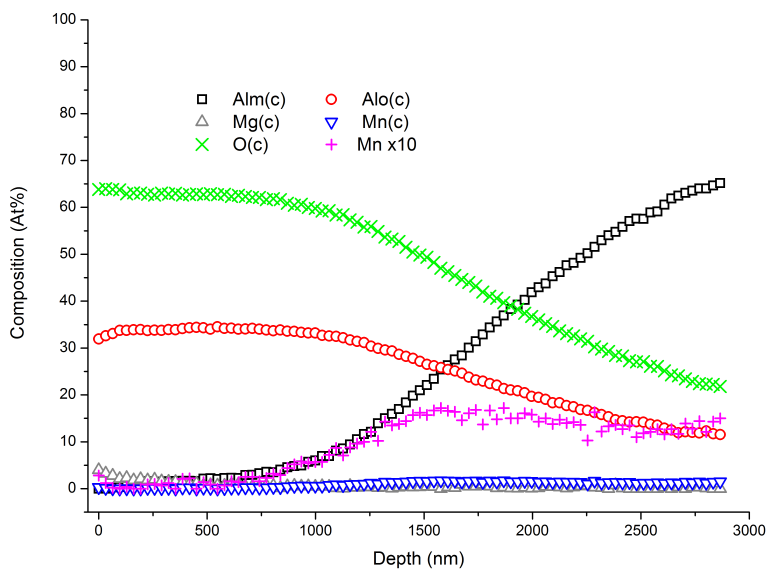
Figure 4.20: *Auger analysis of Al1Mn Sample 121024 heated at 1000℃ in CO_2 for 14h; sample from [17]*

4.5   Muffle furnace oxidation trials

The muffle furnace oxidation trials were divided into three groups; details regarding sample composition, preparation and the heating procedure are discussed in Section 3.3.

4.5.1   Muffle furnace oxidation trials, Group 1: 1000℃

The mass change results for the muffle furnace oxidation of Group 1 (abrasive ground) samples at 1000℃ are shown in Figure 4.21. Samples were removed from the furnace according to the schedule shown in Figure 3.5.
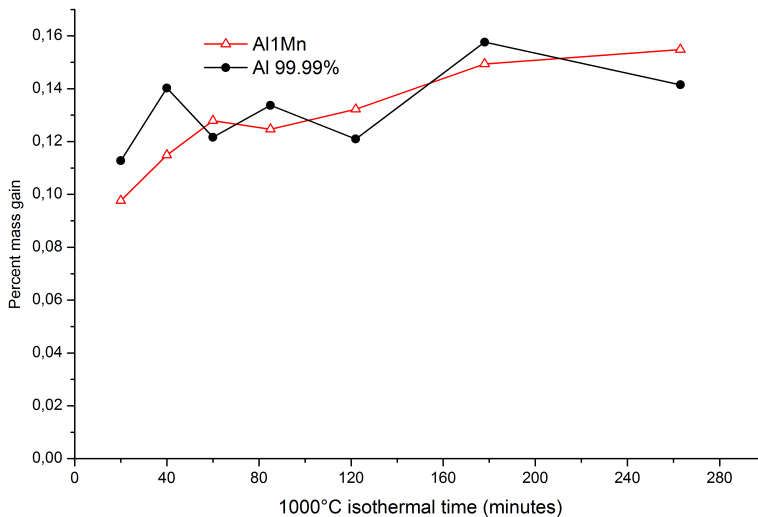
Figure 4.21: *Mass change results for Group 1 40g Al and Al1Mn samples in alumina crucibles heated in a muffle furnace at 1000℃ with air atmosphere. Sample pairs were removed 20, 40, 60, 85, 122, 178 and 263 minutes after melting.*

The greatest mass gain occurred in the first 20 minutes, after which there is a trend of steady mass increase with time, but there is no clear difference in mass gain between the 99.99% Al and Al1Mn materials. The Group 1 samples gained more mass than the Group 2 and Group 3 samples.

4.5.2   Muffle furnace oxidation trials, Group 2: 1200℃

The mass change results for the muffle furnace oxidation of Group 2 (machined) samples at 1200℃ are shown in Figure 4.22. Samples were removed from the furnace according to the schedule shown in Figure 3.6.

There is a distinct difference in mass gain between the different materials in Figure 4.22, with the mass gain (and subsequent loss) increasing with Mn content. The majority of
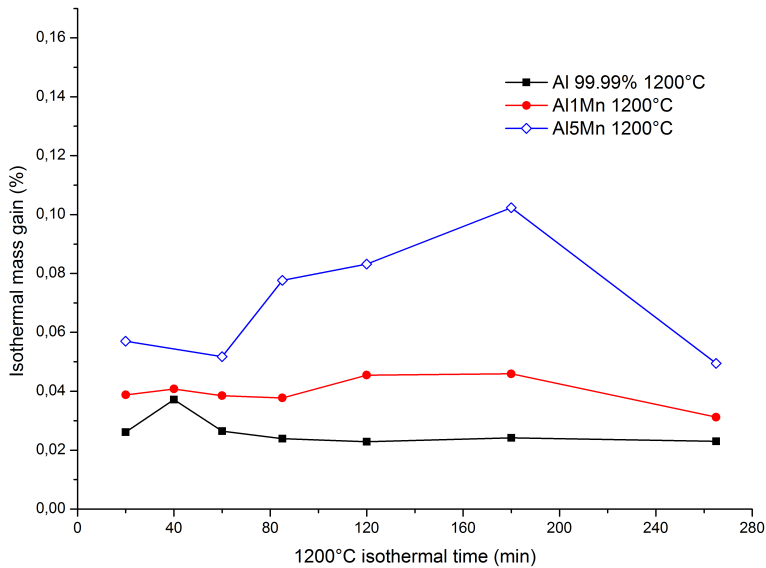
Figure 4.22: *Mass change results for Group 2 35.5g Al, Al1Mn and Al5Mn samples in alumina crucibles heated in a muffle furnace at 1200℃ with air atmosphere. 1200℃ sample triples were removed 20, 40, 60, 85, 120, 180 and 265 minutes after melting.*

the mass gain in 99.99% Al and Al1Mn samples occurs in the first 20 minutes, then the 99.99% Al samples do not gain more mass. The Al1Mn samples gain approximately 0.01% mass from 20 to 85 minutes, only to lose approximately 0.02% mass between 180 and 265 minutes. The Al5Mn samples show approximately 0.06% mass gain at 20 minutes, increasing fairly linearly to 0.10% at 180 minutes. Between 180 and 265 minutes, the Al5Mn samples lose 0.05% mass.

4.5.3 Muffle furnace oxidation trials, Group 3: 1000℃

It was unclear whether the differences between the Group 1 and Group 2 mass gains were due to the different temperature (1000℃ for Group 1 vs. 1200℃ for Group 2), the different sample preparation (Abrasive grinding for Group 1 vs. machining for Group 2), or some other factor such as atmospheric humidity. Therefore, the machined samples in Group 3 were heated at 1000℃ with samples removed from the furnace according to the schedule shown in Figure 3.7. The mass change results for the muffle furnace oxidation of Group 3 samples are shown in Figure 4.23.

The Group 3 samples gained the least mass of the three Groups of 99.99% Al samples. The mass gain at 20 minutes was approximately 0.015%, increasing fairly linearly to approximately 0.03% at 265 minutes.
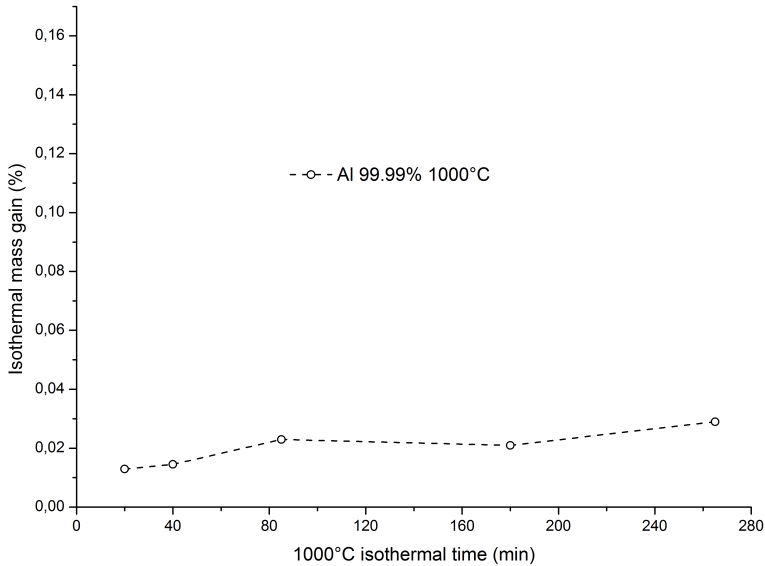
Figure 4.23: *Mass change results for Group 3 99.99%Al samples in alumina crucibles heated in a muffle furnace at 1000℃ with air atmosphere. Samples were removed 20, 40, 85, 180 and 265 minutes after melting.*

4.6 SEM analysis of Group 1 and Group 2 muffle furnace samples

4.6.1 SEM-EDS analysis of Group 1 1000℃ muffle furnace samples

In the SEM, Energy Dispersive x-ray Spectroscopy[2] was performed on the top (oxidized) surface of selected Group 1 muffle furnace samples to quickly determine if there were any obvious differences in the oxide formed for the 99.99% Al and Al1Mn samples that warranted closer inspection.

For these analyses, the muffle furnace samples were simply removed from their crucibles and EDS measurements were taken at two locations on the as-formed top surface of each sample; no sectioning, polishing or carbon coating was done. For each sample, the selection of the two analysis locations was based on areas that appeared different from each other in the SEM. The qualitative results of these analyses are shown in Figures 4.24 through 4.29 and are summarized in Table 4.1

Figures 4.24 and 4.25 show that after 40 minutes at 1000℃ the Al1Mn sample has regions that are somewhat oxidized, while other areas are relatively pure metal.

---

[2]EDS analysis in Section 4.6.1 was done by Wilhelm Dall (SINTEF)

Table 4.1: *Summary of qualitative SEM-EDS results shown in Figures 4.24 through 4.29 for selected Group 1 1000℃ muffle furnace samples*

Time, min	Sample(Location)	Figure	EDS Signal		
			Strong	Moderate	Weak
40	Al1Mn(1)	4.24	Al		O
40	Al1Mn(2)	4.25		Al, O	
263	Al1Mn(1)	4.26	Al, Mg, O	Na	Ca
263	Al1Mn(2)	4.27	Mg, O	Al	Ca, Na
263	99.99% Al(1)	4.28	Al		O
263	99.99% Al(2)	4.29	Al		O, N

The increased oxygen signal for the 263 minute Al1Mn measurements shown in Figures 4.26 and 4.27 indicate that this sample is more heavily oxidized. The 263 minute Al1Mn sample shows high Mg, as well as low to moderate Ca and Na signals that are not present for the 40 minute Al1Mn or 99.99% Al samples.

In Figures 4.28 and 4.29, the 263 minute 99.99% Al sample measurements show only strong Al signals with comparatively weak oxygen and nitrogen signals, indicating that this sample is much less oxidized than the 263 minute Al1Mn sample, but comparable to the 40 minute Al1Mn sample. Since the muffle furnace oxidation was carried out in air, there is a possibility for some minor formation of AlN along with the oxide.
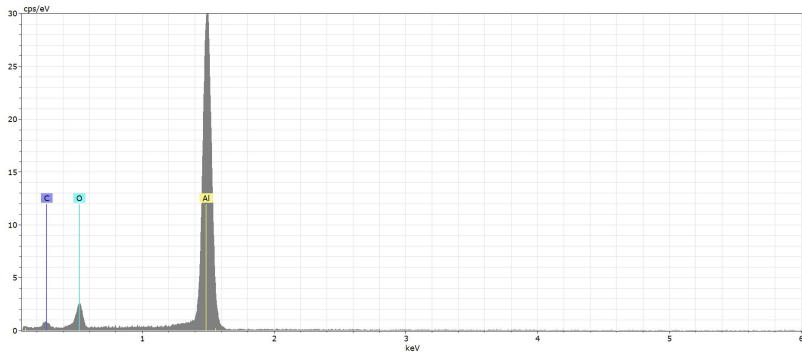
Figure 4.24: *SEM-EDS results for Group 1 Al1Mn 40min/1000℃ muffle furnace sample, EDS analysis location #1*
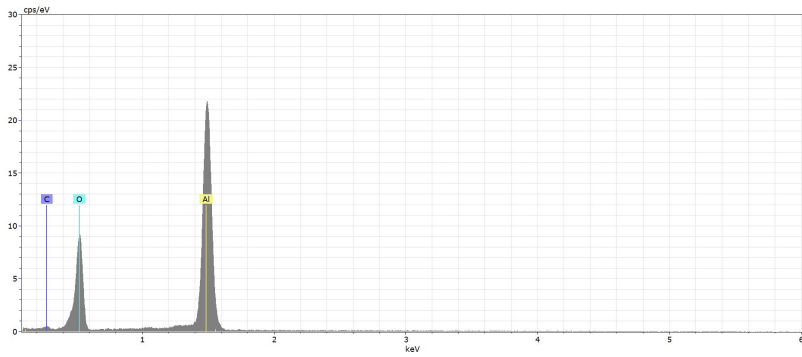
Figure 4.25: *SEM-EDS results for Group 1 Al1Mn 40min/1000℃ muffle furnace sample, EDS analysis location #2*
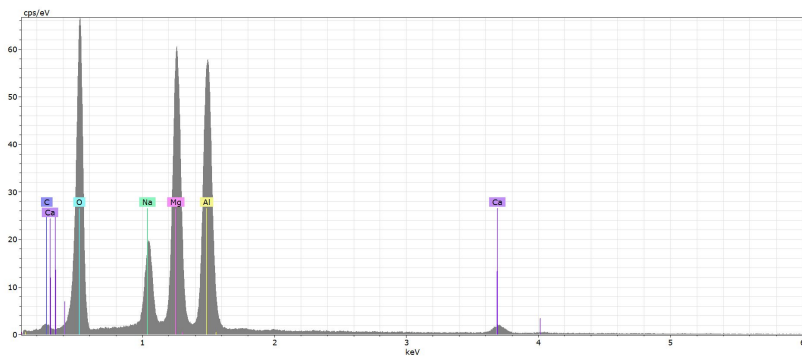
Figure 4.26: *SEM-EDS results for Group 1 Al1Mn 263min/1000℃ muffle furnace sample, EDS analysis location #1*

47
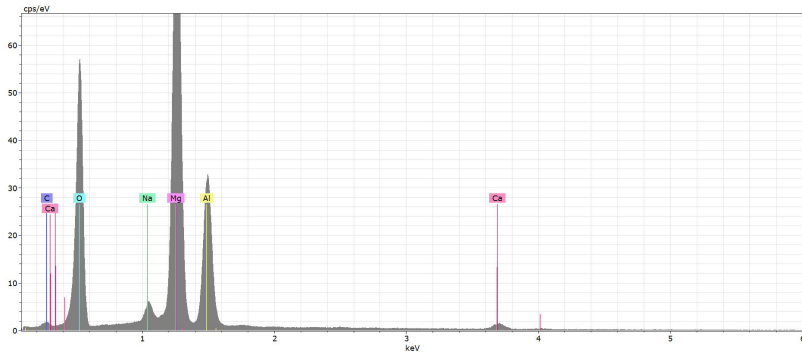
Figure 4.27: *SEM-EDS results for Group 1 Al1Mn 263min/1000℃ muffle furnace sample, EDS analysis location #2*
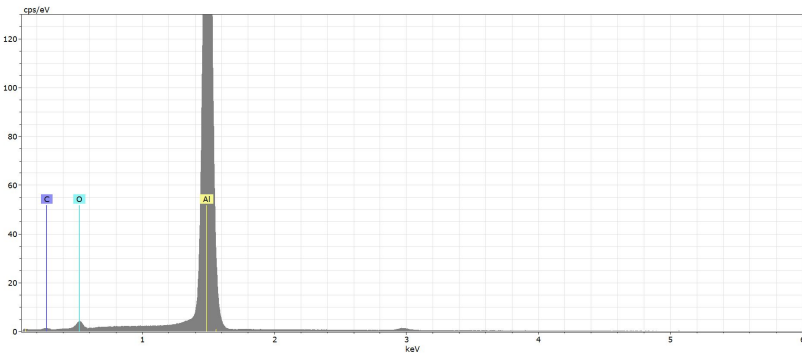
Figure 4.28: *SEM-EDS results for Group 1 99.99% Al 263min/1000℃ muffle furnace sample, EDS analysis location #1*
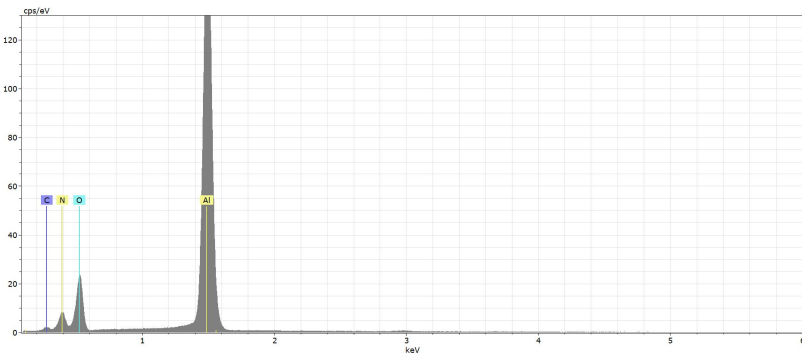
Figure 4.29: *SEM-EDS results for Group 1 99.99% Al 263min/1000℃ muffle furnace sample, EDS analysis location #2*

4.6.2 SEM-SE images of Group 2 1200℃ muffle furnace samples

Sections were cut from the Group 2 muffle furnace samples that were held at 1200℃ for 20 and 265 minutes (the first and last sample for each alloy time-series), then the sections were mounted in epoxy and polished as described in Section 3.4.2. Secondary Electron SEM (SEM-SE) images were taken of the polished cross sections to look at the oxide layer that formed on the top surface of the aluminum in the crucible. Figures 4.30 through 4.35 show selected images that are representative of each sample.

At the bottom of each SEM image there is information regarding the measurement parameters. For example, in Figure 4.30(a) it reads *10.0kV 15.3mm x3.00k SE*; this translates into a $10kV$ electron beam, a working distance of $15.3mm$, an image magnification of $3000x$, and the imaging is using the Secondary Electron mode. In this Figure, each division of the linear scale represents $1\mu m$ on the sample.

Figures 4.30 and 4.31 show the SEM-SE images for the 99.99% Al muffle furnace samples that were held at 1200℃ for 20 minutes and 265 minutes, respectively. The oxide layer on the 20 minute sample is thinner and less fragmented than on the 265 minute sample, and there is less oxide on both of the 99.99% Al samples than on any of the Al1Mn or Al5 Mn samples.

Figures 4.32 and 4.33 show the SEM-SE images for the Al1Mn muffle furnace samples that were held at 1200℃ for 20 minutes and 265 minutes, respectively. The oxide layer on the 20 minute sample is quite different than for the 265 minute sample; there are many small oxide fragments in the 20 minute sample that extend some $10\mu m$ into the bulk, while on the 265 minute sample the fragments appear to have fused together and are concentrated on the surface. However, on both the 20 and 265 minute samples there are "fjords" and "peninsulas" of metal that are surrounded with an oxide layer. Figure 4.33(e) shows an "island" of oxide-encapsulated metal that has become isolated from the bulk.

Figures 4.34 and 4.35 show the SEM-SE images for the Al5Mn muffle furnace samples that were held at 1200℃ for 20 minutes and 265 minutes, respectively. The 20 minute sample has regions in Figures 4.34(c) through (e) where no oxide appears to have formed at all, while Figure 4.34(a) has a region of oxide inclusions some $50\mu m$ deep into the sample. In comparison, the 265 minute sample in Figure 4.35 shows extensive oxide formation, with "fjords" and "peninsulas" similar to those found in the both the 20 and 265 minute Al1Mn sample in Figures 4.32 and 4.33.

In Figures 4.32(e), 4.33(a) and 4.34 there are particles that are likely Al_xMn_y; the composition of these particles was not analyzed. The composition of locations in the 265 minute Al5Mn sample in Figure 4.35(a) were investigated using Energy Dispersive Spectroscopy, and the results are shown in Section 4.6.4.

(a) x3000 X701

(b) x3000 X702

(c) x500 X704

(d) x3000 X706

(e) x3000 X703

(f) x3000 X705
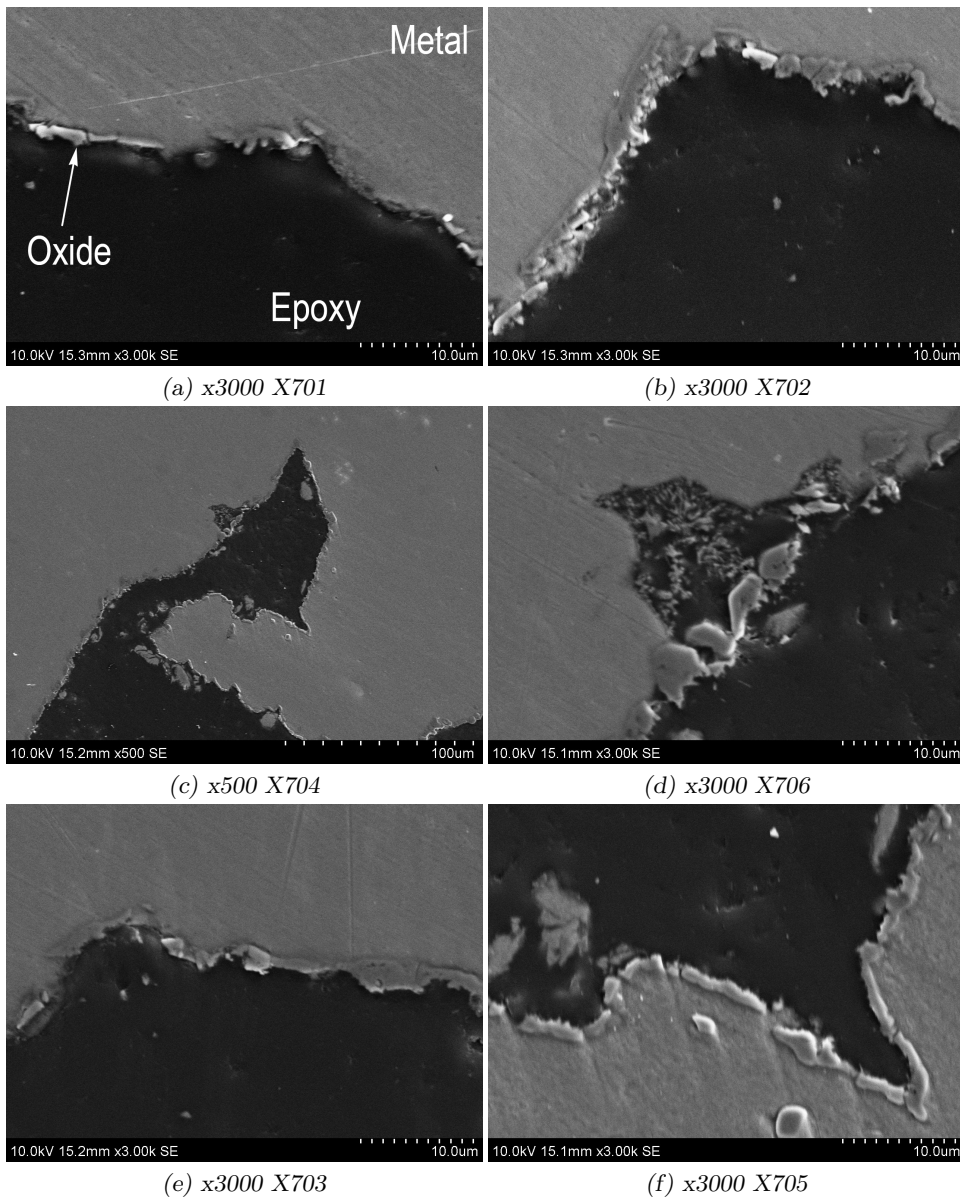
Figure 4.30: *Secondary Electron images of 99.99% Al muffle furnace sample cross-section, 20min at 1200°C. Image (d) is a magnified region from Image (c), the other images are taken at different points along the oxidized surface that are representative of the whole cross-section.*

(a) x3000 X101

(b) x3000 X102

(c) x1200 X108

(d) x900 X103

(e) x3000 X105

(f) x3000 X104
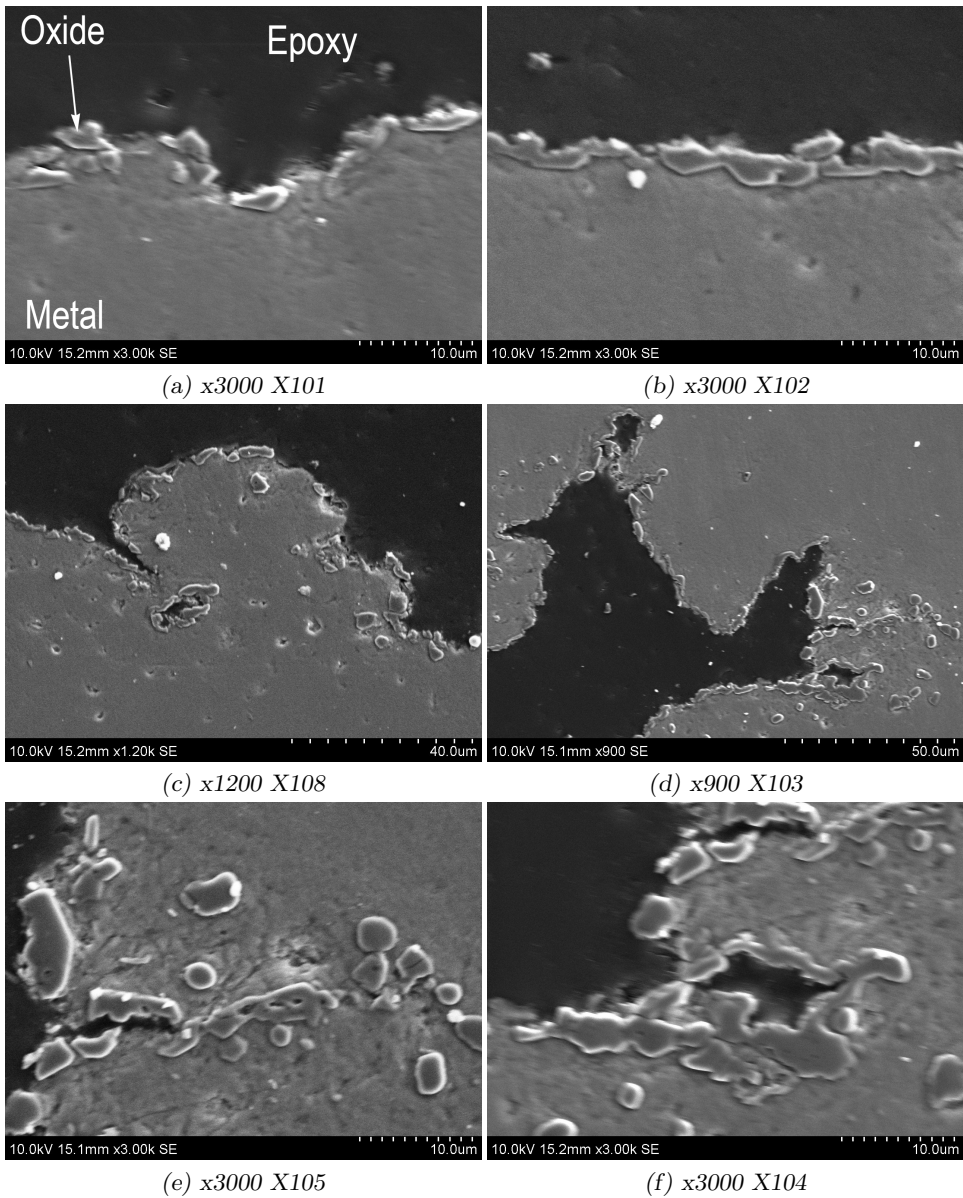
Figure 4.31: *Secondary Electron images of 99.99% Al muffle furnace sample cross-section, 265min at 1200℃. Images (e) and (f) are magnified regions from Image (d).*

(a) x1000 Y711

(b) x3000 Y712

(c) x3000 Y713

(d) x3000 Y719

(e) x1000 Y724

(f) x3000 Y725
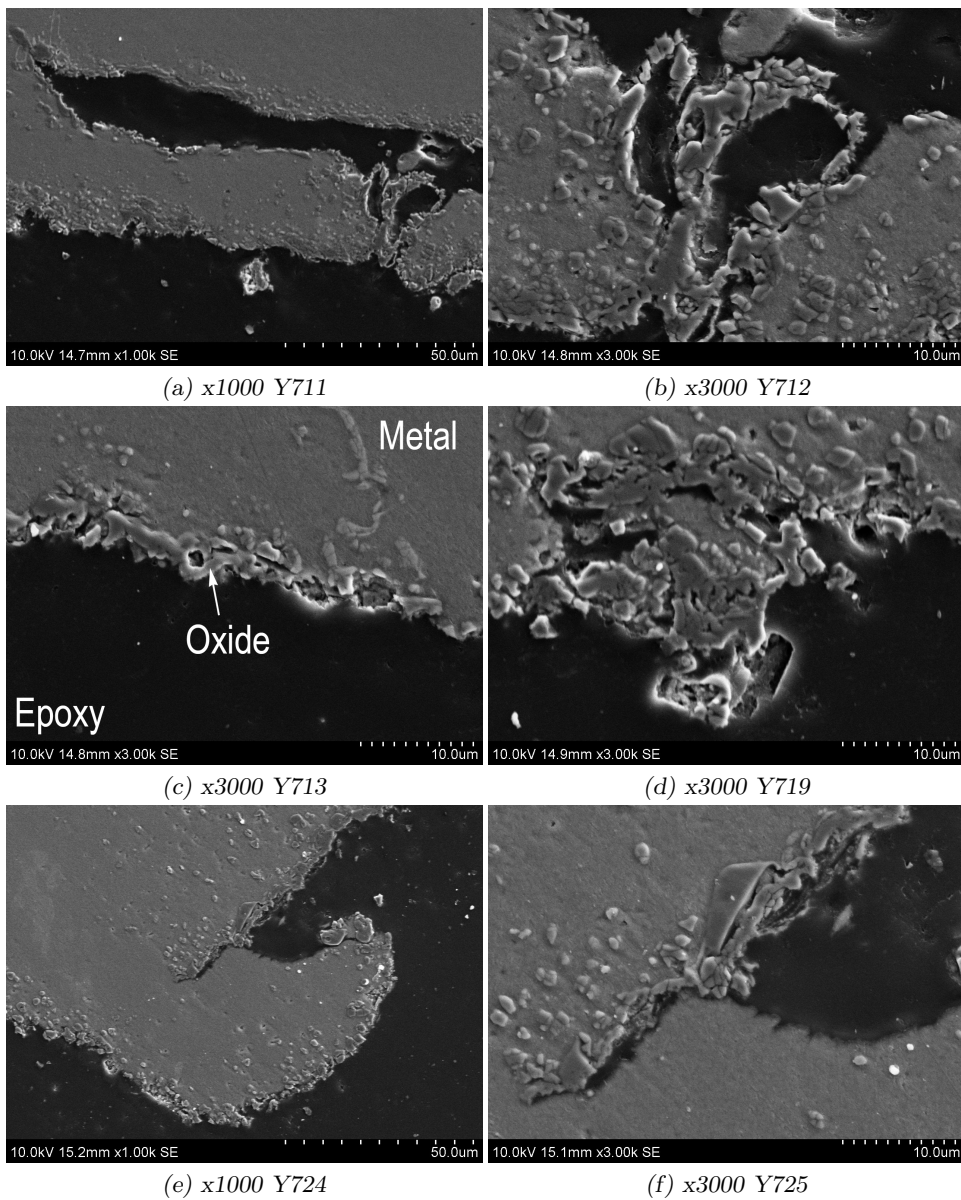
Figure 4.32: *Secondary Electron images of Al1Mn muffle furnace sample cross-section, 20min at 1200℃. Image (b) is a magnified region from Image (a), and Image (f) is a magnified region from Image (e)*

52

(a) x1000 Y1121K

(b) x3000 Y1133K

(c) x1000 Y1031K

(d) x3000 Y1043K

(e) x1300 Y1061P5K

(f) x3000 Y1053K
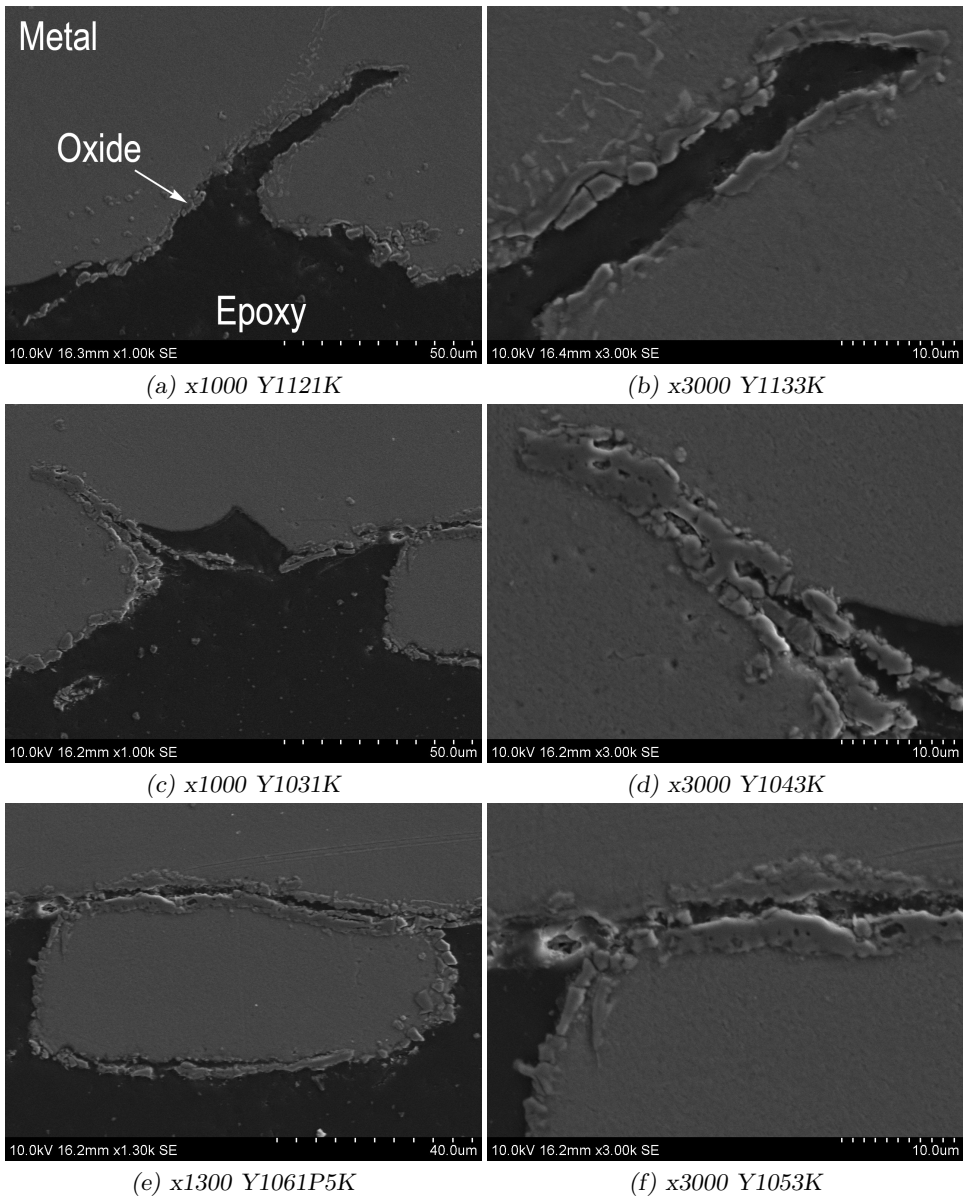
Figure 4.33: *Secondary Electron images of Al1Mn muffle furnace sample cross-section, 265min at 1200℃. The images in the right column are magnified regions from the corresponding images in the left column.*

(a) Z7201K

(b) Z7212p5K

(c) Z7063K

(d) Z7153K

(e) Z7181K

(f) Z7173K
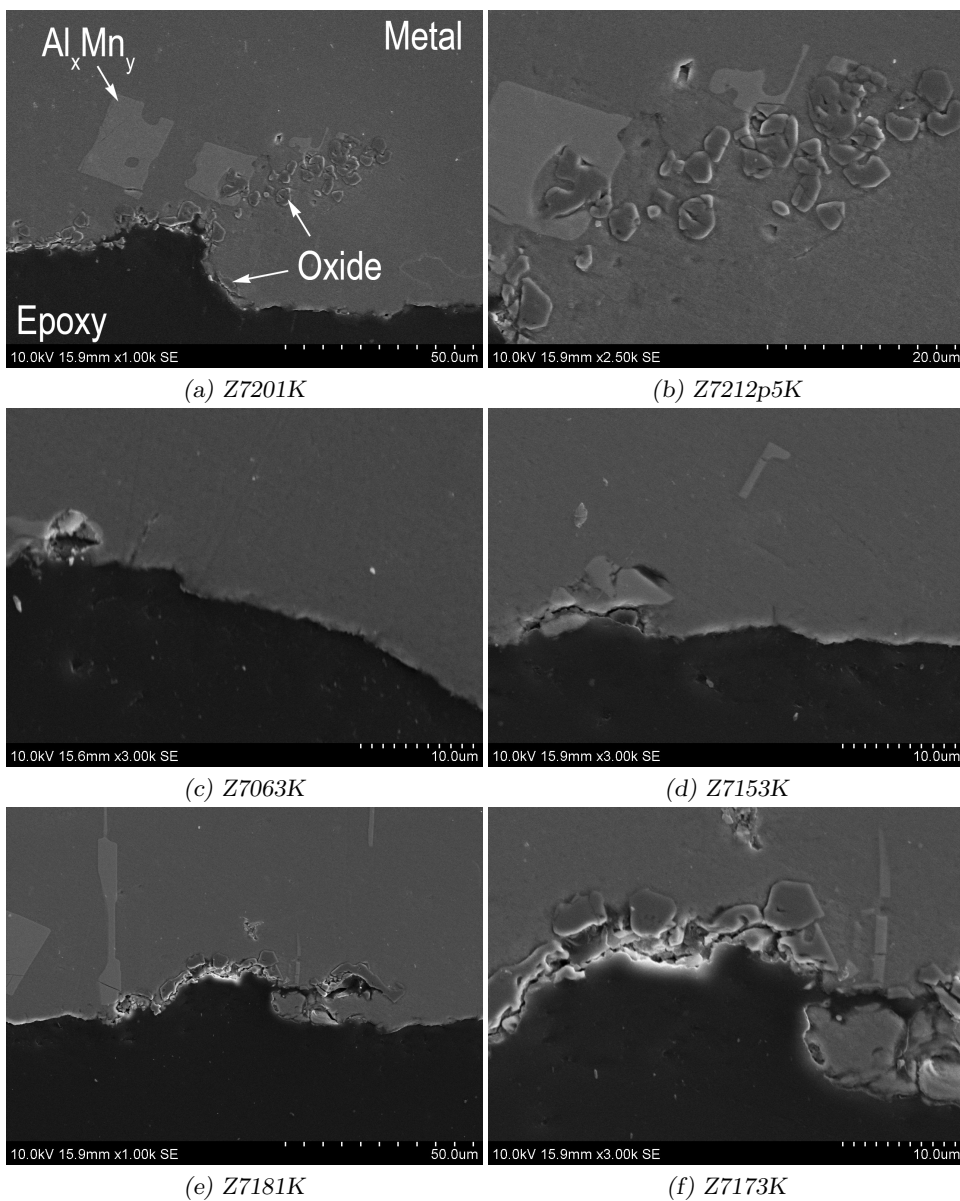
Figure 4.34: *Secondary Electron images of Al5Mn muffle furnace sample cross-section, 20min at 1200℃. Image (b) is a magnified region in Image (a), and Image (f) is a magnified region in Image (e).*

54

(a) Z1010p6K

(b) Z1023K

(c) Z1031K

(d) Z1041K

(e) Z1161K

(f) Z1153K
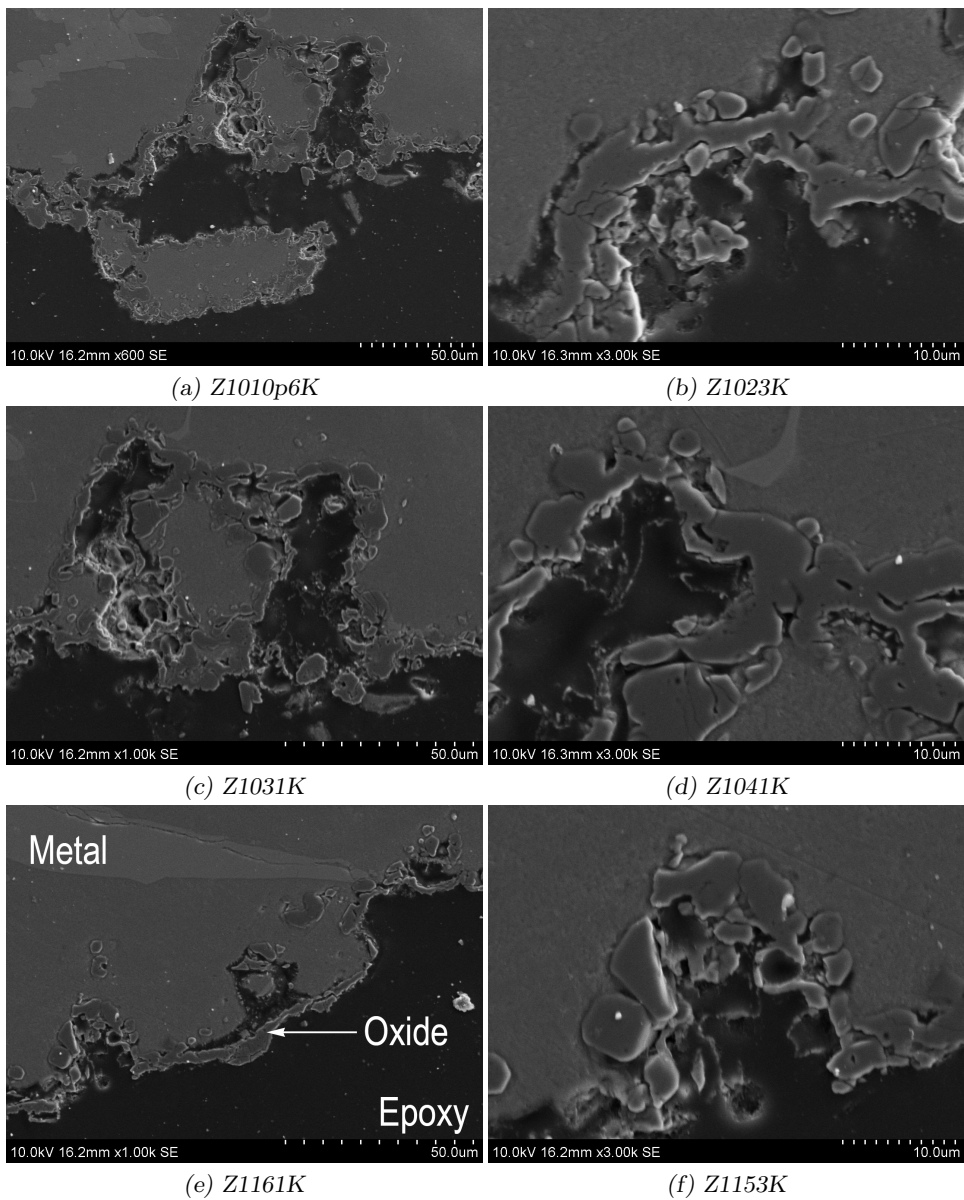
Figure 4.35: *Secondary Electron images of Al5Mn muffle furnace sample cross-section, 265min at 1200℃. Images (b) through (d) are magnified regions from Image (a), and Image (f) is a magnified region from Image (e) Fig:SEMSEZ1*

4.6.3   SEM-EDS analysis of Group 2 Sample Y1

The 265 minute 1200℃ Al1Mn sample cross-section shown in Figure 4.33 was examined using SEM-Energy Dispersive Spectroscopy[3] (SEM-EDS) to investigate the composition of the oxide layer.

Figure 4.36 shows the SEM-SE image of the area that was analyzed using EDS; note that Figures 4.33 and 4.36 show different regions of the same sample cross-section.
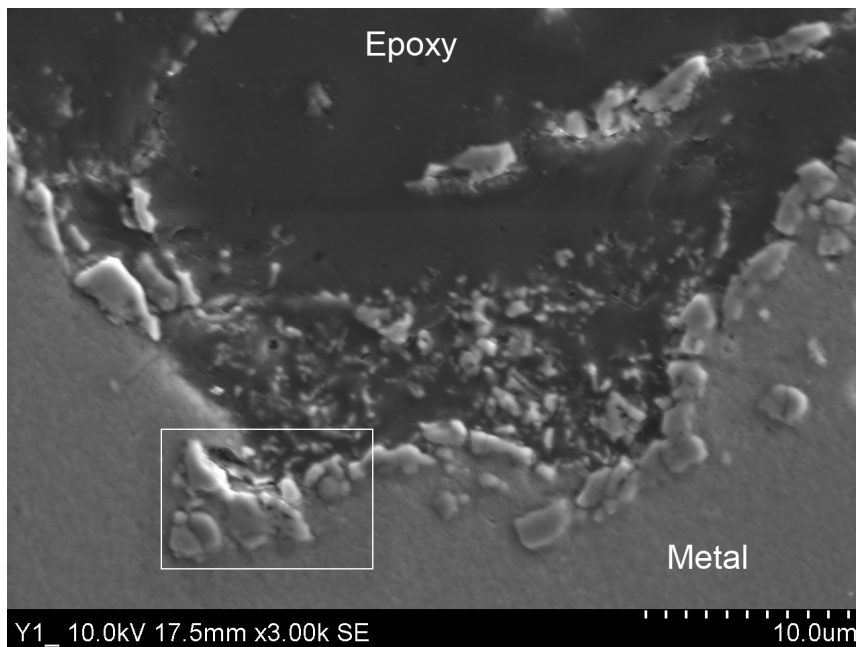
Figure 4.36: *Secondary Electron image of a cross-section of the top surface of Sample Y1. The boxed area was analyzed using EDS and is shown in Figure 4.37. Note that this is a different region of the same sample shown in Figure 4.33. YY1A-02*

Figure 4.37 shows the backscatter SEM (SEM-BS) image of the boxed area shown in Figure 4.36 and Table 4.2 gives the compositions measured at the locations indicated in Figure 4.37.

Heavy elements such as Fe and Mn backscatter (reflect) electrons more strongly than lighter elements such as Al, so the heavier elements show up as brighter spots in SEM-BS images; cf. locations *Y1-4* (contains Fe and Mn) and *Y1-7* (contains only Al and O).

In the oxidized surface of this sample there are regions of aluminum oxide devoid of other metals, interspersed with small clusters where Mn and Fe are concentrated. Location *Y1-2* reflects the bulk composition.

---

[3]SEM-EDS measurements in Sections 4.6.3 and 4.6.4 were conducted by Wilhelm Dall (SINTEF)
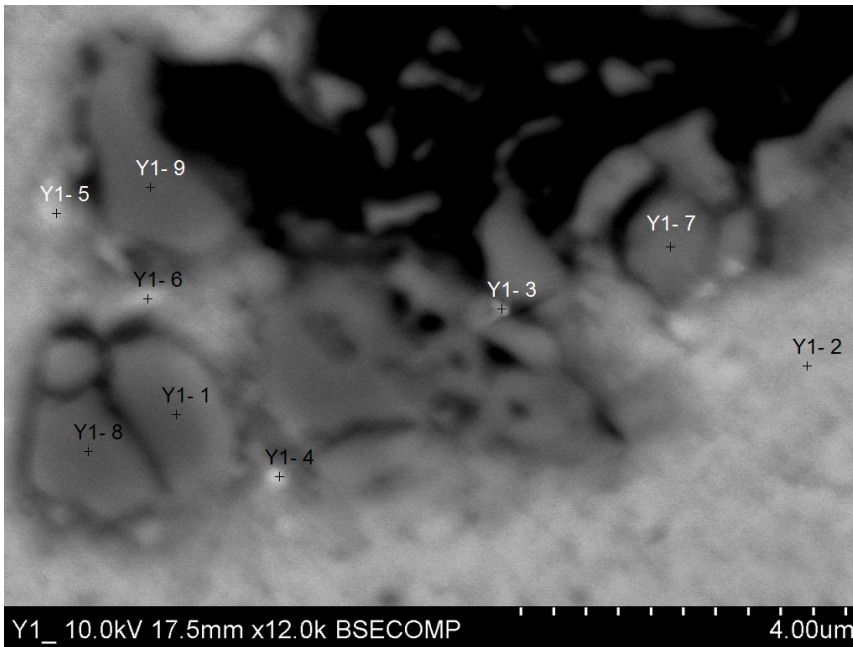
Figure 4.37: *Backscatter image of the boxed area shown in Figure 4.36, showing the SEM-EDS analysis locations; the compositions of these locations are listed in Table 4.2. Fig:EDS-Y1-0109*

Table 4.2: *SEM-EDS normalized compositions in mass% for locations indicated in Figure 4.37. Values for each location do not total 100% due to presence of minor elements and carbon coating on samples. Table:Y1EDS*

Location	Al	O	Mn	Fe	Comment
Y1-1	56.2	38.7			Oxide
Y1-2	88.9	1.2	1.4		Bulk metal
Y1-3	62.0	34.7			Oxide
Y1-4	78.4	5.4	0.8	6.3	Metallic
Y1-5	66.8	23.0	0.8	0.9	Metallic+oxide
Y1-6	72.3	18.4			Oxide
Y1-7	59.2	17.6			Oxide
Y1-8	52.3	42.0			Oxide
Y1-9	52.3	41.7			Oxide

4.6.4 SEM-EDS analysis of Group 2 Sample Z1

Figure 4.38 shows the backscatter SEM image of an area of the Group 2 Al5Mn 265 minute/1200℃ muffle furnace sample cross-section. The interior of the sample contains a large number of particles that are presumed to be enriched in Mn.

The boxed regions were analyzed using EDS; *Area I* is shown in Figure 4.39, *Area II* is shown in Figure 4.40, *Area III* is shown in Figure 4.41 and *Area IV* is shown in Figure 4.42; the EDS analyses accompany each figure. Note that *Area I* was also shown in Figures 4.35(a) through (d) and discussed in Section 4.6.2.
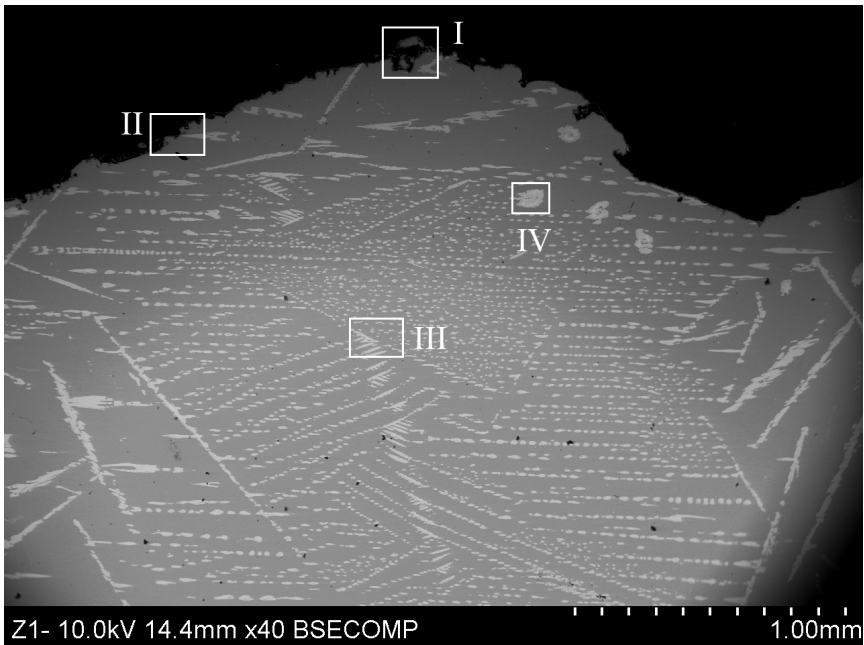
Figure 4.38: *Backscatter SEM image of a cross-section of the top surface of the sample. The boxed areas were analyzed using EDS;* Area I *is shown in Figure 4.39,* Area II *is shown in Figure 4.40,* Area III *is shown in Figure 4.41 and* Area IV *is shown in Figure 4.42. Fig:ZZ1a-05*

Figure 4.39 shows the secondary electron and backscatter images of *Area I* in Figure 4.38. Figure 4.39(b) shows the locations that were analyzed using EDS, and the analysis results are presented in Table 4.3.

There is a thick oxidized layer present on the surface, and in Figure 4.39(b) there are small particles interspersed throughout the oxide that are presumed to be enriched in Mn or Fe. There are also large particles visible in the bulk that likely contain Mn.
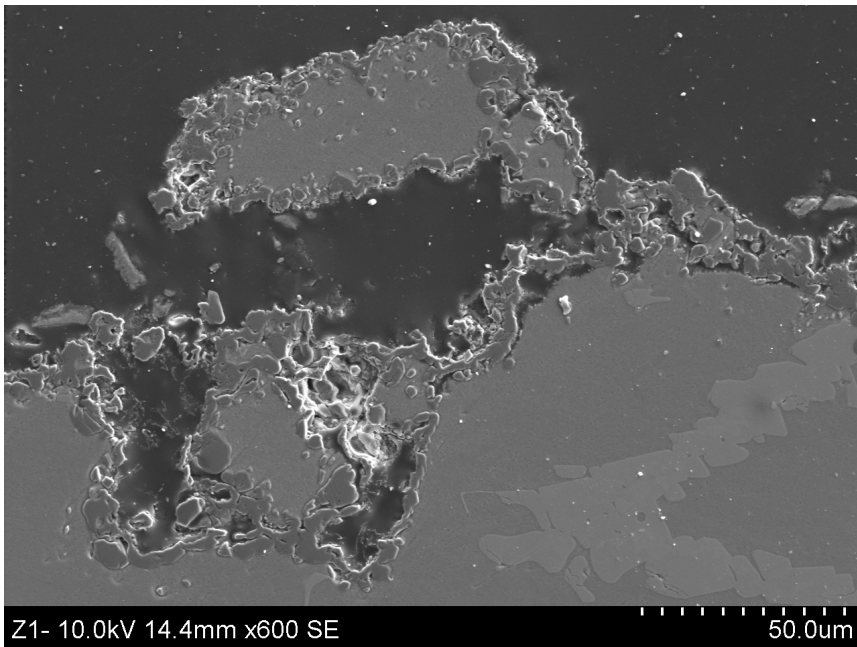
(a) Secondary Electron
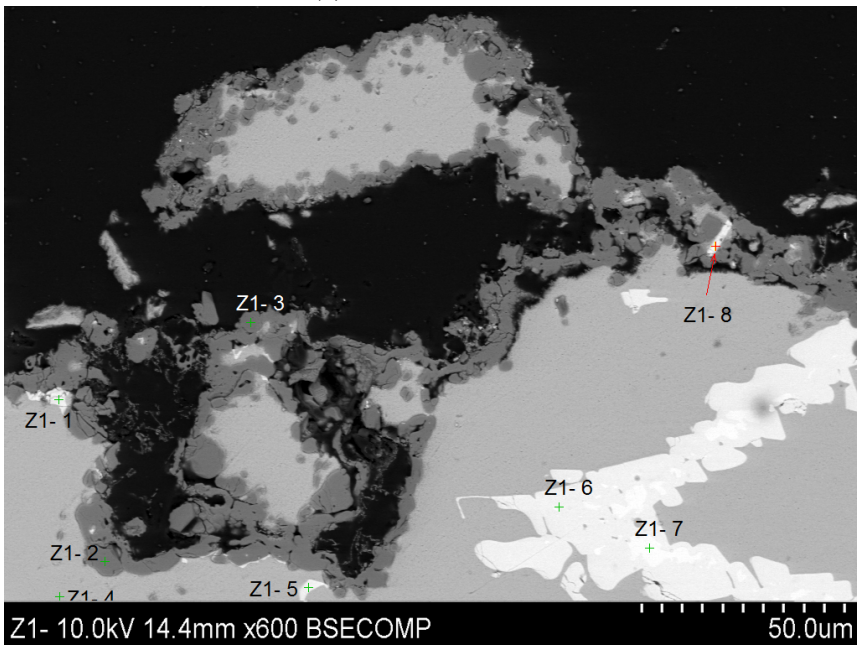
(b) Backscatter image showing EDS analysis locations

Figure 4.39: *SE (a) and backscatter (b) images of Area I in Figure 4.38, showing SEM-EDS analysis locations. Fig:EDSsecI*

Table 4.3: *SEM-EDS normalized compositions in mass% for locations shown in Figure 4.39(b). Values for each location do not total 100% due to presence of minor elements and carbon coating on samples. Table:Z1EDSI*

Location	Al	O	Mn	Fe	Comment
Z1-1	63.27		27.31		Metal in oxide layer
Z1-2	54.52	40.89			Oxide layer
Z1-3	54.37	41.30			Oxide layer
Z1-4	90.39	0.86	2.13		Bulk metal
Z1-5	64.54		21.61	6.90	Metal particle in bulk
Z1-6	65.37		28.21		Metal particle in bulk
Z1-7	62.16		31.36		Metal particle in bulk
Z1-8	62.76		30.05		Metal in oxide layer

Locations *Z1-2* and *Z1-3* are darker than the bulk metal in Figure 4.39(b), and the EDS results in Table 4.3 show that these areas are nearly pure aluminum oxide. Locations *Z1-1* and *Z1-8* are small bright particles in the oxide layer, and have Mn concentrations approximately 6x that of overall alloy.

Location *Z1-4* should represent the bulk concentration; this EDS measurement is lower in Mn than the overall Al5Mn alloy. The values in Table 4.3 are normalized and the Mn concentration outside the particles will be lower because of the amount of Mn that is bound up in particles.

There is a large particle in the lower right corner of Figure 4.39(b), where measurements *Z1-6* and *Z1-7* were taken. The brightness of the particle at location *Z1-7* indicates a higher Mn concentration than at location *Z1-6*; this is reflected in the measurements in Table 4.3 and suggests there could be two different Al_xMn_y phases here.

Figure 4.40 shows the secondary electron and backscatter images of *Area II* in Figure 4.38. The EDS measurements for the locations shown in Figure 4.40(b) are presented in Tables 4.4 and 4.5.
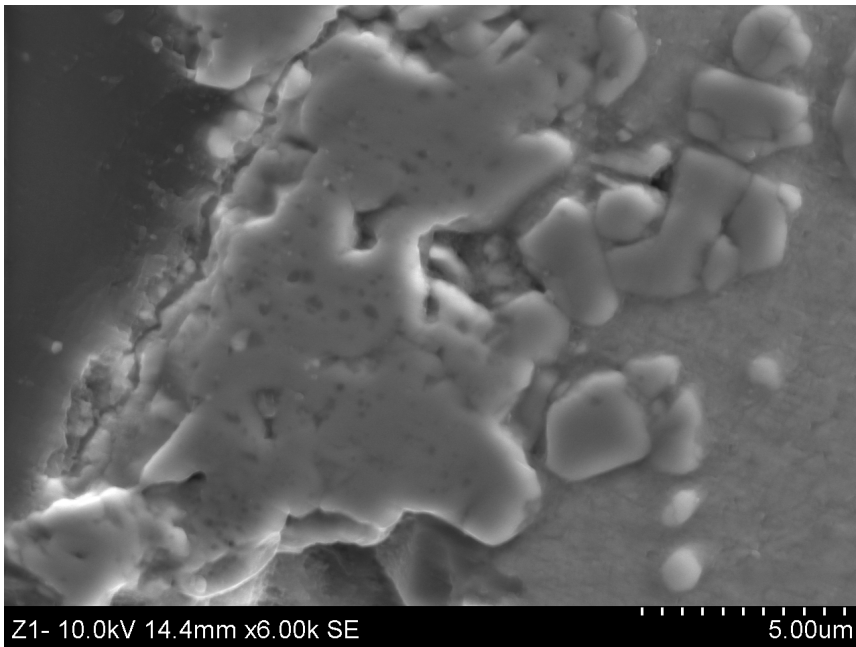
(a) Secondary Electron
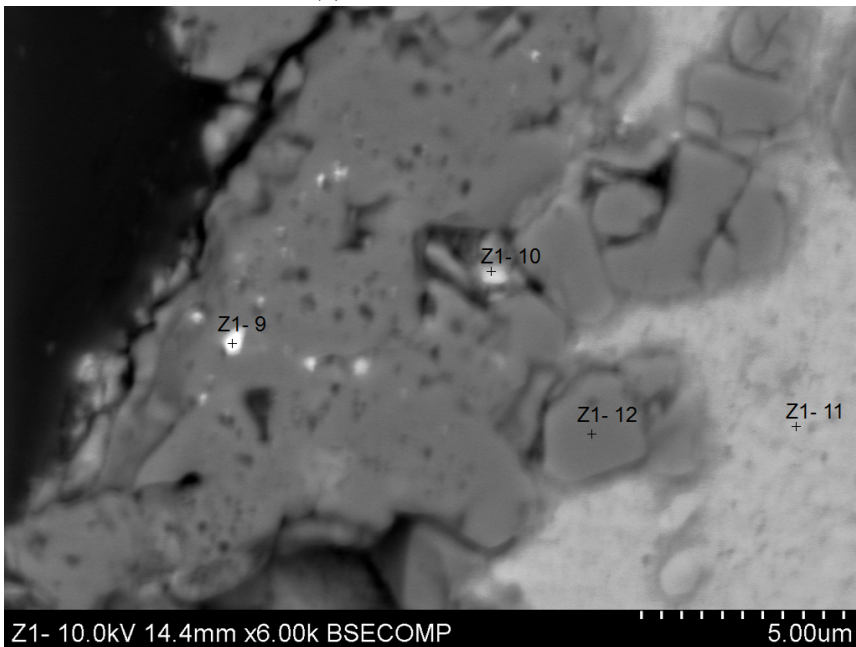
(b) Backscatter image showing EDS analysis locations

Figure 4.40: *SE (a) and backscatter (b) images of* Area II *in Figure 4.38. Figure 4.40(b) shows the EDS measurement locations in Tables 4.4 and 4.5 Fig:EDSsecII*

Figure 4.40(b) indicates that locations *Z1-9* and *Z1-10* are small particles of heavier elements in the oxide layer. From Table 4.4, location *Z1-9* contains Mn and O, in addition to Si, Mo, Cr, Fe, V, Ti and Cu. These additional elements were not significant components of the original alloy.

Table 4.4: *SEM-EDS normalized compositions in mass% for location Z1-9 shown in Figure 4.40(b). Values for each location do not total 100% due to presence of minor elements and carbon coating on samples. Table:EDSZ1A2.1*

Al	O	Mn	Si	Mo	Cr	Fe	V	Ti	Cu
17.15	13.03	9.10	28.89	13.48	3.18	2.88	2.06	2.04	1.23

Table 4.5 shows that location *Z1-10* is also enriched in Mn, but does not contain the other metallic elements found at location *Z1-9*. There are other, smaller bright spots in the oxide layer in Figure 4.40(b), but the composition of these spots were not measured with EDS. Location *Z1-11* is unoxidized metal, and location *Z1-12* is only aluminum oxide.

Table 4.5: *SEM-EDS normalized compositions in mass% for locations shown in Figure 4.40(b). Values for each location do not total 100% due to presence of minor elements and carbon coating on samples.Table:EDSZ1A2.2*

Location	Al	O	Mn	Comment
Z1-10	71.91	10.77	7.06	
Z1-11	88.17	1.27	1.71	
Z1-12	54.26	40.99		Oxide

Figure 4.41 shows the backscatter image of *Area III* in Figure 4.38 and the locations of the EDS measurements presented in Table 4.6.
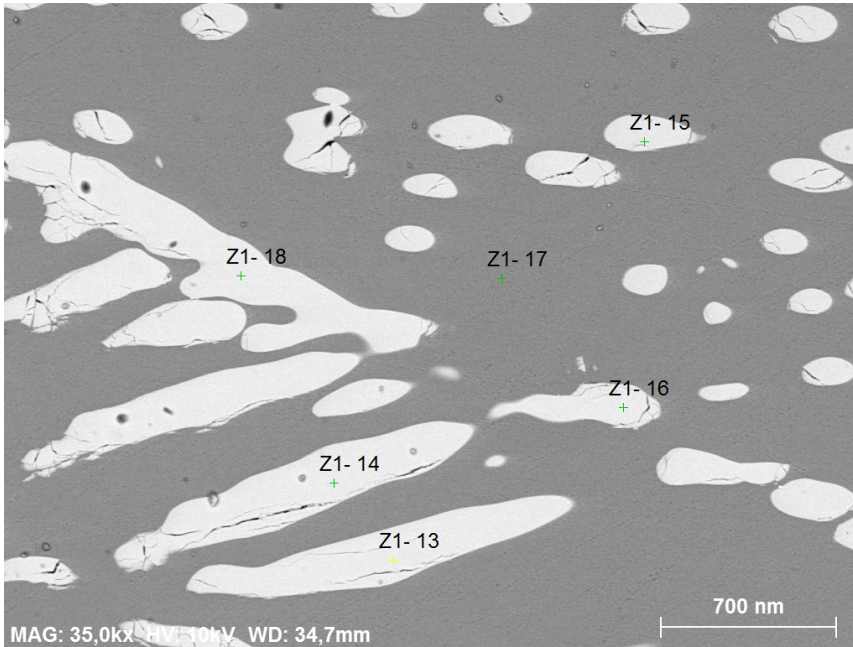
Figure 4.41: *Backscatter image of* Area III *in Figure 4.38. EDS analysis compositions are listed in Table 4.6. EDS-Z1-1318*

The backscatter overview of the sample interior shown in Figure 4.38 showed that the interior of the sample had a high concentration of particles that formed along various grain boundaries. Figure 4.41 shows a magnified view of the particles in the matrix. There is very little variation in the brightness of locations *Z1-13* through *Z1-16* and *Z1-16*; the EDS analysis in Table 4.6 shows that these locations all have similar Mn content. Location *Z1-17* has a comparatively low Mn content due to the Mn bound up in the particles.

Table 4.6: *SEM-EDS normalized compositions in mass% for locations shown in Figure 4.41. Values for each location do not total 100% due to presence of minor elements and carbon coating on samples. Table:EDSZ1A3*

Location	Al	Mn
Z1-13	70.93	29.07
Z1-14	64.15	29.43
Z1-15	65.71	27.68
Z1-16	64.83	28.67
Z1-17	90.48	2.12
Z1-18	65.65	27.79

Figure 4.42 shows the backscatter SEM image of *Area IV* in Figure 4.38. The compositions of the EDS analysis locations in Figure 4.42 are given in Table 4.7.
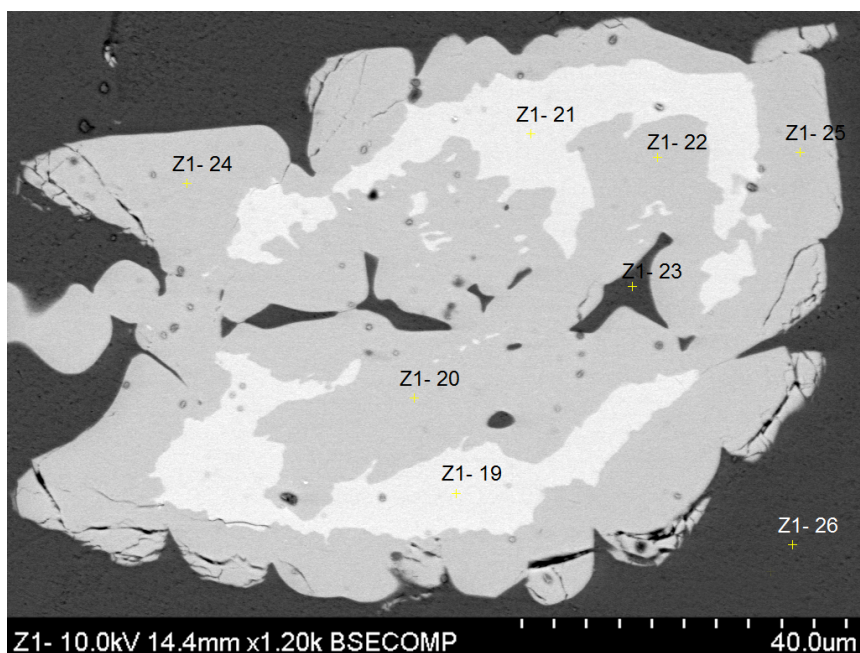
Figure 4.42: *Backscatter image of* Area IV *in Figure 4.38, showing the EDS analysis locations; compositions are listed in Table 4.7. EDS-Z1-1926*

Similar to Figure 4.41, this particle contains a high concentration of Mn. The backscatter image suggests the stoichiometry of the areas within the particle are different; locations *Z1-19* and *Z1-21* are in the brightest area and have similar compositions in Table 4.7, and locations *Z1-20,Z1-22,Z1-24* and *Z1-25* have similar compositions. Locations *Z1-25* and *Z1-25* have similar compositions and represent the low-Mn metal.

Table 4.7: *SEM-EDS normalized compositions in mass% for locations shown in Figure 4.42. Values for each location do not total 100% due to presence of minor elements and carbon coating on samples. EDSZ1A4*

| Location	Al	O	Mn	Comment
19	58.40		35.38	Mn-rich phase 1
20	64.64		28.88	Mn-rich phase 2
21	56.15		37.88	Mn-rich phase 1
22	65.81		27.57	Mn-rich phase 2
23	88.77	0.88	3.14	
24	66.24		27.14	Mn-rich phase 2
25	63.35		30.25	Mn-rich phase 2
26	88.98	1.07	1.96	

5. Discussion

5.1 GDOES discussion

The GD-OES results in Section 4.1 confirm findings from [17], that Mn is not present on the surface of the Al1Mn extruded strip.

The results for the as-extruded and surface-cleaned samples are very similar, in that the oxide layer is approximately $6 - 12nm$ thick, while the Mn-depleted zone extends some $100nm$ into the surface.

It is not unreasonable that the as-extruded sample was depleted in Mn, since it was subjected to the heat, pressure and material flow of the extrusion process and this may well affect the surface chemistry. However, it was unexpected that the samples with the surface $50\mu m$ removed would have a Mn profile nearly identical to that of the as-extruded samples. The surface cleaning process should have removed all of the Mn-depleted material and the bulk Mn concentration should have been measured at the surface, just below the $6nm$ thick oxide layer.

The surface cleaning process was performed at room temperature and the samples were not subjected to any elevated temperatures before they were measured with GD-OES some 3-5 days later.

From this, it appears that the Mn either (a) evaporates from the surface at room temperature, or (b) diffuses *away* from the surface.

Using data from Table 2.3 in Equation (2.8), the vapour pressure of Mn at 25℃ is calculated:

$$log(P/atm) = 12.805 + \frac{-15097}{298} - 1.7896 \ log(298) = -42.28 \tag{5.1}$$

$$\boxed{P_{Mn}^{vap} = 5.2 \times 10^{-43} atm} \tag{5.2}$$

The vapour pressure of Mn at room temperature is so low that evaporation from the surface should not be possible. Further, Mn diffusion at room temperature occurs much too slowly for the Mn concentration profile in the cleaned samples to be nearly identical to the as-extruded samples after only a few days, and diffusion *toward* an area of higher concentration should not be thermodynamically possible. Therefore, some other mechanism must be at play that is not currently understood.

5.2 Thermogravimetric oxidation

The results for the series of six cleaned Al1Mn TGA oxidation samples at 1000℃ in N_2+ 7 mol% H_2O in Figure 4.14 showed consistent results for five of the samples, but Sample 130227 showed considerably more mass gain even though all of the experimental variables were identical. This series of six experiments was conducted to compare with TGA results from Wilson [17] for as-extruded Al1Mn under similar experimental conditions, shown in Figure 5.1.

In [17] the results for the 800℃ samples were quite consistent whether there was water vapour present or not, while at 1000℃ there was more scatter in the results, especially when water vapour was added. However, there were not enough parallels run in [17] for any one experimental combination of temperature, time and presence of water vapour to draw any firm conclusions as to the reason for the scatter.
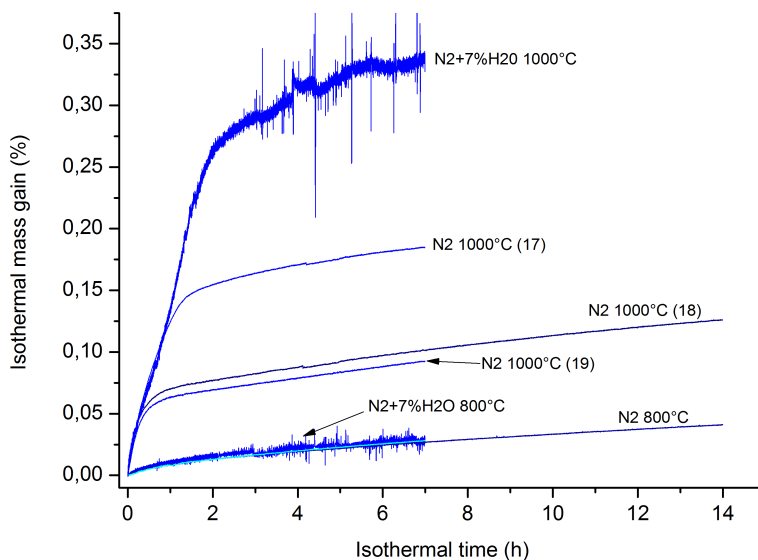
Figure 5.1: *TGA results for as-extruded Al1Mn samples in N_2, from [17]. Fig:MPN2All*

When the current results in Figure 4.14 are compared to those in Figure 5.1, the cluster of five samples in Figure 4.14 have approximately the same mass gain at the end of 7 hours as Samples 18 and 19 in Figure 5.1. However, the majority of the mass gain for the cleaned Al1Mn samples in Figure 4.14 occured in the first 30 minutes, after which the mass gain more or less stopped. Samples 18 and 19 in Figure 5.1 also gained mass quickly in the first half hour, then over the next 30 minutes the mass gain became nearly linear with time. Note that all of the samples in Figure 4.14 had an atmosphere containing water vapour, while Samples 18 and 19 in Figure 5.1 were dry.

In both Figures 4.14 and 5.1, the samples with maximum mass gain had N_2 atmospheres with 7 mol% H_2O and showed somewhat similar mass gain behaviour; the mass gains in the first 30 minutes were at approximately the same rate as the other samples in the respective series, but both samples continued gaining mass at a high rate for approximately

the first 90 minutes. In the TGA data for sample 130227 in Figure 4.9 the peak in the H_2 mass spectrometer signal is significantly larger and much more defined than for any of the other TGA samples in Figures 4.9 through 4.13 and indicates rapid, or "breakaway" oxidation as discussed in Section 2.1.3. This breakaway oxidation appears to happen somewhat randomly, and once it begins it seems to take considerable time before the oxide layer that is forming stabilizes and starts to protect the molten metal.

5.2.1 TGA baseline subtraction error analysis

The TGA measurement mass change data are meaningless until the systematic error from the machine - the baseline - is subtracted. In this work, baselines were conducted with the identical heating program and gas composition/flow parameters used for the respective sample measurements, with an empty sample crucible. Further, when a series of identical measurements were conducted, the same baseline was subtracted from each of the experiments. For the baseline subtraction:

$$m_{sample} = m_{measurement} - m_{baseline} \qquad (5.3)$$

The error in the sample mass change is calculated using Equation (2.55):

$$(\delta m_{sample})^2 = (\delta m_{measurement})^2 + (\delta m_{baseline})^2 \qquad (5.4)$$

The "large range" for the TGA microbalance was used in this work; from Table 2.5 the uncertainty in each mass measurement is $\pm 0.4 \mu g$, so the total measurement uncertainty is

$$\delta m_{sample,TGA} = \sqrt{(0.4\mu g)^2 + (0.4\mu g)^2} = 0.5657\mu g \qquad (5.5)$$

$$\boxed{\delta m_{sample,TGA} = \pm 0.6\mu g} \qquad (5.6)$$

The thermogravimetric mass change data in this work is normalized as a percentage of the original sample mass prior to heating:

$$\Delta m_{sample,\%} = 100 \frac{\Delta m_{sample}}{original\ sample\ mass} \qquad (5.7)$$

To convert the measurement uncertainty to use in the mass change figures,

$$\delta m_{sample,TGA}, \% = 100 \frac{\pm 0.6\mu g}{original\ sample\ mass} \qquad (5.8)$$

Then from Equation (2.56), the uncertainty in the normalized sample mass change is given by

$$\left(\frac{\delta m_{sample}, \%}{\Delta m_{sample}, \%} \right)^2 = \left(\frac{\delta m_{sample,TGA}}{\Delta m_{sample}} \right)^2 + \left(\frac{\delta m_{M36S}}{m_{sample\ before}} \right)^2 \qquad (5.9)$$

In the Results, Figure 4.14 showed the series of six TGA measurements of the cleaned Al1Mn discs in $N_2 + 7\%H_2O$ at 1000℃; Table 5.1 summarizes the mass change data.

Table 5.1: *Sample mass and baseline-corrected mass gain data for TGA samples shown in Figure 4.14. Sample masses were measured with Sartorius M36S microbalance before TGA oxidation*

Sample	Sample mass, M36S $\pm 0.002 mg$	Corrected mass gain, TGA $\pm 0.4 \mu g$	%
130326	209.960	168.9	0.080
130327†	212.842†	513.7†	0.241†
130328	210.993	157.4	0.075
130329	211.515	161.5	0.076
130330	210.496	167.0	0.079
130331	208.016	154.1	0.074
Average	210.196	161.8	0.077
St. Dev	1.348	6.2	0.003

† Sample 130327 not included in average and standard deviation calculations

Five of the measurements were nearly identical when the baseline was subtracted, but the mass change for sample 130327 was much greater than for the other five measurements in that series, and is not included in the average and standard deviation calculations. The data shows an average mass gain of $161.8 \mu g$ with little scatter, but to determine if these differences are significant an estimate of the total measurement uncertainty is needed.

Equation (5.9) is used to calculate the normalized TGA measurement uncertainty by using the result from Equation (5.6), the average sample mass and % mass gain values from Table 5.1 and the M36S measurement uncertainty from Table 2.5:

$$\delta m_{sample}, \% = 0.077\% \sqrt{\left(\frac{0.6 \mu g}{161.8 \mu g}\right)^2 + \left(\frac{2 \mu g}{210196 \mu g}\right)^2} \tag{5.10}$$

$$\boxed{\delta m_{sample}, \% = \pm(2.85 \times 10^{-5})\%} \tag{5.11}$$

The result in Equation (5.11) shows that the uncertainty in the TGA measurements after the baseline (systematic error) is subtracted is insignificant compared to the variation between the results of each measurement. Therefore, the difference between each sample is due to changes in the samples, and not measurement error.

5.2.2 Oxide Thickness

The average thickness of the oxide that formed on the TGA samples can be calculated using the method outlined in Section 2.2. The calculated values can be compared against physical measurements using, for example, Auger analysis. Table 5.2 lists relevant properties of Al and Al_2O_3 that are used in the calculation.

Table 5.2: *Properties of Al and Al_2O_3[2]*

Property	Value	Units
M_{Al}	27	kg/kmol
M_O	16	kg/kmol
$M_{ox} = M_{Al_2O_3}$	102	kg/kmol
$\rho_{met} = \rho_{Al}$	2700	kg/m^3
$\rho_{ox} = \rho_{Al_2O_3}$	3950	kg/m^3

The samples are disc-shaped, Ø8.5 x 1.6mm, so the geometric surface area is

$$A = \pi D \left(\frac{D}{2} + h \right) = 1.56 \times 10^{-4} \, m^2$$

$$\boxed{A = 1.56 \times 10^{-4} \, m^2} \tag{5.12}$$

The mass fraction of oxygen in Al_2O_3 is

$$y = \frac{3M_O}{M_{Al_2O_3}} = \frac{3(16)}{2(27) + 3(16)}$$

$$\boxed{y = 0.47} \tag{5.13}$$

Equation (2.16) gives the oxide film thickness as a function of mass gain:

$$\Delta \ell_{ox} = \frac{1}{y \, \rho_{ox}} \frac{\Delta m}{A} = \frac{\Delta m}{(0.47)(3950)(1.56 \times 10^{-4})}$$

$$\boxed{\Delta \ell_{ox} = 3.448 \Delta m, \; \left[\frac{m}{kg} \right]} \tag{5.14}$$

where Δm is the mass of the oxide film. The oxide-metal boundary displacement from Equation (2.19):

$$\Delta \ell_{met} = (1 - y) \frac{\rho_{ox}}{\rho_{met}} \Delta \ell_{ox} = (1 - 0.47) \frac{3950}{2700} \Delta \ell_{ox}$$

$$\boxed{\Delta \ell_{met} = 0.775 \Delta \ell_{ox}} \tag{5.15}$$

In Wilson[17], sample 120923 was held at 1000°C for 14h in 100% O_2, and gained $219\mu g$ over the course of the experiment. Using Equation (5.14) and assuming the oxide growth is the same on all surfaces of the sample, the expected change in oxide thickness would then be

$$\Delta \ell_{ox} = 3.448(2.19 \times 10^{-7} kg) = 7.55 \times 10^{-7} m$$

$$\boxed{\Delta \ell_{ox} = 755nm} \tag{5.16}$$

The actual oxide-metal boundary displacement from Equation (5.15) is then

$$\Delta \ell_{met} = 0.775(7.55 \times 10^{-7} m) = 5.85 \times 10^{-7} m$$

$$\boxed{\Delta \ell_{met} = 585nm} \tag{5.17}$$

In addition, Wagner [16] states that the following factors seem important to determine the structure of an oxide layer:

1. degree of porosity and coherency
2. chemical composition
3. crystallographic structure
4. crystallographic orientation
5. variation of properties with increasing distance from the oxide film-metal interface

5.2.3   Discussion of Auger analysis results

The Auger analysis results in Section 4.4 showed the measured oxide thickness as a function of depth for two as-extruded Al1Mn TGA samples from Wilson [17]. The sample in Figure 4.19 had an oxide thickness of approximately 800nm, and in [17] this sample gained $219\mu g$ during the TGA oxidation. Based on this mass gain, the calculations in Section 5.2.2 predict that an oxide layer an average thickness of of $755nm$ should have formed on the sample, in addition to the pre-existing $17-18nm$ of natural oxide measured with GD-OES [17] for a total oxide thickness of approximately $775nm$, which agrees well with the Auger results.

Similarly, the sample in Figure 4.20 had an oxide thickness of some $1900nm$ and gained $377\mu g$ during the TGA oxidation. Using Equation (5.14) this should translate into an average "fresh" oxide thickness of $1300nm$, and when the preexisting $17-18nm$ of natural oxide is added, a total of approximately $1320nm$ of oxide. This, however, does not agree with the Auger results.

5.3 Muffle furnace oxidation

5.3.1 Muffle Furnace Oxidation Error Analysis

As with the TGA results, the muffle furnace oxidation mass gains are very small so minor measurement errors in can have a large influence on the final result. Error analysis was performed on the muffle furnace mass gain data as outlined in Section 2.6 to determine the magnitude of the measurement error.

The simplest case in this work involves measuring the mass of a sample before and after it is heated in a muffle furnace:

$$\Delta m_{sample} = m_{sample\,after} - m_{sample\,before} \tag{5.18}$$

The error in Δm_{sample} is calculated using Equation (2.55):

$$(\delta m_{sample})^2 = (\delta m_{sample\,before})^2 + (\delta m_{sample\,after})^2 \tag{5.19}$$

The Sartorius BP301S microbalance was used to measure the masses of the samples before and after they were heated in the muffle furnace. Using the uncertainty in Table 2.5, the error in the mass change calculation is

$$\delta m_{sample,BP301S} = \sqrt{(0.2mg)^2 + (0.2mg)^2} = 0.2828mg \tag{5.20}$$

$$\boxed{\delta m_{sample,BP301S} = \pm 0.3mg} \tag{5.21}$$

In order to directly compare samples with different masses, the mass change is normalized using the sample mass before heating

$$\Delta m_{sample}, \% = 100 \frac{\Delta m_{sample}}{m_{sample\,before}} \tag{5.22}$$

Equation (5.22) also has an assocated error, according to Equation (2.56):

$$\left(\frac{\delta m_{sample}, \%}{\Delta m_{sample}, \%} \right)^2 = \left(\frac{\delta m_{sample,BP301S}}{\Delta m_{sample}} \right)^2 + \left(\frac{\delta m_{BP301S}}{m_{sample\,before}} \right)^2 \tag{5.23}$$

For muffle furnace sample 1A, the sample mass before heating was approximately $40.4mg$ and the mass change measured on the BP301S balance was 62.6 mg. Using Equation (5.22) the normalized mass change was 0.155%. The error in the normalized mass change is

$$\delta m_{sample\,1A}, \% = 0.155\% \sqrt{\left(\frac{0.3mg}{62.6mg} \right)^2 + \left(\frac{0.2mg}{40424.9mg} \right)^2} \tag{5.24}$$

$$\boxed{\delta m_{sample\,1A}, \% = \pm(7.43 \times 10^{-4})\%} \tag{5.25}$$

Equation (5.25) shows that the uncertainty in the measurement is small compared to the magnitude of the normalized mass change, and Figure 5.2 shows the muffle furnace oxidation results along with their uncertainties.

5.3.2   Muffle furnace mass gain

Table 3.1 lists the differences between the three groups of muffle furnace oxidation samples. The mass gain results in Section 4.5 showed a significant variation between Group 1, and Group 2 and 3 materials; the results for the three groups are compared in Figure 5.2.
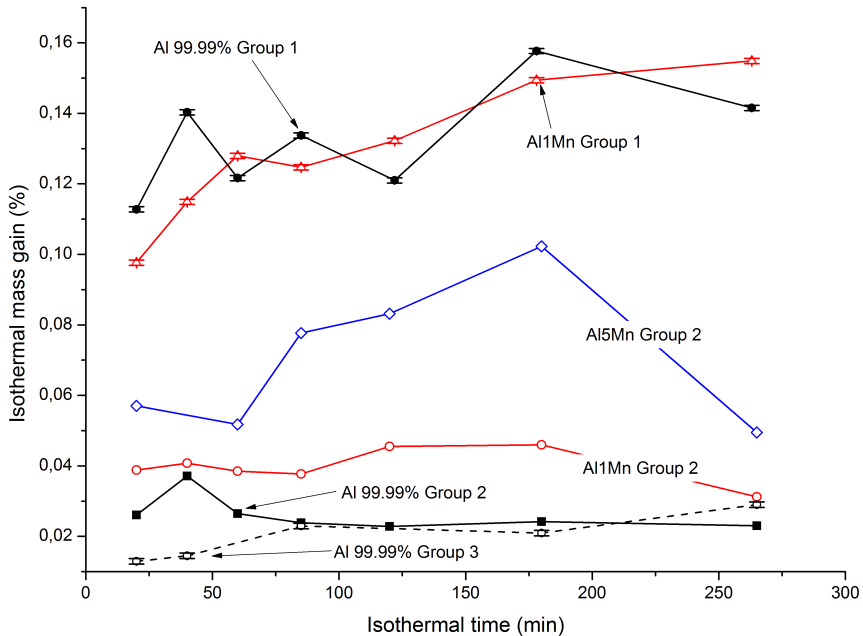
Figure 5.2: *Comparison of Groups 1-3 muffle furnace oxidation mass gain results from Figures 4.21 through 4.23. Samples marked (G) were prepared by grinding with an abrasive belt, samples marked (M) were prepared by machining. Fig:MufFurnDiscuss*

The Group 2 1200℃ Al and Al1Mn and Group 3 samples gained approximately one fifth as much mass as the Group 1 1000℃ Al and Al1Mn samples, the opposite of what would be expected from the increased temperature. All of the samples for the muffle furnace experiments came from the same ingots of the respective alloys, and 99.7% alumina crucibles were used for all of the experiments, so the chemical composition of the experimental materials should be nearly identical.

The furnace atmosphere was approximately the same, apart from minor differences in atmospheric humidity. Table 5.3 shows the outdoor atmospheric conditions during the respective muffle furnace experiments. The indoor humidity conditions were not measured, so it is assumed that the water content of the indoor air was not significantly different than that of the outdoor air.

Comparing the atmospheric conditions between the three groups of experiments shows that there were small differences in the mole fraction (partial pressure) of atmospheric water vapour. Molten aluminum dissociates water vapour according to Equation (2.12) to form alumina and hydrogen. If this effect was significant, the Group 3 materials

Table 5.3: *Atmospheric humidity during muffle furnace experiments. Outdoor temperature and relative humidity data retrieved from local weather service, water content values from* Carrier Psychrometric Chart for Normal Temperatures, *Appendix B.*

Samples	Outdoor temp ℃	RH %	H_2O content $gH_2O/kg\ dry\ air$	Mol frac H_2O
Group 1	-2.3 ± 1.1	40 ± 2	1.3 ± 2	0.002
Group 2	13.7 ± 0.8	50 ± 3	4.7 ± 4	0.007
Group 3	11.2 ± 1.1	72 ± 6	6.1 ± 0.4	0.010

should have gained more mass than the Group 1 materials, given the same temperature. Therefore it must be concluded that there are other factors at play.

Apart from the furnace temperature and small differences in water vapour, the largest difference between the three groups of samples was sample preparation. Impey [7] reviewed a variety of work which indicated that the sample preparation method was an important factor in the amount of oxidation, and that oxide weight gain increased with increasing surface roughness.

The very similar mass gains of the 99.99% Al samples in Groups 2 and 3 show that the sample preparation is more important than either furnace temperature or minor changes in humidity.

The Group 1 samples were shaped and weight-matched using a 60 grit abrasive belt which left these samples with a strongly textured surface, i.e. many deep scratches. This surface texture gives a significantly larger surface area in relation to the geometric area that provides much more area for oxidation to take place.

The Group 2 and 3 samples were prepared together, and the machining processes used to prepare these samples left a much smoother surface finish that would give much less surface area for oxidation than on the Group 1 samples.

The surface texture and roughness of the samples was not measured so it is not known what the relative surface areas were for the different groups of samples.

The mass losses seen with the Group 2 Al1Mn and Al5Mn samples is likely due to the relatively high vapour pressure of Mn at 1200℃. Figure 2.2 and Table 2.4 show that at 1200℃, Mn has a vapour pressure of 7.7×10^{-4} atmospheres. The evaporation of Mn at this temperature would be slow, but would probably be measurable.

5.3.3 Muffle furnace SEM and SEM-EDS

In Section 4.6, cross-sections from the oxide layer and top few millimetres of metal from selected Group 2 muffle furnace samples were inspected in the SEM after oxidation. It was found that the 99.99% Al samples had only a thin layer of oxide on the surface that was relatively coherent, while the oxide on the Al1Mn and Al5Mn samples was thicker, much more fragmented and contained small particles of Mn and other metals. As identified in the Results, the oxide layers on Mn-containing samples contained "islands" of metal surrounded by oxide and "fjords" or deep cracks in the surface that also had oxide skins

in them. In the muffle furnace, the surfaces of the molten samples were not agitated in any way that could lead to oxide formation, except when removing the samples from the furnace. In an industrial remelting furnace where the bath is in motion, it is conceivable that the tendency to form small islands of metal surrounded by oxide could easily lead to formation of large oxide particles with metal locked up inside. This oxide would then be removed from the furnace as dross.

In all of the samples that contained Mn, and indeed, all of the samples in the current work, none of the samples have contained Mn on the surface as a component in the oxide. EDS analysis of the samples showed that the oxide particles only contain Al and O, but there were small particles of Mn-containing metal scattered across the surface.

5.4 Oxidation model

One goal of this work is to develop a kinetic model for the oxidation of Al-Mn alloys. The basis for the mathematical portion of the model is described in Section 2.5, but parameters such as a diffusion coefficient are needed, and curve fitting was used in an attempt to determine values for these parameters.

5.4.1 TGA curve fitting on Al1Mn experimental data

The approach taken in curve fitting was to try different general models that are described in literature [12] as being relevant to oxidation kinetics, and to examine the residual plot for each proposed model to evaluate the fit. The residual for each data point for a set of time-based data are defined as

$$residual(t) = data(t) - model(t)$$

When the correct model and parameter values are found for a set of data, the residuals should ideally be evenly and randomly distributed about $y = 0$ and should have no discernable pattern. If there is a clear trend or pattern in the residuals this means that the model does not adequately describe the data.

When fitting models to experimental data it is generally accepted that the simplest model is the best, especially when attempting to correlate the model to physical phenomena. For example, it may be possible to fit a 10-parameter model to the data perfectly, but the model will likely have no physical meaning. Further, simple models have been identified that have specific meanings in respect to kinetics [12] - linear relationships indicate reaction controlled kinetics, parabolic equations are used to describe diffusion controlled reactions, and so on.

Curve fitting on TGA data for Al1Mn in O_2 at 1000°C from [17] was used to try to find a kinetic model that agreed with the experimental data. Figure 5.3 shows the generic shape of different models that are discussed in literature [12].

At first glance it should seem possible to fit a relatively simple kinetic model to the TGA data to, for example, determine diffusion coefficients and time constants that can be used in the diffusion model from Section 2.5, but this has proven to be challenging.

5.4.1.1 First approach: fitting all data

In an attempt to find a model that fit the TGA data, the curve fitting function in *Origin 8* was used. Numerous built-in functions were tried, and the best fit for the entire set of data was using a two-part exponential function of the form

$$mass\ gain\ /mg = A1\ e^{\frac{-t\ /s}{B1}} + A2\ e^{\frac{-t\ /s}{B2}} + C$$

For the case of the Al1Mn alloy at 1000°C in O_2 [17], Figure 5.4(a) shows the increase in oxide thickness vs. time is described reasonably well by the equation

$$mass\ gain = \left\{ -2.44\ e^{\frac{-t}{51111}} - 4.57\ e^{\frac{-t}{530}} + 7.34 \right\} \times 10^{-7} [mg] \qquad (5.26)$$
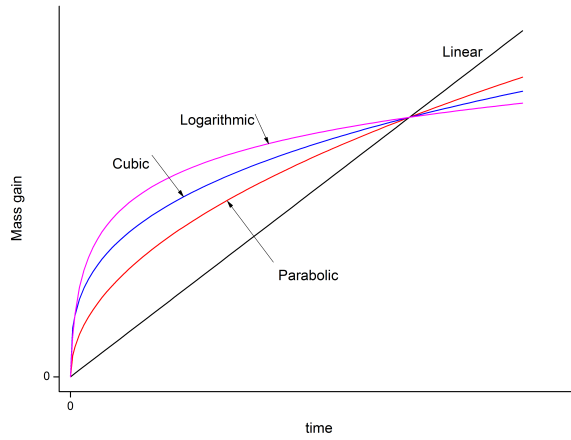
Figure 5.3: *Generic shape of different oxidation models [12] Fig:GenModels*

but the obvious pattern in the residual plot in Figure 5.4(b) shows that this model does not adequately describe the data, especially in the first two hours. Interpretation of this model and how to apply it in the context of oxidation kinetics is also difficult, since the oxidation was expected to follow parabolic kinetics. Simple parabolic and cubic models of the form

$$mass\ gain_{parabolic} = A_1\sqrt{A_2(t + \tau_1)} + A_3(t + \tau_2) + C$$
$$mass\ gain_{cubic} = A_1\sqrt[3]{A_2(t + \tau_1)} + A_3(t + \tau_2) + C$$

were also tried, but the best fits that could be achieved with either of these models were worse than for the exponential decay model. It is apparent from this that there is something more complex going on than can be described with a single equation, and another approach is needed.
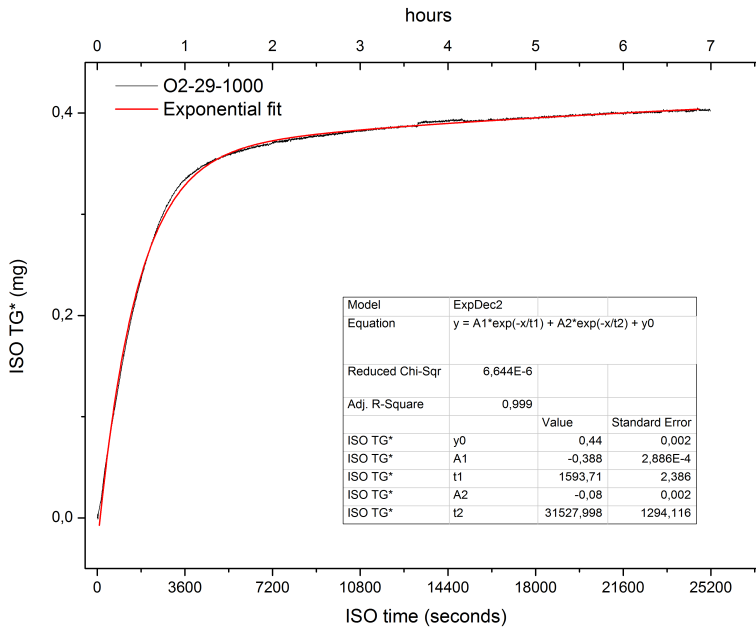
(a) Fitted exponential decay model ExpDec2_O2_29_1000
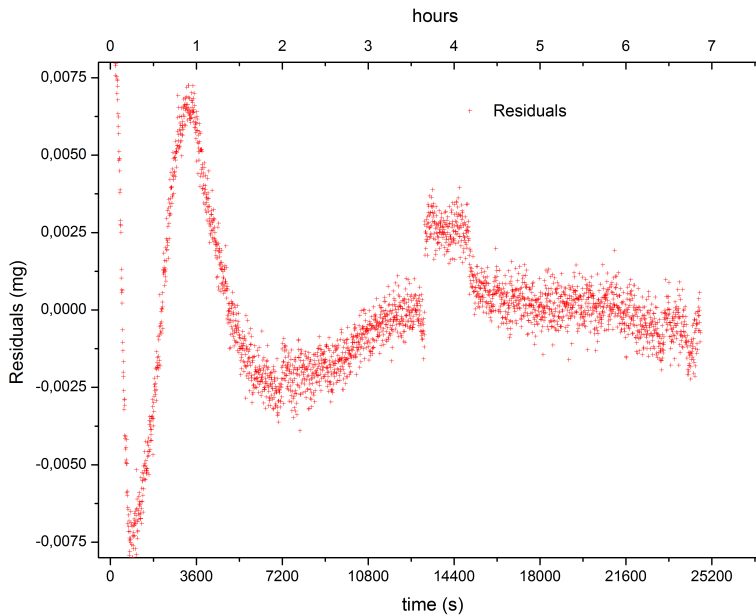
(b) Residuals for the exponential model in Figure (a) ExpDec2_O2_29_1000_Resid

Figure 5.4: *Exponential decay model fit model fits and residuals for sample O2_29_1000 Fig:ExpFit*

5.4.1.2 Second approach, linearization and fitting in sections

The next approach was linearization of the TGA data. Figure 5.5 shows that when the data was plotted on a log-log scale, the first 30 seconds of the TGA data contained a few negative values that introduced a discontinuity in the linearized data. The first 50-100 seconds of data are overrepresented on a log-log scale so ignoring these values should have little influence on the physical model.

(a) Fitted linear models Lin_O2_29_1000

(b)

(c)

Figure 5.5: *Linear model fits and residuals for sample O2_29_1000*

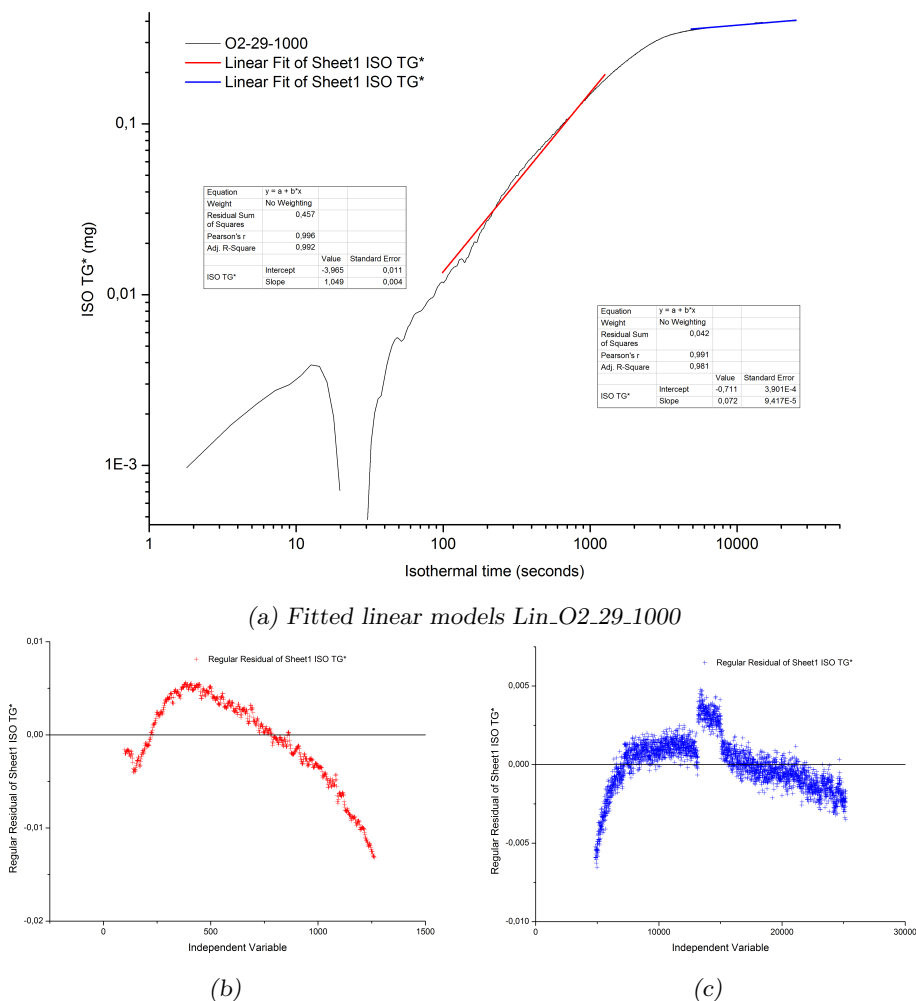The remainder of the data has two reasonably linear portions, but a simple model could not be found that fit the transition between the linear portions. Further, the residuals for each of the linear fits showed distinct patterns that indicated the linear fits were not adequate to describe the data.

5.4.1.3   Third approach, fitting in sections

Neither of the approaches in Sections 5.4.1.1 and 5.4.1.2 described the experimental data well, and involved somewhat complex models, so the approach was changed to fitting the data in sections using the simplest models possible. The time period chosen for each fitted section was balanced between covering as much data as possible, without generating excessive residuals.

Figure 5.6 shows the areas that were fit with linear equations, and the corresponding residuals. In the region $0 \leq t \leq 0.5h$, the curve appears to fit reasonably well

Figures 5.7 and 5.8 show the three-stage parabolic and cubic fits, along with the respective residuals. Both the parabolic and cubic models fit better in the first section (0 to ca. 1.5h) than the linear model in Figure 5.6, but the residuals for both models show definite patterns, indicating higher-order equations are needed to describe the data properly. The residuals for both of these models in the region $1.5 \leq t \leq 7h$ are nearly identical and show approximately the same pattern.
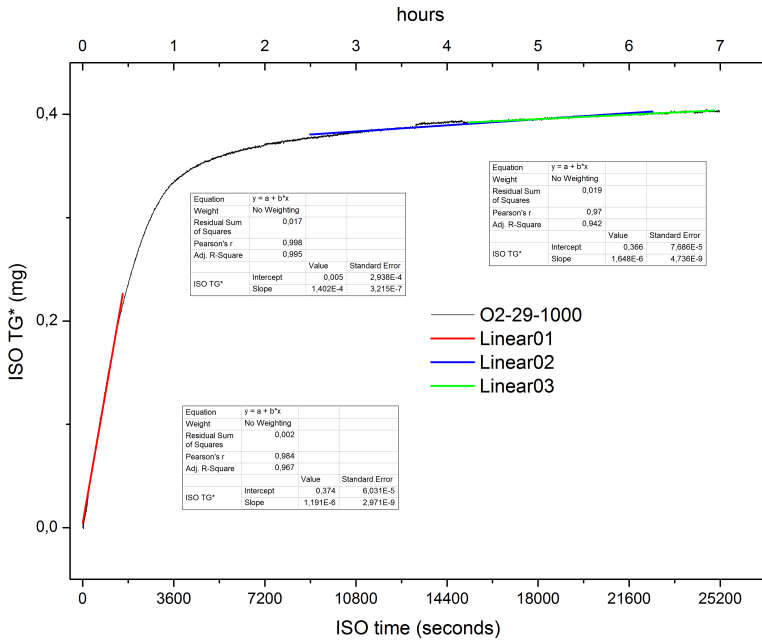
(a) Fitted linear models Lin_O2_29_1000
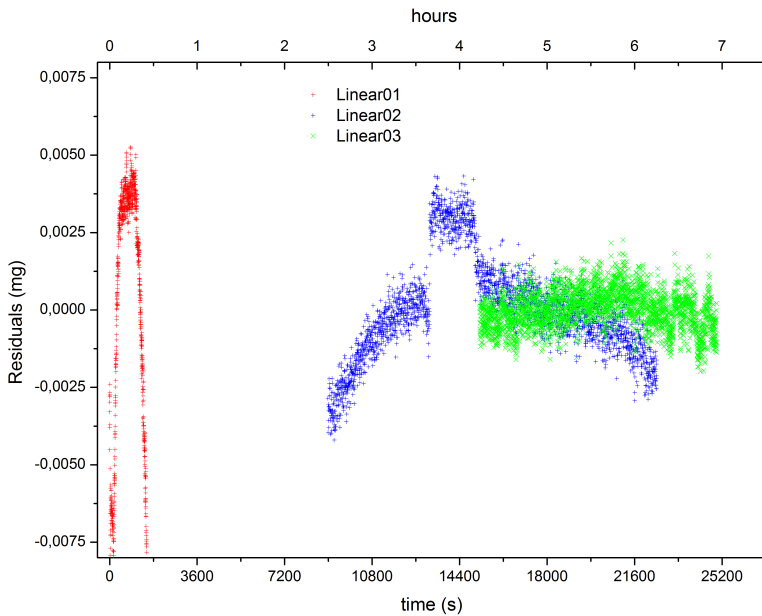
(b) Residuals for the linear models in (a) Lin_O2_29_1000_Resid

Figure 5.6: *Linear model fits and residuals for sample O2_29_1000 [17] Fig:LinearFit*
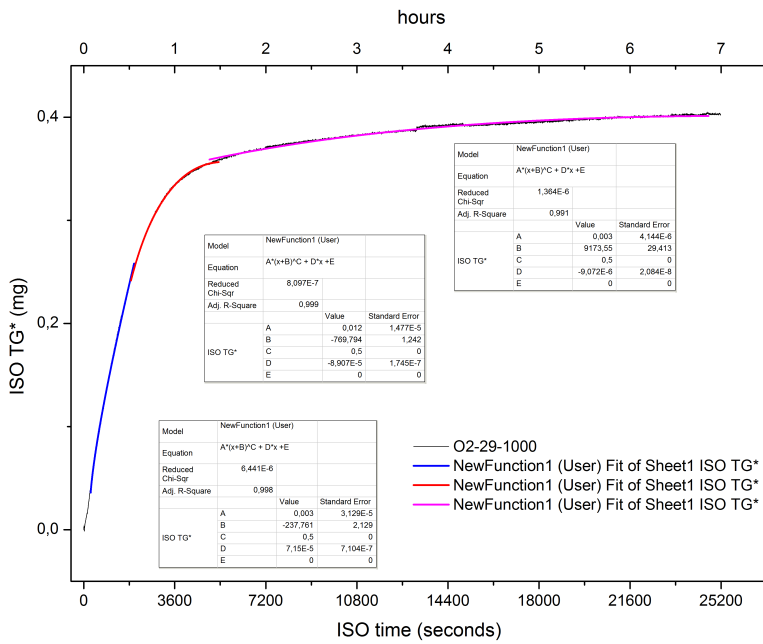
(a) Fitted parabolic models Parabol_O2_29_1000
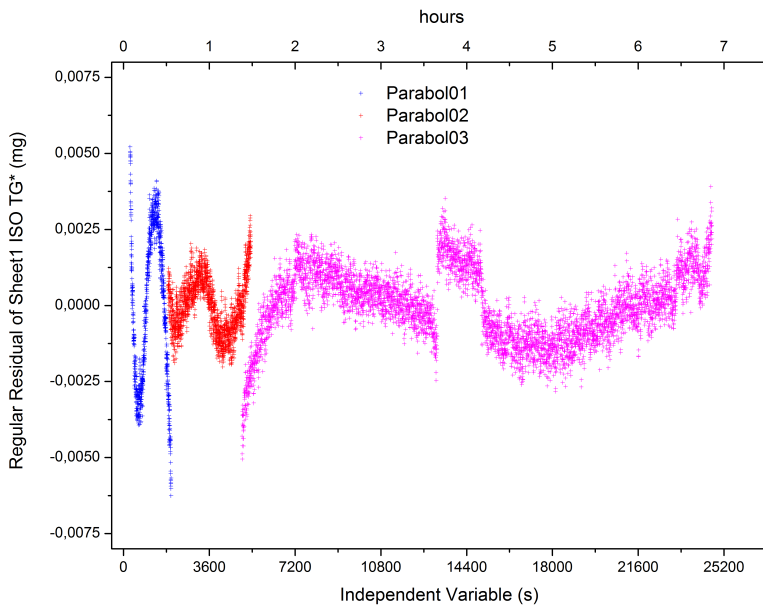
(b) Residuals for the parabolic model in (a) Parabol_O2_29_1000_Resid

Figure 5.7: *Parabolic model fits and residuals for sample O2_29_1000 [17] Fig:ParbolFit*
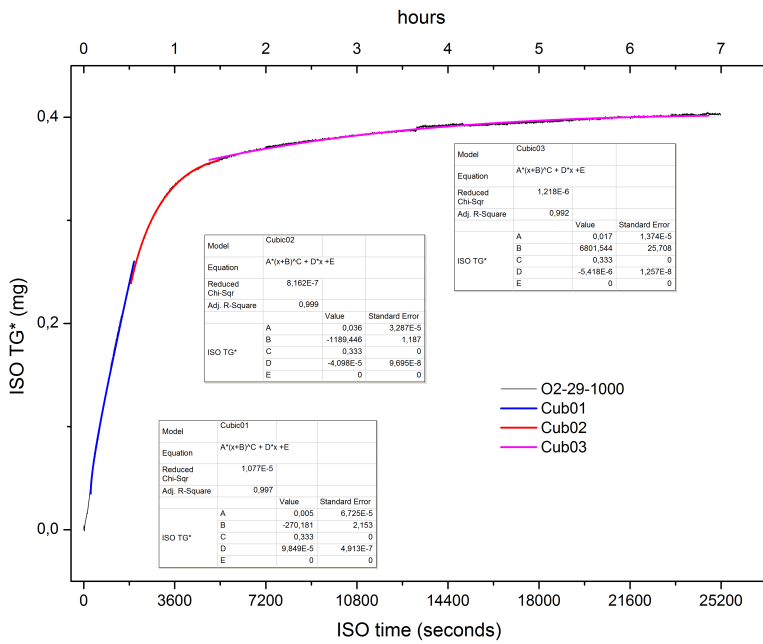
(a) Fitted cubic models Cubic_O2_29_1000

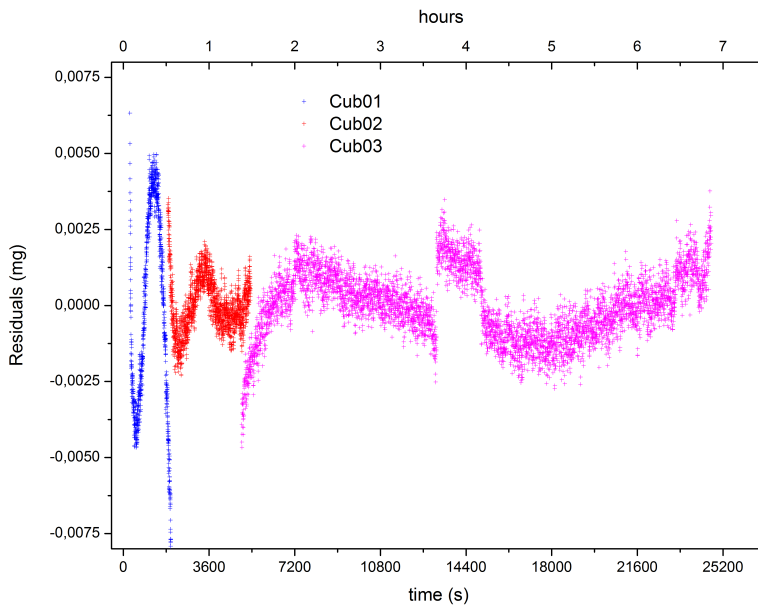
(b) Residuals for the cubic models in Figure 5.8(a) Cubic_O2_29_1000_Resid

Figure 5.8: *Cubic model fits and residuals for sample O2_29_1000 [17] Fig:CubicFit*

5.4.2 Pilling-Bedworth Ratio

The Pilling-Bedworth ratio is the ratio of the volume of an oxide to the volume of its corresponding metal, and predicts the protective behaviour of the oxide that is formed. The Pilling-Bedworth ratio is defined

$$R_{PB} = \frac{molar\ volume\ oxide}{molar\ volume\ metal} = \frac{M_{ox} \cdot \rho_{met}}{n \cdot M_{met} \cdot \rho_{ox}} \tag{5.27}$$

Where $\begin{cases} R_{PB} < 1 : & \text{the oxide coating layer is too thin, likely broken and provides no protective effect} \\ R_{PB} > 2 : & \text{the oxide coating chips off and provides no protective effect} \\ 1 < R_{PB} < 2 : & \text{the oxide coating is passivating and provides a protecting effect against further surface oxidation} \end{cases}$

Using values from Table 5.2 for aluminum and α-Al$_2$O$_3$,

$$R_{PB,Al} = \frac{(102)(2700)}{(2)(27)(3950)} \tag{5.28}$$

$$\boxed{R_{PB,Al} = 1.29} \tag{5.29}$$

and for the Mn-MnO system, using values from [2],

$$R_{PB,Mn} = \frac{(70.94)(7430)}{(54.94)(5430)} \tag{5.30}$$

$$\boxed{R_{PB,Mn} = 1.77} \tag{5.31}$$

According to the Pilling-Bedworth ratio both of these oxides should be passivating. The Pilling-Bedworth ratio for Mn is toward the upper end of the "passivating" spectrum, so the Mn oxide properties may tend toward chipping instead of passivating. This could help explain the fractured oxides found for the AlMn alloys in the muffle furnace investigations.

5.4.3 Possible oxidation mechanisms

Attempts to fit different models to the TGA data did not produce satisfactory results; there is more going on than can be explained by simple mathematical equations.

From a physical standpoint, Al and Al$_2$O$_3$ have quite different thermal expansion coefficients; the coefficient for Al is $23.1 \times 10^{-6} m\ m^{-1} K^{-1}$, while the coefficient for Al$_2$O$_3$ is $5.4 \times 10^{-6} m\ m^{-1} K^{-1}$, a factor of more than 4. Combining this large difference in expansion with the high temperature oxidation behavior shown in the generic TGA mass oxidation curve in Figure 5.9 (as well as using some imagination), the following mechanism combining oxide fracture and diffusion behaviour could be suggested, and is shown in Figure 5.10.
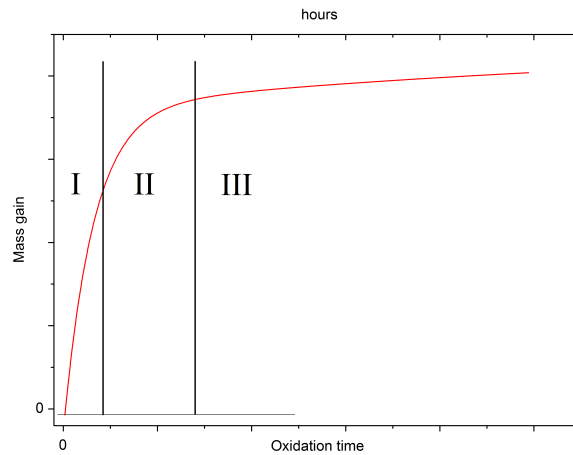
Figure 5.9: *Generic TGA oxidation curve shape, showing regions of different behaviour*
  Fig:generic

1. Figure 5.10(a): A coherent, protective layer of alumina is formed on the surface at ambient temperature.

2. Figure 5.10(b): As the sample is heated in Ar, the alumina on the surface cracks due to the differences in thermal expansion. A very thin layer of fresh alumina is formed at the bottom of the cracks and oxygen has easy access to the Al through the fresh Al_2O_3, but there is only 1ppm oxygen in the furnace atmosphere and this oxidation is very slow. This would take place in the heating phase before $t = 0$ in Figure 5.9.

3. Figures 5.10(c) and (d): When oxygen is added to the furnace, the fresh alumina thickens, while the cracks in the original alumina are slowly filled by fresh alumina. This gives the rapid, reaction controlled mass gain in Region I in Figure 5.9 since the oxygen still has a relatively short path through the new oxide to the metal.

4. Figures 5.10(e): The cracks in the original Al_2O_3 are filling with fresh alumina and are closing up. The mass gain now exhibits mixed reaction and diffusion control, and slows dramatically due to the thickening layer of new alumina the oxygen must diffuse through. This corresponds to Region II in Figure 5.9.

5. Figures 5.10(f): The cracks in the original Al_2O_3 are now filled with fresh alumina and have completely closed up. The mass gain in Region III in Figure 5.9 is very slow and is fully diffusion-controlled.

(a) Fig:M00

(b) Fig:M01

(c) Fig:M02

(d) Fig:M03

(e) Fig:M04

(f) Fig:M05
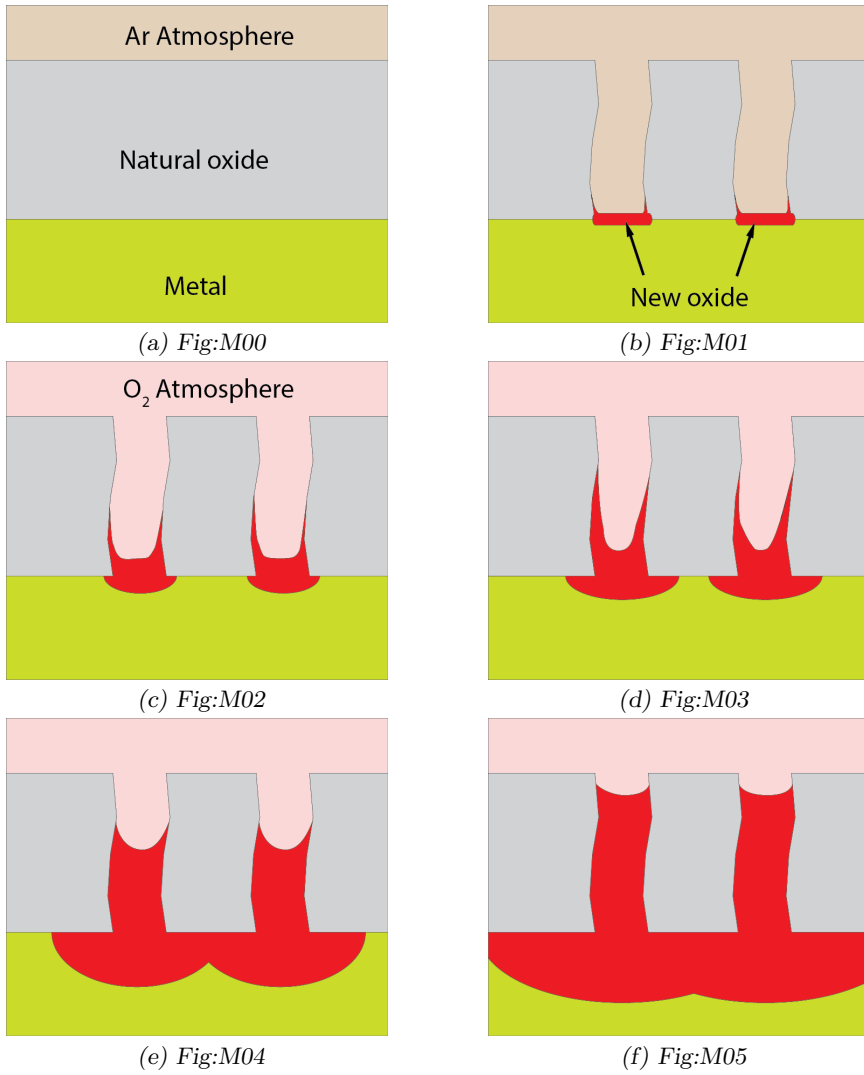
Figure 5.10: *Proposed oxidation model Fig:OxMod*

6. Conclusions

An oxidation study was performed on 99.99% Al, Al1%Mn and Al5%Mn materials, both in a thermogravimetric furnace, and in a muffle furnace. The mass gain behaviour for these materials was studied and compared for different temperatures and surface preparations, and was compared to previous work on Al1Mn.

Curve fitting was used with the thermogravimetric data in an attempt to develop a mathematical model to describe oxidation in the Al1%Mn materials, but a satisfactory model could not be found.

The oxidized materials were then analyzed in the Scanning Electron Microscope using EDS and Auger microprobe analysis, both for chemical composition and to analyze the structure of the oxide that was formed.

The main findings from the thermogravimetric work are as follows:

1. Error analysis showed that the mass measurement errors were at least two orders of magnitude smaller than the mass measurements, so any differences between samples was due to different oxidation behaviour in the sample.
2. There was inconsistent oxidation behaviour for the Al1Mn surface-cleaned TGA samples; for six identical samples and experiments, five samples showed comparable results, while one sample showed much larger mass gain.
3. Sample preparation has a large influence on oxidation behaviour in the muffle furnace.
4. Mn content has an influence on oxidation behavior; there was a trend of increasing oxidation with increasing Mn content in the muffle furnace samples.

The main findings from the SEM analysis of the oxidized 99.99% Al, Al1%Mn and Al5%Mn materials are as follows:

1. The oxides formed on the Al1Mn and Al5Mn materials were thicker and different than those found on 99.99% Al
2. The oxides formed on the Al1Mn and Al5Mn materials did not contain Mn oxides
3. The oxides formed on the Al1Mn and Al5Mn materials had small particles of Mn metal completely surrounded by Al_2O_3
4. Mn-rich particles were found in the interior of the Al1Mn and Al5Mn samples
5. Small clusters of Mn metal were found among the Al_2O_3 particles on the surface of the Al1Mn and Al5Mn samples

Glow Discharge Optical Emission Spectroscopy showed that there was no measurable Mn on the surface of an as-extruded Al1Mn strip, and the Mn was deficient to a depth of some 100nm from the surface. A similar Al1Mn extruded strip that had $50\mu m$ of the surface mechanically removed also did not contain Mn on the surface, and had a similar Mn profile to the as-extruded strip.

A qualitative physical model of oxidation was suggested, based on thermogravimetric data.

References

[1] ASM Handbook (1990), *Volume 2: Properties and Selection: Nonferrous Alloys and Special Purpose Materials.* pp 15-20

[2] Aylward, G. H. and T. J. V. Findlay (2002). *SI Chemical Data 5^{th}ed.* Milton, Wiley.

[3] Bird, Lightfoot and Stewart (2007).*Transport Phenomena*

[4] BRONKHORST HIGH-TECH B.V. *General instructions digital Mass Flow/Pressure instruments laboratory style/IN-FLOW*, Document no. 9.17.022S Date: 03-09-2012

[5] Çengel, Yunus A. (2002) *Thermodynamics: an engineering approach* McGraw Hill, pp. 667-711

[6] Cochran, C. N., Belitskus, D. L. and Kinosz, D. L. (1977) *Oxidation of Aluminum-Magnesium Melts in Air, Oxygen, Flue Gas, and Carbon Dioxide* Met Trans B Volume 8B June 1977 pp.323-332

[7] Impey, S.A. (1989), PhD thesis *The Mechanism of Dross Formation on Aluminium and Aluminium-Magnesium Alloys* Cranfield Institute of Technology

[8] FactSage phase diagrams calculated by Kai Tang, SINTEF

[9] Lapointe, K., Kvithyld, A., Bao, S. (2012) *Oxidation of Flash-Anodized Aluminium-Magnesium Alloy in Pure Atmospheres of Nitrogen, Carbon Dioxide, and Oxygen* SINTEF Report number F23409

[10] Leftsad, M. and Kvithyld, A. SINTEF internal memo 2012.07.04 *Prosjekt 80569113 Ekstrudering av skinne (Al1%Mn) i laboratoriepresse*

[11] de Nevers, N. (2000) *Air Pollution Control Engineering 2nd edition* McGraw-Hill, pp. 372-402, 2000.

[12] Ray, H.S. (1993). *Kinetics of Metallurgical Reactions* International Science Publisher.

[13] Rossel, H. (1990). *FUNDAMENTAL INVESTIGATIONS ABOUT METAL LOSS DURING REMELTING OF EXTRUSION AND ROLLING FABRICATION SCRAP* Light Metals/TMS

[14] Squires, G.L. (2001) *Practical Physics, 4th Edition* Cambridge University Press.

[15] Taylor and Francis (2012-2013). *CRC Handbook of Chemistry and Physics 93rd ed.* CRC Press.

[16] Wagner, C. (1955). *Kinetics in Metallurgy* M.I.T. Course 3.63. M.I.T, Spring 1955.

[17] Wilson, S.C. (2012) *Oxidation of Aluminum-Manganese Alloys During Remelting* TMT5500 Master Project, NTNU

[18] Young, D.J. (2008) *High Temperature Oxidation and Corrosion of Materials* Elsevier.

A. Gaussian Error Function

For the integral $\int_{-\infty}^{\infty} e^{-x^2} \mathrm{d}x$:

$$I = \int_{-\infty}^{\infty} e^{-x^2} \mathrm{d}x \tag{A.1}$$

Square both sides of (A.1), but multiply the RHS by the same integral with a different variable; this simplifies later operations:

$$I^2 = \int_{-\infty}^{\infty} e^{-x^2} \mathrm{d}x \int_{-\infty}^{\infty} e^{-y^2} \mathrm{d}y \tag{A.2}$$

$$= \int_{-\infty}^{\infty} \int_{-\infty}^{\infty} e^{-(x^2+y^2)} \mathrm{d}x \ \mathrm{d}y \tag{A.3}$$

Change to polar coordinates, where $x^2 + y^2 = r^2$ and $\mathrm{d}x \ \mathrm{d}y = r \ \mathrm{d}r \ \mathrm{d}\theta$. The new limits of integration are $0 \to 2\pi$ for $\mathrm{d}\theta$ and $0 \to \infty$ for $\mathrm{d}r$:

$$I^2 = \int_0^{2\pi} \int_0^{\infty} e^{-r^2} \ r \ \mathrm{d}r \ \mathrm{d}\theta \tag{A.4}$$

There is no θ dependence in the integrand, so (A.4) simplifies to:

$$I^2 = \pi \int_0^{\infty} e^{-r^2} \ 2r \ \mathrm{d}r \tag{A.5}$$

With the substitution $u = r^2$ and $du = 2r \ dr$, the limits of integration do not change since $u = 0$ when $r = 0$ and $u = \infty$ when $r = \infty$:

$$I^2 = \pi \int_0^{\infty} e^{-u} \ \mathrm{d}u \tag{A.6}$$

$$= \pi \left[-e^{-u} \right]\Big|_{u=0}^{\infty} \tag{A.7}$$

$$I^2 = \pi \left[-e^{-\infty} - (-e^0) \right] = \pi[0+1] = \pi \tag{A.8}$$

$$\boxed{I = \sqrt{\pi}} \tag{A.9}$$

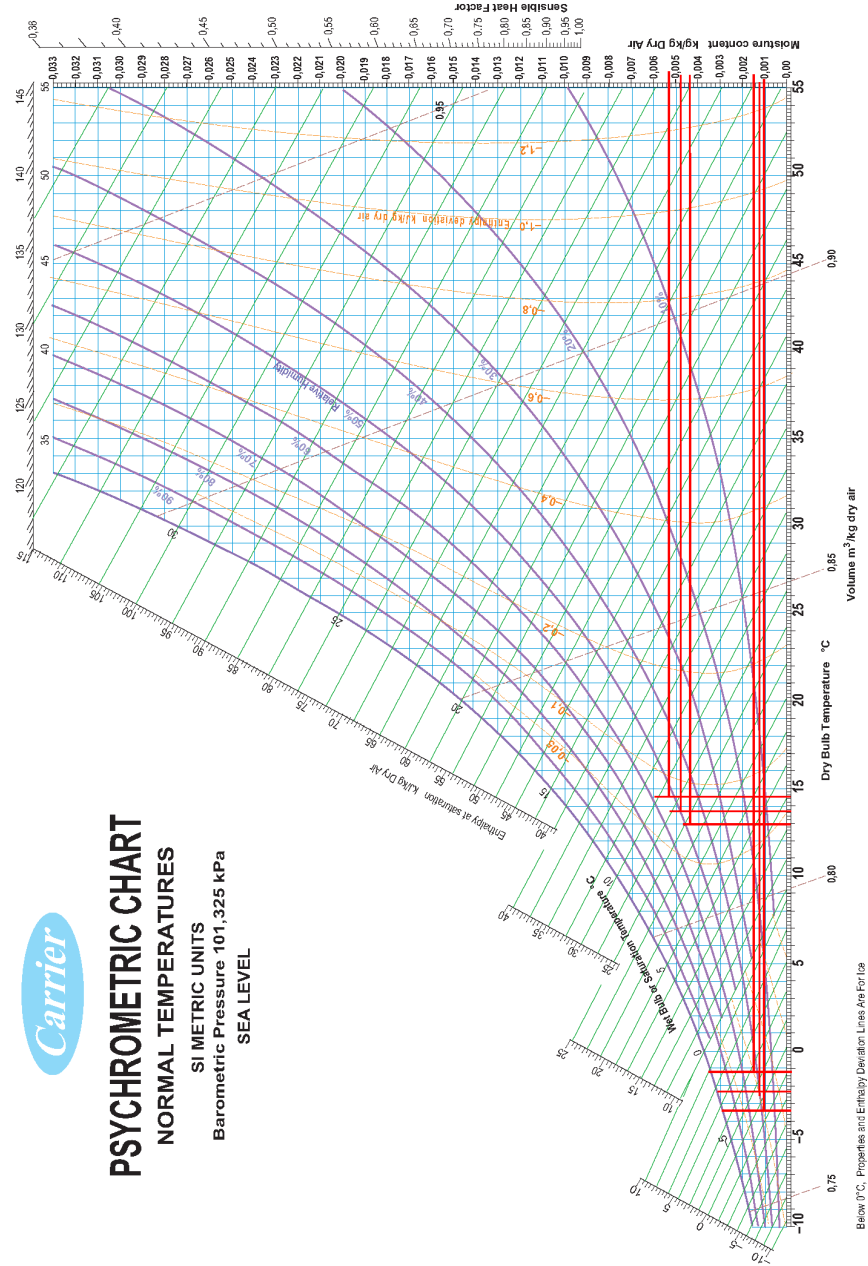# B. Carrier Psychrometric Chart for Normal Temperatures

Figure B.1: *Carrier Psychrometric Chart for Normal Temperatures, humidity conditions for muffle furnace experiments are marked in red*

C. Wetsys Calculations:

Temperature required to prevent condensation and gas flow settings to produce desired H_2O content   Given: Industrial aluminum remelting furnace atmosphere with air-fuel burners: 7 molar% H_2O with N_2, O_2 and CO_2 present

Assumptions:

1. Ideal gas behaviour for all gas species except H_2O.
2. H_2O's non-ideal behaviour is accurately described by psychrometric charts and steam tables.
3. Psychrometric charts are based on air $\longrightarrow$ Assume in calculations that 7 mol% H_2O in air has the same H_2O saturation temperature and pressure (dew point), as in other gases at a given temperature and pressure.
4. Air consists of 21% O_2 and 79% N_2, other components are ignored. (Mean molar mass 28.97g/mol [2])
5. The same gas is used in the Setsys balance head and Wetsys inlet.

Table C.1: *Ideal gas data at sea level, P = 1 atm = 101.325kPa[2]*

Standard condition	℃	K	Volume, L/mol
STP	0	273.15	22.414
SATP	25	298.15	24.790

Table C.2: *Molar masses[2], see assumptions for air*

Species	H	N	O	H_2O	N_2	O_2	CO_2	Air
g/mol	1.008	14	16	18.016	28.02	32	44	28.86

For a basis of 10mol furnace gas with 7 vol% (=mol%) H_2O(g) at 1atm:

$$H_2O: 0.7\text{mol} \times 18.016\text{g/mol} = 12.611\text{g } H_2O \tag{C.1}$$

$$\text{Air, assumed: } 9.3\text{mol} \times 28.86\text{g/mol} = 268.398\text{g air} \tag{C.2}$$

$$\text{Air, mean : } 9.3\text{mol} \times 28.86\text{g/mol} = 269.421\text{g air} \tag{C.3}$$

$$\text{Mass fraction } H_2O : \frac{\text{mass } H_2O}{\text{Total mass}} = \frac{12.611}{12.611 + 268.398} \quad = 4.488\% \tag{C.4}$$

$$\text{Air Humidity Ratio : } \frac{\text{mass } H_2O}{\text{mass dry air}} = \frac{12.611}{268.398} \quad = 0.04699 \tag{C.5}$$

Equation (C.5) is also known as the **Moisture Content in air.**

Sensitivity Check: In Assumption 4, air consists only of 21% O_2 and 79% N_2 with a molar mass of 28.86g/mol. When the minor components of air are taken into consideration, the mean molar mass is 28.97g/mol [5]. Using the mean value in Equation (C.3):

$$\text{Mass fraction } H_2O : \frac{\text{mass } H_2O}{\text{Total mass}} = \frac{12.611}{12.611 + 269.421} \quad = 4.472\%$$

$$\text{Air Humidity Ratio : } \frac{\text{mass } H_2O}{\text{mass dry air}} = \frac{12.611}{269.421} \quad = 0.04681 \tag{C.6}$$

Comparing the values in Equations (C.5) and (C.6), the error is essentially zero, so it is valid to use Assumption 4:

$$\text{Error} = \frac{\text{Assumed value - True value}}{\text{True value}} = \frac{0.04699 - 0.04681}{0.04681} = 0.38\%$$

The Setsys balance head must be protected from humidity by continuous flushing with dry gas at 10mL/min. This dilutes the humid gas, so the flow of humid gas from the Wetsys must be increased to compensate for the dilution in order to get the correct humidity level in the furnace. The Wetsys can deliver humid gas at rates of 0 - 50mL/min, but the maximum gas flow past the sample crucible must not exceed 50mL/min; above this limit the turbulent gas flow disturbs the TG (mass) signal. Therefore, given 10mL/min of dry gas through the balance head, the maximum Wetsys gas flow is 40mL/min. For a total gas flow rate of 50mL/min at STP conditions:

$$\text{Total gas} = 50\text{mL} \times 22.414\text{L/mol} \qquad = 2.231\text{mmol} \tag{C.7}$$

$$H_2O = 7\% \times 2.213\text{mmol} \qquad = 0.155\text{mmol} \tag{C.8}$$

$$\text{Dry air} = 2.231 - 0.155 \qquad = 2.076\text{mmol} \tag{C.9}$$

Of this air, 10mL/min goes through the balance head.

$$\text{Balance head air} = \frac{0.01\text{L}}{22.414\text{L/mol}} = 0.446\text{mmol} \tag{C.10}$$

$$\text{Wetsys air} = 2.075 - 0.446 = 1.628\text{mmol} \tag{C.11}$$

Converting Equations (C.8) through (C.11) from moles to mass for use in the Akton psychrometric chart:

$$\text{H}_2\text{O} = 0.155\text{mmol} \times 18.02\text{g/mol} = 2.813\text{mg} \tag{C.12}$$

$$\text{Dry air} = 2.075\text{mmol} \times 28.86\text{g/mol} = 59.87\text{mg} \tag{C.13}$$

$$\text{Balance head air} = 0.446\text{mmol} \times 28.86\text{g/mol} = 12.88\text{mg} \tag{C.14}$$

$$\text{Wetsys air} = 1.628\text{mmol} \times 28.86\text{g/mol} = 47.00\text{mg} \tag{C.15}$$

The maximum H_2O content of the humid gas is a function of gas temperature, and is limited by the lowest temperature in the system in order to prevent condensation. Equation (C.6) is used to calculate the humidity ratios for both the Wetsys and total furnace gases, in order to determine their dewpoints from the Akton psychrometric chart in Figure C.1:

$$\text{Wetsys gas humidity ratio} = \frac{\text{mass H}_2\text{O}}{\text{mass dry air}} = \frac{2.813}{47.00} = 0.05986 \tag{C.16}$$

$$\text{Furnace gas humidity ratio} = \frac{\text{mass H}_2\text{O}}{\text{mass dry air}} = \frac{2.813}{59.87} = 0.04699 \tag{C.17}$$

From Figure C.1, a humidity ratio of 0.060 gives a dew point (100%RH) temperature of 44±0.5℃ (red line in Figure C.1) for the Wetsys gas, so both the Wetsys, and the humid gas transfer tube between the Wetsys and Setsys must be kept above this temperature. 50℃ was chosen to give some margin (green line in Figure C.1). A humidity ratio of 0.047 gives a dew point (100%RH) temperature of 39℃±0.5℃ for the furnace gas, so all experimental equipment in contact with this humid gas must be kept above this temperature to prevent H_2O condensation. A summary of the relationship between humidity ratio, %RH and temperature is given in Table C.3.

Table C.3: *% Relative humidity temperatures, given Humidity Ratio in grams H_2O/grams dry air. All temperatures ± 0.5℃, data from Akton Psychrometric Table*

Humidity Ratio	Saturation	95%	90%	85%	80%
Wetsys humid gas 0.0599	43.5℃	44.5℃	45.5℃	47.0℃	48.0℃
Furnace atmosphere 0.0470	39.0℃	40.0℃	41.0℃	42.0℃	43.0℃

Relative humidity in air is the relationship of the vapour pressure of water to its saturation pressure in air at a given temperature, and is therefore related to the molar quantities of each species. For gases other than air, Equation (C.5) can be generalized, and we define the *Molar humidity ratio* and *Gas humidity ratio*:

$$\text{Molar humidity ratio} = \frac{\text{n}_{\text{H}_2\text{O}}}{\text{n}_{dry\,gas}} \tag{C.18}$$

$$\text{Gas humidity ratio} = \frac{\text{mass H}_2\text{O}}{\text{mass dry gas}} = \frac{\text{n}_{\text{H}_2\text{O}}\,\text{M}_{\text{H}_2\text{O}}}{\text{n}_{dry\,gas}\,\text{M}_{dry\,gas}} \tag{C.19}$$
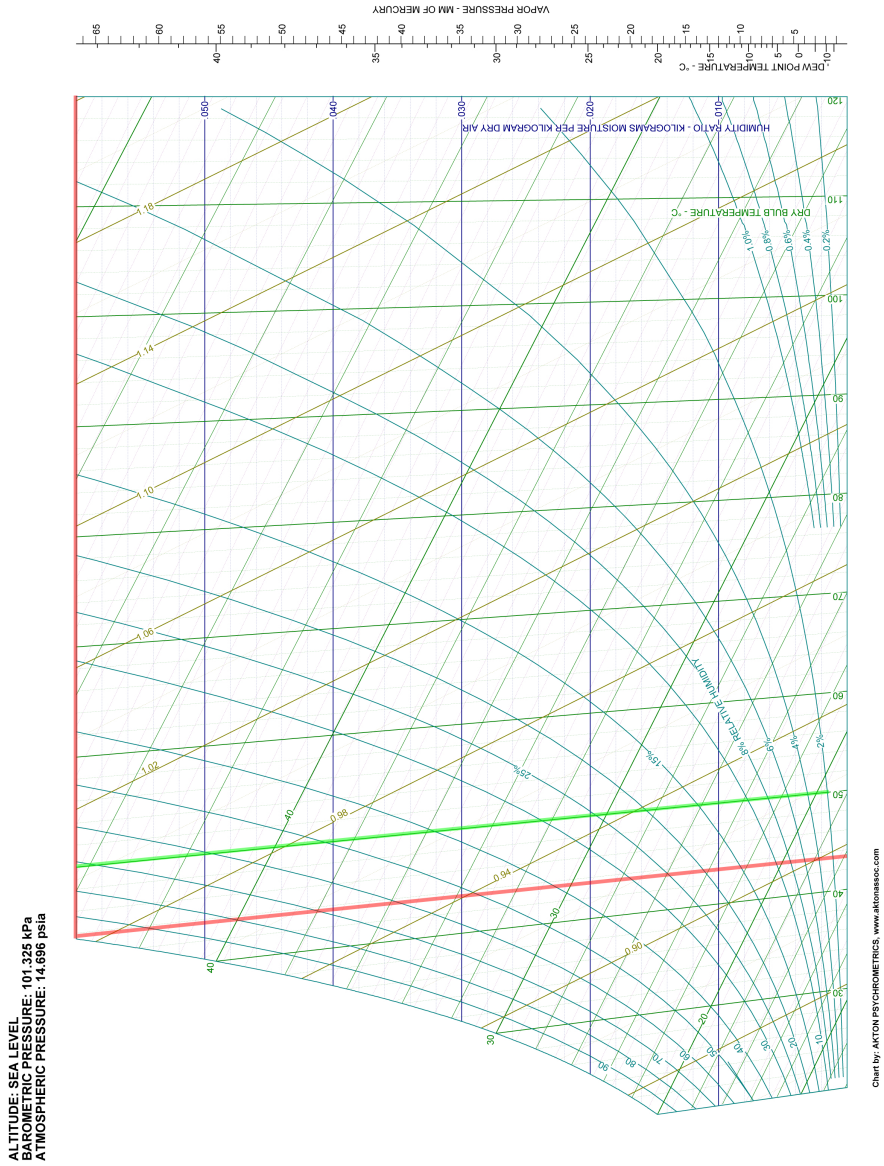
Figure C.1: *Akton High Temperature Psychrometric Chart for Sea Level*

Where n is the number of moles of the species and M is the molar mass of the species. For example, given 100mol of gas that consists of CO_2 with 7mol% H_2O, the gas humidity ratio is:

$$\frac{7\text{mol } H_2O \times 18.016 \frac{\text{g}}{\text{mol}}}{93\text{mol } CO_2 \times 44 \frac{\text{g}}{\text{mol}}} = \frac{126.112\text{g } H_2O}{4092\text{g } CO_2} = 0.031 \frac{\text{g } H_2O}{\text{g dry } CO_2} \tag{C.20}$$

Equations (C.18) and (C.19) use Assumption 1, that all gases except H_2O behave as ideal gases, and this assumption is generally valid at near-ambient temperatures and pressures. To confirm this assumption, a measure of the "ideality" of a gas or gas mixture is the compressibility factor, z in the Ideal Gas Equation:

$$PV = znRT \tag{C.21}$$

The compressibility factor is dependent on the relationship of the gas temperature and pressure to the critical temperature and pressure for that gas:

$$T_{reduced} = \frac{T}{T_{critical}} \tag{C.22}$$

$$P_{reduced} = \frac{P}{P_{critical}} \tag{C.23}$$

Using the reduced temperature and pressure, the compressibility factor can be found in the Nelson-Obert Generalized Compressibility Charts [5]. Under the experimental conditions of 1 atmosphere pressure $= 0.101$ MPa and 50℃ $= 323$K, the compressibility factors for the experimental gases are listed in Table C.4

Table C.4: *Compressibility factors for experimental gases at 1atm and 50℃ [5].*

Gas	T_{cr},K	P_{cr},MPa	T_r	P_r	z
Air	132.5	3.77	2.44	0.027	1
Ar	151	4.86	2.14	0.021	1
CO_2	304.2	7.39	1.06	0.014	1
N_2	126.2	3.39	2.56	0.030	1
O_2	154.8	5.08	2.09	0.020	1
H_2O	647.3	22.09	0.50	0.005	1

Since the compressibility factors for all of the gases are equal to 1, the assumption of ideality (Assumption 1) is reasonable.